

# Time-domain evolution of Lorenz-gauge metric perturbations: taming the $\ell = m = 1$ gauge instability

Jonathan Thornburg<sup>1,2,3,\*</sup>

<sup>1</sup>*BKIS Orchards, Box 87, Thetis Island BC V0R 2Y0, Canada*

<sup>2</sup>*Department of Astronomy and Center for Spacetime Symmetries,  
Indiana University, Bloomington, Indiana 47405, USA*

<sup>3</sup>*Max-Planck-Institut für Gravitationsphysik, Albert-Einstein-Institut,  
Am Mühlenberg 1, D-14476 Potsdam-Golm, Germany*

Calculating the spacetime metric perturbation (MP) sourced by a small “particle” of mass  $\mu M$  (with  $0 < \mu \ll 1$ ) moving in a Schwarzschild or Kerr “background” black hole spacetime of mass  $M$  is a longstanding research area in general relativity. This calculation also has an important astrophysical motivation as a major step in calculating the gravitational waves emitted by an extreme-mass-ratio inspiral (EMRI) system. Here I consider the specific problem of the time-domain calculation of the  $\mathcal{O}(\mu)$  Lorenz-gauge MP  $h_{ab}$  sourced by the particle. Decomposing the Schwarzschild-background MP into  $e^{im\phi}$  modes, Dolan and Barack [*Phys. Rev. D* **87**, 084066 (2013)] found that the  $m = 1$  time-domain Lorenz-gauge MP generically contains an *unstable gauge mode* which grows linearly with time. Here I demonstrate a method for computing a Lorenz-gauge time-domain evolution which is mostly free of this gauge mode. This method computes an “orthogonalized” MP  $h_{ab}^{(\text{ortho})}$  as a linear combination of the sourced MP and a homogeneous MP  $h_{ab}^{(\text{hom})}$  (evolved in parallel with the sourced MP). The linear combination is updated “occasionally” to make  $h_{ab}^{(\text{ortho})}$  orthogonal to  $h_{ab}^{(\text{hom})}$  with respect to a chosen inner product on MPs. I show that, for the test case of a particle in a circular orbit in a Schwarzschild background, the resulting  $h_{ab}^{(\text{ortho})}$  satisfies the  $\mathcal{O}(\mu)$  Einstein equations and the  $\mathcal{O}(\mu)$  Lorenz gauge conditions, remains bounded as  $t \rightarrow \infty$ , and at late (finite) times contains only a small component of the unstable gauge mode. These results hold both for the case where the particle is modelled as a point particle with MP jump conditions across the particle, and for the case where the particle is modelled by a Barack-Goldburn-Vega-Detweiler “effective source”. My numerical code for evolving the MP, computing  $h_{ab}^{(\text{ortho})}$ , and verifying the above results is included as online supplemental material with this paper, and will be deposited in the open-source Black Hole Perturbation Toolkit.

PACS numbers: 04.25.Nx, 04.25.dg 02.70.-c, 04.25.Dm,

Keywords: general relativity, perturbation theory, black hole, Schwarzschild spacetime, Kerr spacetime, Lorenz gauge, unstable gauge mode, metric perturbation, extreme-mass-ratio inspiral, orthogonalization

*This paper is dedicated to the memory of my late friend and colleague Professor Steven Detweiler.*

## I. INTRODUCTION

Consider a small body (“particle”) of mass  $\mu M$  (with  $0 < \mu \ll 1$ ) moving freely in an asymptotically flat and (exterior to any event horizon) globally hyperbolic background spacetime (e.g., Schwarzschild or Kerr spacetime) of mass  $M$ . Self-consistently calculating the resulting spacetime and the motion of the small body is a longstanding research question in general relativity.

There is also an astrophysical motivation for this calculation: If a neutron star or stellar-mass black hole of mass  $\sim 1\text{--}100M_{\odot}$  orbits a massive black hole of mass  $\sim 10^5\text{--}10^7M_{\odot}$ ,<sup>1</sup> the resulting “extreme-mass-ratio inspiral” (EMRI) system will be a strong astrophysical

gravitational-wave (GW) source, likely detectable by the planned Laser Interferometer Space Antenna (LISA) space-based gravitational-wave detector. LISA is expected to observe many such systems, some of them at quite high signal/noise ratios. The data analysis for, and indeed the detection of, such systems will generally require matched-filtering the detector data stream against large numbers of precomputed GW templates (LISA Consortium Waveform Working Group [27]). These templates, in turn, will mainly be generated by “fast waveform models” (e.g., Katz et al. [26]) calibrated against smaller numbers of waveforms calculated *ab initio*. The problem of computing these latter waveforms provides the astrophysical motivation for this work.

Here I consider the case where the particle’s orbit is too relativistic for post-Newtonian methods (e.g., Blanchet [10], Futamase and Itoh [19], and Schäfer and Jaranowski [29]) to be reliably accurate. Since the radiation-reaction orbital-evolution timescale is long ( $\sim \mu^{-1}M$ ) while the required resolution near the particle is high ( $\lesssim \mu M$ ), a direct “numerical relativity” integration of the Einstein equations would be very expensive (and possibly insufficiently accurate) for this problem.

\* dr.j.thornburg@gmail.com

<sup>1</sup>  $M_{\odot}$  denotes the solar mass.

Instead, I use black hole perturbation theory, treating the particle as an  $\mathcal{O}(\mu)$  perturbation on the background spacetime. For this work I consider only linear (1st-order) perturbation effects: I assume the particle moves on a pre-specified trajectory in the background spacetime, and consider the problem of calculating the resulting  $\mathcal{O}(\mu)$  metric perturbation via a time-domain numerical evolution of the Lorenz-gauge perturbed Einstein equations sourced by the particle, in the manner of Barack and Lousto [5] (hereinafter BL05).

As discussed by BL05, using the Lorenz gauge for such a calculation has the notable advantages that the Lorenz-gauge metric perturbation from a point particle is well-behaved both close to and far from the the particle, and that the Lorenz-gauge perturbed Einstein equations are a Z4 system (and hence are hyperbolic at leading order).

Time-domain calculations of this type are a useful complement to the more common frequency-domain calculations, and inter-comparing these different types of calculations can help improve our confidence in the correctness and accuracy of both. Two important advantages of time-domain calculations are that they're relatively easy to extend to highly eccentric particle orbits, and that (with somewhat more effort) they can be extended from a Schwarzschild background to a Kerr background,<sup>2</sup> although I will not further consider either of these extensions here.

Dolan and Barack [15] (hereinafter DB13) considered the test case of the Lorenz-gauge metric perturbation on a Schwarzschild background, with the metric perturbation decomposed into  $e^{im\phi}$  modes (so as to prototype a future extension to a Kerr background). They found that time-domain  $m = 1$  Cauchy evolutions exhibit an *unstable gauge mode*, i.e., a metric perturbation which grows unboundedly with time while still satisfying the Lorenz gauge condition at any finite time.<sup>3</sup> At any finite time, this gauge mode satisfies all appropriate physical boundary conditions at the horizon and at spatial infinity. At a fixed spatial position, this gauge mode grows linearly with time and so is unbounded as  $t \rightarrow \infty$ .

Decomposing the metric perturbation into Barack-Lousto-Sago ( $\ell, m$ ) tensor-spherical-harmonic modes (BL05, with the modification described by Barack and Sago [6, note 37], hereinafter BS07), DB13 found that the unstable gauge mode is an  $\ell = m = 1$  even-parity mode. DB13 also found an explicit analytical solution (their equation (131)) with properties matching their numerical results. It appears highly likely that a similar

mode would also be generically present in time-domain Lorenz-gauge metric-perturbation evolutions on a Kerr background.

This unstable gauge mode poses a major problem for time-domain evolutions of Lorenz-gauge metric perturbations. Several approaches have been proposed to resolve this problem, but thus far all require either analytical knowledge of the unstable gauge mode (available only for a Schwarzschild background), restrictions on the particle orbit, or leaving the time domain. (A frequency-domain evolution naturally enforces boundedness of the metric perturbation as  $t \rightarrow \infty$ , thus eliminating the unstable gauge mode.)

In their time-domain calculations of gravitational self-force on a Schwarzschild background, BL05 and Barack and Sago [6, 7, 8, 9] avoided the gauge mode problem by solving for the  $\ell = m = 1$  metric perturbation using the method of Detweiler and Poisson [13], but this method only applies for the case of a Schwarzschild background.

For the case of a circular geodesic particle orbit (where the metric perturbation's time dependence at a fixed spatial position contains only a single frequency), DB13 were able to remove the unstable gauge mode by applying a frequency-domain filter to the numerically-computed metric perturbation. This method will very likely also work for circular equatorial particle orbits on a Kerr background, but, unfortunately, there does not appear to be any way to generalize this method to more generic particle orbits. DB13 also found that the frequency filter introduces considerable high-frequency numerical noise.

For zero-energy zoom-whirl orbits in Schwarzschild, Barack et al. [3] were able to cancel out the unstable gauge mode in time-domain evolutions, but their method requires knowing the unstable gauge mode analytically, and is thus only applicable for a Schwarzschild background.

Here I present a new method for mostly removing the unstable gauge mode in  $m = 1$  time-domain Lorenz-gauge metric-perturbation evolutions. This method is based on *orthogonalizing* the metric perturbation with respect to an auxiliary homogeneous metric-perturbation evolution run in parallel with the main evolution. At late times the homogeneous metric perturbation is dominated by the unstable gauge mode, so orthogonalizing with respect to the homogeneous metric perturbation is approximately the same as orthogonalizing with respect to the unstable gauge mode. The result is that the orthogonalized metric perturbation is mostly free of (i.e., contains only a small component of) the unstable gauge mode.

I present numerical tests of the orthogonalization scheme for the test case of a particle in a circular geodesic orbit on a Schwarzschild background, using the BL05 formalism for time-domain Cauchy evolution of the metric perturbation in 1+1 numerical dimensions. I consider two different schemes for modelling the particle: either as a point particle via jump conditions for the Barack-Lousto-Sago fields and their derivatives across the particle (following BL05), or via a Barack-Golbourn-Vega-

<sup>2</sup> Frequency-domain calculations on a Kerr background are difficult for various reasons, notably the non-separability of the Lorenz-gauge metric perturbation equations (see, e.g., Teukolsky [31] and Whiting and Price [40]), although there has been major progress in recent years (Dolan et al. [16, 17], and Wardell et al. [39]).

<sup>3</sup> They also found unstable gauge modes in  $m = 0$  evolutions, but they were able to stabilize these evolutions using a generalization of the Lorenz gauge condition.

Detweiler effective source, using Wardell’s LorenzGauge-1DEffectiveSource effective source code (Wardell [38]).

To preview the main result of this paper, the orthogonalization technique works well for both point-particle and effective-source schemes. More precisely, I show that for both schemes, the orthogonalized metric perturbation

- satisfies the  $\mathcal{O}(\mu)$  Einstein equations and the  $\mathcal{O}(\mu)$  Lorenz gauge conditions (up to finite-differencing accuracy),
- remains bounded as  $t \rightarrow \infty$ , and
- at any finite time, contains only a small component (bounded as  $t \rightarrow \infty$ ) of the unstable gauge mode.

The remainder of this paper is organized as follows: Section IA summarizes my notation. Section II describes the  $\mathcal{O}(\mu)$  perturbed (linearized) Einstein equations, the point-particle and effective-source schemes for solving these, the unstable gauge mode, and the basic idea of the orthogonalization scheme, all for a generic background spacetime. Section III specializes to a Schwarzschild background, and describes the Barack-Lousto-Sago tensor-spherical-harmonic decomposition of metric perturbations and the resulting BL05 Cauchy evolution scheme for metric perturbations, the point-particle and effective-source schemes, the implementation of the orthogonalization scheme, and some points about the computation of diagnostics. Section IV describes numerical tests of my implementation of the BL05 evolution scheme and of the basic orthogonalization scheme. Section V presents conclusions and directions for further research. Appendix A describes the computation of the jumps in the Barack-Lousto-Sago fields across the particle when using a point-particle scheme. Appendix B describes my numerical scheme. Appendix C presents tests of four variants of the basic orthogonalization scheme: using a shorter orthogonalization time spacing, orbit-averaging  $\lambda$ , gradual turnon of the puncture and effective source, and using a fixed (time-independent)  $\lambda$ . Appendix D presents numerical tests of the convergence of the orthogonalized metric perturbation to a continuum limit, and the convergence of the corresponding Lorenz gauge constraints and independently-computed Einstein tensor to zero.

## A. Notation

I generally follow the sign and notation conventions of Wald [36], with  $G = c = 1$  units and a  $(-, +, +, +)$  metric signature. I assume spacetime to be globally hyperbolic (exterior to any event horizon), foliated by the 3-dimensional spacelike Cauchy hypersurfaces  $\Sigma_t$ , and asymptotically flat with (ADM) mass  $M$ .

I use the Penrose abstract-index notation, with lower-case Latin indices  $abcd$  from the beginning of the alphabet running over spacetime coordinates. Upper-case Latin indices  $IJK$  range over the integers from 1

to 10 inclusive, indexing the Barack-Lousto-Sago tensor-spherical-harmonic basis elements. Non-tensor indices and labels are generally parenthesized, as in  $\bar{h}_{(\text{ortho})}^{(I)}$ . A lower-case typewriter-font Latin  $i$  indexes grid points, and a lower-case typewriter-font Latin  $m$  indexes the individual points of finite-difference molecules, as described in detail in appendix B2. The indices  $\ell$  and  $m$  index tensor spherical harmonics, as described in section III A.

Spacetime coordinate indices  $abcd$  are subject to the Einstein summation convention. Non-tensor indices (including the spherical-harmonic indices  $\ell$  and  $m$ , any parenthesized indices, and any indices subscripting or superscripting the  $\sum$  symbol) are not subject to the Einstein summation convention.  $g_{ab}$  is the background spacetime metric, and is assumed to be Ricci-flat everywhere away from the particle.  $g_{ab}$  is used to raise and lower all indices.  $\partial_a = \partial/\partial x^a$  is the usual coordinate partial derivative operator,  $\nabla_a$  is the covariant derivative operator associated with  $g_{ab}$ , and  $\square = \nabla^a \nabla_a$  is the covariant D’Alembertian operator.  $h_{ab}$  is the metric perturbation,  $h = h_a^a$  is its trace, and  $\bar{h}_{ab} = h_{ab} - \frac{1}{2} h g_{ab}$  is the trace-reversed metric perturbation.

$\langle h_{ab}^{(A)}, h_{ab}^{(B)} \rangle$  is an inner product on metric perturbations  $h_{ab}$  in the constant-time slice  $\Sigma_t$ ,  $\|h_{ab}\|$  is the associated norm, and  $h_{ab}^{(A)} \perp h_{ab}^{(B)}$  means  $\langle h_{ab}^{(A)}, h_{ab}^{(B)} \rangle = 0$ . For any given  $(\ell, m)$ ,  $\langle \bar{h}_{(A)}^{(I)}, \bar{h}_{(B)}^{(I)} \rangle$  is an inner product on the Barack-Lousto-Sago metric-perturbation fields  $\bar{h}^{(I)} = \bar{h}^{(I\ell m)}$  in the constant-time slice  $\Sigma_t$ ,  $\|\bar{h}^{(I)}\|$  is the associated norm, and  $\bar{h}_{(A)}^{(I)} \perp \bar{h}_{(B)}^{(I)}$  means  $\langle \bar{h}_{(A)}^{(I)}, \bar{h}_{(B)}^{(I)} \rangle = 0$ . Indices repeated between the two arguments of the inner product, as in  $\langle h_{ab}^{(A)}, h_{ab}^{(B)} \rangle$  or  $\langle \bar{h}_{(A)}^{(I)}, \bar{h}_{(B)}^{(I)} \rangle$  are not subject to the Einstein summation convention. A caret accent denotes a unit vector defined with respect to the norm, as in  $\widehat{\bar{h}}^{(I)} := \bar{h}^{(I)} / \|\bar{h}^{(I)}\|$  ( $\sum^I$ ). ( $X := E$  or  $E := X$  means that  $X$  is defined to be (the expression)  $E$ .)

In the context of a specific coordinate system,  $\|T_{ab}\|$  is a pointwise norm over the coordinate components of a tensor or tensor-like expression  $T_{ab}$  at an event (so that the value of  $\|T_{ab}\|$  at an event is a single nonnegative real number).

$\varepsilon$  is the difference between 1.0 and the next larger floating-point number.  $\varepsilon \approx 1.1 \times 10^{-16}$  for IEEE-standard double-precision floating-point arithmetic (Goldberg [20]).

$\partial S$  is the boundary of the set of events  $S$ .  $\text{conj}[z]$  is the complex conjugate of the complex number  $z$ . Given a sequence of times  $\{t_k \mid k = 1, 2, 3, \dots\}$ ,  $[t]_{\{t_k\}}$  is the largest  $t_k \leq t$ .  $\text{average}(f, [A, B])$  is the average of the function  $f$  over the interval  $[A, B]$ , i.e.,  $(\int_A^B f(t) dt) / (B - A)$ .

A subscript  $p$  denotes quantities evaluated at the particle position; the particle is in a circular geodesic orbit at coordinate radius  $r = r_p$ , with (coordinate) orbit period  $P$ .

In the context of a specific coordinate system (for example, the usual Schwarzschild  $(t, r, \theta, \phi)$  coordinates for Schwarzschild spacetime), I use  $\times$  to denote the component-by-component multiplication of (coordinate) tensor components, as in  $S_{ab} \times G_{ab}$ . Indices appearing in such products are not subject to the Einstein summation convention.

In appendix A only,  $x := r_*$ ; for any variable or expression  $q$ ,  $q' := \partial_x q$  and  $[q]_p$  is the jump in  $q$  across the particle;  $N$  is the number of nontrivial Barack-Lousto-Sago Schwarzschild-metric-perturbation fields  $\bar{h}^{(\ell m)}$  ( $N=6$  for the  $\ell=m=1$  case which is the main focus here);  $\mathbb{T}$ ,  $\mathbb{X}$ , and  $\mathbb{V}$  are  $N \times N$  matrices; and for any given  $(\ell, m)$ ,  $\mathbf{u}$  and  $\mathbf{s}$  are (time-dependent)  $N$ -element column vectors of field variables.

## II. THEORY: GENERIC BACKGROUND

### A. Perturbed (Linearized) Einstein Equations

Consider an asymptotically-flat Ricci-flat “background” spacetime of mass  $M$  (in practice, this will be either Kerr or Schwarzschild spacetime) with metric  $g_{ab}$  and associated covariant derivative operator  $\nabla$ , perturbed by a small metric perturbation  $h_{ab}$  (so that the physical metric is  $g_{ab}^{(\text{physical})} = g_{ab} + h_{ab}$ ), with  $h_{ab}$  sourced by the stress-energy tensor  $T_{ab}$  of a small “particle” of mass  $\mu M$ , with  $0 < \mu \ll 1$ . I assume that both the background and physical spacetimes (exterior to any event horizon) are globally hyperbolic, foliated by the 3-dimensional spacelike hypersurfaces  $\Sigma_t$ , and that (again exterior to any event horizon) any  $t = \text{constant}$  hypersurface is a Cauchy surface.

Linearizing the physical-metric Einstein equations about the background metric gives (Wald [36, section 7.5], BL05)

$$\begin{aligned} G_{ab} := & \square h_{ab} - g_{ab} \square h \\ & + \nabla_a \nabla_b h + g_{ab} \nabla^c \nabla^d h_{cd} \\ & - \nabla_b \nabla^c h_{ac} - \nabla_a \nabla^c h_{bc} \\ & + 2R^c{}_a{}^d{}_b h_{cd} \\ = & -16\pi T_{ab} , \end{aligned} \quad (2.1)$$

where  $\nabla$ ,  $\square$ , the Riemann tensor, and index raising/lowering are all defined with respect to the background metric  $g_{ab}$ .

Defining the trace-reversed metric perturbation  $\bar{h}_{ab} := h_{ab} - \frac{1}{2} h g_{ab}$  (where  $h := h_a{}^a$ ) and adopting the Lorenz gauge condition

$$\nabla^b \bar{h}_{ab} = 0 , \quad (2.2)$$

the linearized Einstein equations (2.1) simplify to

$$\square \bar{h}_{ab} + 2R^c{}_a{}^d{}_b \bar{h}_{cd} = -16\pi T_{ab} . \quad (2.3)$$

### B. Effective-Source Scheme

The Barack-Golbourn-Vega-Detweiler effective-source scheme allows modelling a point particle without requiring a  $\delta$ -function stress-energy tensor  $T_{ab}$ . First introduced by Barack and Golbourn [4] and Vega and Detweiler [35], the effective source method is now widely used; see Wardell [37, section 3.3] for a review.

The basic concept of the effective-source scheme is to first choose (compute) a “puncture” metric perturbation  $\bar{h}_{ab}^{(\text{puncture})}$  which approximates (in a manner to be described below) the Detweiler-Whiting singular metric perturbation  $\bar{h}_{ab}^{(\text{singular})}$  (Detweiler and Whiting [14]) near the particle, so that the “residual” metric perturbation

$$\bar{h}_{ab}^{(\text{residual})} := \bar{h}_{ab} - \bar{h}_{ab}^{(\text{puncture})} \quad (2.4)$$

is finite in a neighborhood of the particle and “somewhat differentiable” (here,  $C^2$ ) at the particle. Substituting this definition into the  $\mathcal{O}(\mu)$  Lorenz-gauge perturbed Einstein equations (2.3) then gives

$$\square \bar{h}_{ab}^{(\text{residual})} + 2R^c{}_a{}^d{}_b \bar{h}_{cd}^{(\text{residual})} = -16\pi T_{ab} - \square \bar{h}_{ab}^{(\text{puncture})} - 2R^c{}_a{}^d{}_b \bar{h}_{cd}^{(\text{puncture})} \quad (2.5a)$$

$$= \begin{cases} 0 & \text{at the particle} \\ -\square \bar{h}_{ab}^{(\text{puncture})} - 2R^c{}_a{}^d{}_b \bar{h}_{cd}^{(\text{puncture})} & \text{elsewhere} \end{cases} \quad (2.5b)$$

$$=: S_{ab}^{\text{eff}} ,$$

where the effective source  $S_{ab}^{\text{eff}}$  is defined to be the RHS

of (2.5b).

There is considerable freedom in the precise choice of the puncture. My choice here is that embodied in Wardell’s `LorenzGauge1DEffectiveSource` open-source effective source code (Wardell [38]). This chooses  $\bar{h}_{ab}^{(\text{puncture})}$  to match the first 4 terms of the Laurent series expansion of  $\bar{h}_{ab}^{(\text{singular})}$  near the particle in powers of the distance from the particle. This puncture is only defined in a convex normal neighborhood of the particle, but that’s not a problem for present purposes.

The simplest form of the effective-source scheme – which is the one I use here – then chooses a finite worldtube  $W$  such that the particle is contained in the worldtube’s interior and the puncture and effective source are both defined in a neighborhood of the worldtube, and defines the “numerical” metric perturbation

$$\begin{aligned} \bar{h}_{ab}^{\text{num}} &= \begin{cases} \bar{h}_{ab}^{(\text{residual})} & \text{inside the worldtube} \\ \bar{h}_{ab} & \text{outside the worldtube} \end{cases} \quad (2.6a) \\ &= \begin{cases} \bar{h}_{ab} - \bar{h}_{ab}^{(\text{puncture})} & \text{inside the worldtube} \\ \bar{h}_{ab} & \text{outside the worldtube} \end{cases} \quad (2.6b) \end{aligned}$$

By construction,  $\bar{h}_{ab}^{\text{num}}$  is finite in a neighborhood of the particle,  $C^2$  at the particle and as smooth as  $\bar{h}_{ab}$  elsewhere, obeys the same far-field boundary conditions as  $\bar{h}_{ab}$ , and satisfies the evolution equations

$$\square \bar{h}_{ab}^{\text{num}} + 2R^c{}_a{}^d{}_b \bar{h}_{cd}^{\text{num}} = \begin{cases} S_{ab}^{\text{eff}} & \text{inside the worldtube} \\ 0 & \text{outside the worldtube} \end{cases} \quad (2.7)$$

$\bar{h}_{ab}^{\text{num}}$  has a jump of  $\bar{h}_{ab}^{(\text{puncture})}$  across the worldtube boundary  $\partial W$ , i.e., for any worldtube-boundary point  $x_{\text{bdry}}^i \in \partial W$ ,

$$\lim_{\substack{x^i \rightarrow x_{\text{bdry}}^i \\ x^i \in W}} (\bar{h}_{ab}^{\text{num}}) = \lim_{\substack{x^i \rightarrow x_{\text{bdry}}^i \\ x^i \notin W}} (\bar{h}_{ab}^{\text{num}}) - \bar{h}_{ab}^{(\text{puncture})}(x_{\text{bdry}}^i). \quad (2.8)$$

After numerically solving the evolution equation (2.7) for  $\bar{h}_{ab}^{\text{num}}$ , the physical metric perturbation is given by

$$\bar{h}_{ab} = \begin{cases} \bar{h}_{ab}^{\text{num}} + \bar{h}_{ab}^{(\text{puncture})} & \text{inside the worldtube} \\ \bar{h}_{ab}^{\text{num}} & \text{outside the worldtube} \end{cases} \quad (2.9)$$

Notice that despite the fact that the puncture is only an approximation to the true Detweiler-Whiting singular field, the  $\bar{h}^{\text{num}}$  evolution equations (2.7) (if solved exactly) and the physical-metric-perturbation reconstruction (2.9) together yield an *exact* solution of the  $\mathcal{O}(\mu)$  perturbed Einstein equations (2.3). In a practical computational scheme, the dominant errors come from the numerical solution of the  $\bar{h}^{\text{num}}$  evolution equations (2.7)

### C. The Unstable Gauge Mode

DB13’s analytical solution and numerical experiments show that  $m=1$  time-domain Lorenz-gauge evolutions generically include an unstable gauge mode. This gauge mode induces a metric perturbation  $h_{ab}^{(\text{unstable})}$  that grows linearly with time while (for a suitable numerical evolution scheme) still satisfying the Lorenz gauge conditions (2.2) up to numerical accuracy everywhere away from the particle. DB13’s numerical experiments only included sourced evolutions, but it’s clear from their analytical solution (their equation (131)) that nontrivial homogeneous (source-free) evolutions should exhibit the same instability.

I will use  $\ell=m=1$  metric perturbation of Schwarzschild spacetime as numerical examples of this behavior. As discussed in section III, I parameterize such perturbations by the Barack-Lousto-Sago modes  $\bar{h}^{(I)}$ . I define a (complex) inner product  $\langle \bar{h}_{(A)}^{(I)}, \bar{h}_{(B)}^{(I)} \rangle$  ( $\sum^{(I)}$ ) and associated norm  $\|\bar{h}^{(I)}\|$ , and a pointwise norm  $\|\bar{h}^{(I)}\|$ , on Barack-Lousto-Sago modes.

Figures 1 and 2 show the growth of the unstable gauge mode in three sample  $\ell=m=1$  time-domain Lorenz-gauge evolutions of metric perturbations of Schwarzschild spacetime. All three sample evolutions use the same (arbitrary) initial data, but differ in their source terms: they are, respectively, a homogeneous evolution, a sourced evolution using a point-particle scheme, and a sourced evolution using an effective-source scheme.<sup>4</sup>

For  $t \gtrsim 100M$ ,  $\bar{h}^{(I)}$  in each of these sample evolutions is dominated by the (growing) unstable mode, with the particle-orbit-period oscillations hardly visible. Despite  $\bar{h}^{(I)}$  being large, at late times pointwise norms of the Lorenz gauge constraints ( $\|Y^{(1)}, Y^{(2)}, Y^{(3)}\|$ ) and the independently-computed rescaled Einstein tensor ( $\|\tilde{G}_{ab}\|$ ) are both small at all spatial positions except within a few grid points of the particle (where neither  $Y^{(I)}$  nor  $\tilde{G}_{ab}$  are computed accurately), demonstrating that the unstable mode (i) satisfies the Lorenz gauge constraints and (ii) is in fact a solution of the  $\mathcal{O}(\mu)$  perturbed Einstein equations.<sup>5, 6</sup>

<sup>4</sup> These evolutions are described in detail in section IV; they are, respectively, the **homogeneous**, **sourced-escr**, and **sourced-ppart** evolutions in table I.

<sup>5</sup> The Lorenz-gauge-constraints norm is large early in each evolution because the (arbitrary) initial data doesn’t satisfy the Lorenz gauge constraints. The BL05 evolution system’s gauge constraint damping effectively “radiates away” these early-time constraint violations.

<sup>6</sup>  $\|\tilde{G}_{ab}\|$  is large at early times, but this isn’t surprising: the BL05 evolution system was derived assuming the Lorenz gauge, so there’s no particular reason for it to be correct ( $\|\tilde{G}_{ab}\|$  small) in the presence of large Lorenz gauge constraint violations (as are present early in each evolution).

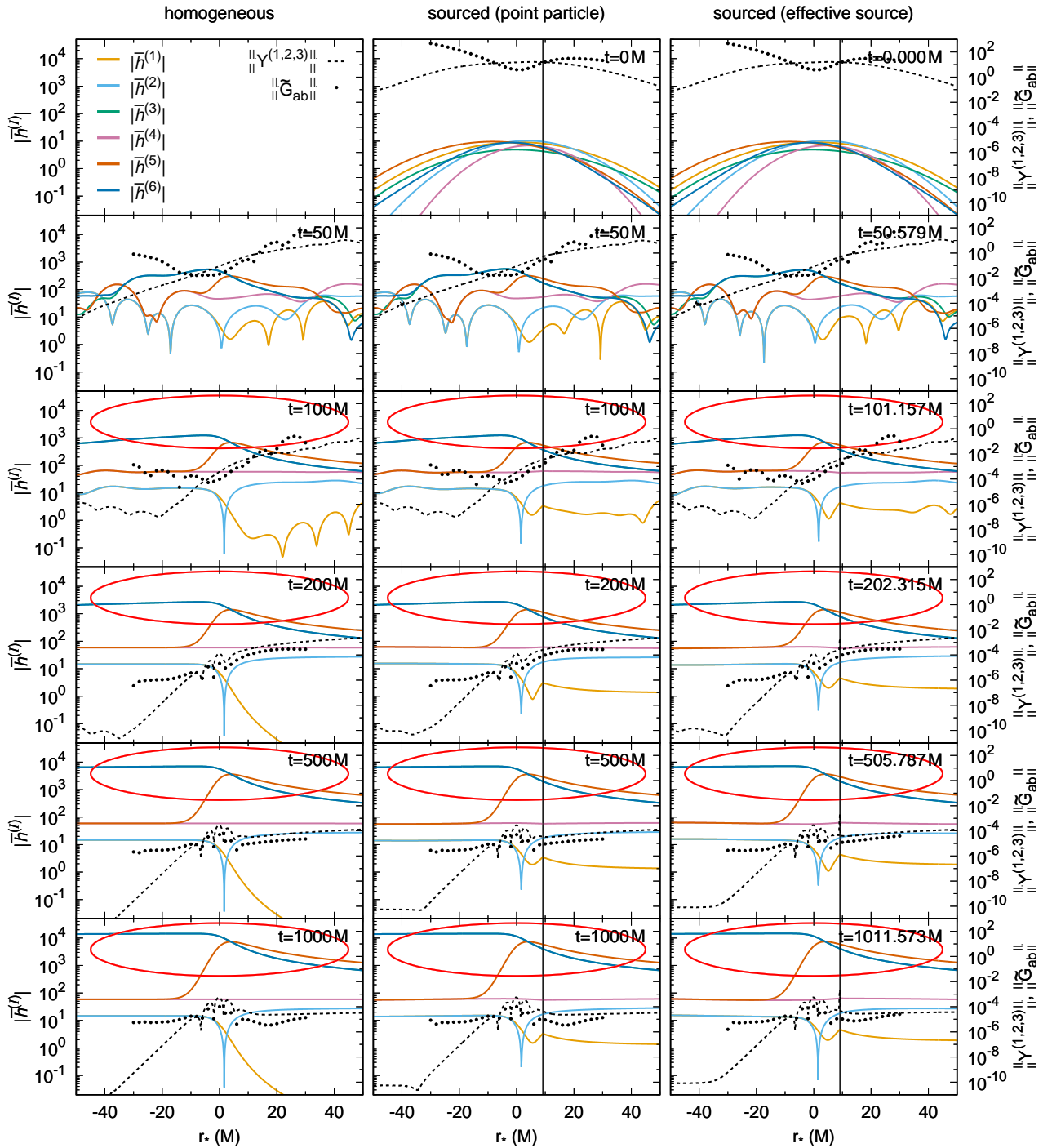


FIG. 1. This figure shows snapshots and a movie of the growth of the unstable gauge mode in three sample  $\ell = m = 1$  evolutions of Schwarzschild metric perturbations. (The evolutions are described in detail in section IV.) The left column shows a homogeneous evolution, the center column shows a sourced evolution using a point-particle scheme, and the right column shows a sourced evolution using an effective-source scheme; the movie shows the sourced point-particle evolution. The same legend (shown in the top left subplot) applies to each subplot. In each subplot and movie frame, the absolute values of the nontrivial Barack-Lousto-Sago metric-perturbation fields  $\bar{h}^{(1)}$ ,  $\bar{h}^{(2)}$ ,  $\bar{h}^{(3)}$ ,  $\bar{h}^{(4)}$ ,  $\bar{h}^{(5)}$ , and  $\bar{h}^{(6)}$  are plotted in color on the left scale, and pointwise norms of the nontrivial Barack-Lousto-Sago Lorenz gauge constraints,  $\|Y^{(1)}, Y^{(2)}, Y^{(3)}\|$  and of the independently-computed rescaled Einstein tensor,  $\|\tilde{G}_{ab}\|$ , are plotted in black on the right scale ( $\|\tilde{G}_{ab}\|$  is only plotted every  $2M$  in  $r_*$ ). For the sourced evolutions, the particle position is marked by a vertical line. Notice that for  $t \gtrsim 100M$  all three evolutions are dominated by the growing unstable mode (shown circled in red), while the Lorenz gauge constraints norm  $\|Y^{(1)}, Y^{(2)}, Y^{(3)}\|$  and the rescaled Einstein tensor norm  $\|\tilde{G}_{ab}\|$  are small everywhere except within a few grid points of the particle in the effective-source evolution (where the constraints and the rescaled Einstein tensor are not computed accurately, for reasons described in section III D 4).

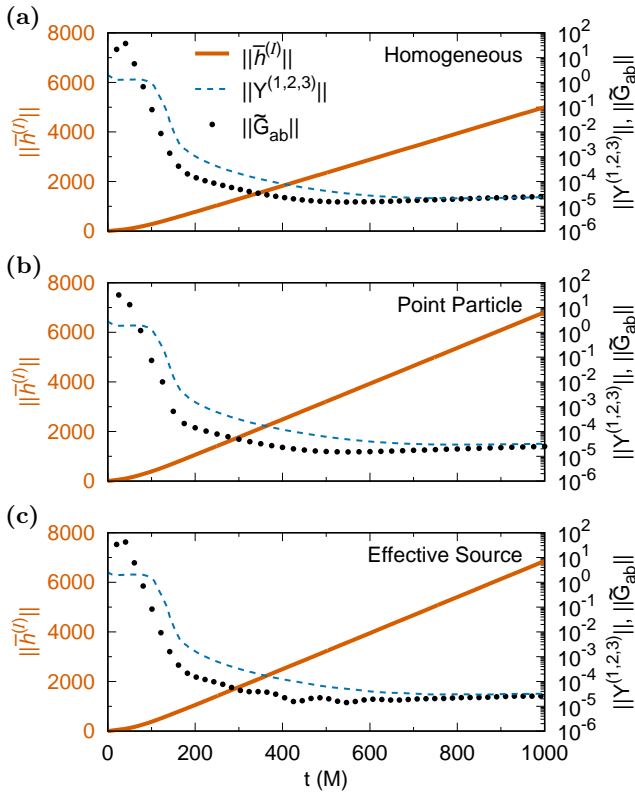


FIG. 2. This figure shows the time evolution of norms over grid points and components in the same three sample evolutions shown in figure 1. Part (a) shows the homogeneous evolution, part (b) shows shows the sourced evolution using a point-particle scheme, and part (c) shows the sourced evolution using an effective-source scheme. The same legend (shown in part (a)) applies to each subplot. In each subplot, a norm of the Barack-Lousto-Sago metric-perturbation fields,  $\|\bar{h}^{(I)}\|$ , is plotted on the left scale, and norms of the Barack-Lousto-Sago Lorenz gauge constraints,  $\|Y^{(1)}, Y^{(2)}, Y^{(3)}\|$ , and the rescaled Einstein tensor,  $\|\tilde{G}_{ab}\|$ , are plotted on the right (logarithmic) scale. Notice that at late times all three evolutions are dominated by the unstable mode ( $\|\bar{h}^{(I)}\|$  is large and growing roughly linearly with time), while the Lorenz gauge constraint norm and the rescaled Einstein tensor norm are both small.

## D. Orthogonalization

### 1. Basic concept

Figure 1 shows that the homogeneous and sourced evolutions have very similar-looking unstable modes at late times. This similarity can be quantified via the inner product and norm of “unit-vector” Barack-Lousto-Sago modes  $\widehat{\bar{h}^{(I)}} := \bar{h}^{(I)} / \|\bar{h}^{(I)}\|$  ( $\sum^A I$ ). By construction,  $\langle \widehat{\bar{h}^{(A)}}, \widehat{\bar{h}^{(B)}} \rangle$  lies between 0 and 1, reaching the latter only when  $\bar{h}^{(A)}$  and  $\bar{h}^{(B)}$  are scalar multiples of each other.

Figure 3 shows that  $\langle \widehat{\bar{h}^{(I)}_{\text{sourced-ppart}}}, \widehat{\bar{h}^{(I)}_{\text{(hom)}}} \rangle$  and

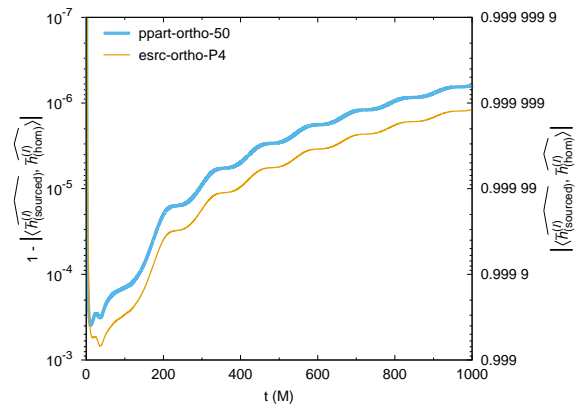


FIG. 3. This figure shows the time evolution of the unit-vector inner products  $\langle \widehat{\bar{h}^{(I)}_{\text{sourced-ppart}}}, \widehat{\bar{h}^{(I)}_{\text{(hom)}}} \rangle$  (thick light-blue curve) and  $\langle \widehat{\bar{h}^{(I)}_{\text{sourced-esrc}}}, \widehat{\bar{h}^{(I)}_{\text{(hom)}}} \rangle$  (thin orange curve) in the same three sample evolutions shown in figure 1. Notice that at late times both unit-vector inner products are very close to 1.

$\langle \widehat{\bar{h}^{(I)}_{\text{sourced-esrc}}}, \widehat{\bar{h}^{(I)}_{\text{(hom)}}} \rangle$  are both very close to 1 at late times,<sup>7</sup> i.e., at late times each sourced evolution is very close to a scalar multiple of the homogeneous evolution. In other words, it appears that at late times each of these evolutions is dominated by (a scalar multiple of) the *same* unstable mode, i.e., there appears to be only a *single* unstable mode.

This suggests the following “orthogonalization” scheme for constructing a sourced Lorenz-gauge evolution which is mostly free of the unstable mode. (Here I describe this scheme for a generic background spacetime; in section III C I specialize to a Schwarzschild background.) First, choose (define) an inner product  $\langle h_{ab}^{(A)}(t), h_{ab}^{(B)}(t) \rangle$  on metric perturbations  $h_{ab}(t)$  in a constant-time slice; this implicitly also defines a norm on metric perturbations in a slice,  $\|h_{ab}(t)\|^2 := \langle h_{ab}(t), h_{ab}(t) \rangle$ .<sup>8</sup>

Now consider the sourced Lorenz-gauge evolution  $h_{ab}^{(\text{sourced})}$  of some nonzero initial data, together with the homogeneous Lorenz-gauge evolution  $h_{ab}^{(\text{hom})}$  of some (possibly-different) nonzero initial data.<sup>9</sup> At late times,

<sup>7</sup> Although it’s difficult to see on the scale of figure 3, both unit-vector inner products are also very close to 1 at early times, but this is “just” a consequence of using the same initial data for the homogeneous and source evolutions, and is not important for my arguments here.

<sup>8</sup> Recall that indices repeated between the two arguments of the inner product are not subject to the Einstein summation convention, so there is no summation over  $ab$  implied in this definition, nor in the definition of  $\|h_{ab}(t)\|^2$ .

<sup>9</sup> In my numerical tests of the orthogonalization scheme I have always used the same (nonzero) initial data for the homogeneous and sourced evolutions, but the orthogonalization scheme doesn’t actually require this.

$h_{ab}^{(\text{hom})}$  is dominated by the unstable gauge mode, i.e.,  $h_{ab}^{(\text{hom})}$  is approximately some scalar multiple of  $h_{ab}^{(\text{unstable})}$ . This suggests defining

$$h_{ab}^{(\text{ortho})} := h_{ab}^{(\text{sourced})} + \lambda h_{ab}^{(\text{hom})}, \quad (2.10)$$

where the (real) scalar  $\lambda$  is chosen so that

$$h_{ab}^{(\text{ortho})} \perp h_{ab}^{(\text{hom})}, \quad (2.11a)$$

or, equivalently,

$$\|h_{ab}^{(\text{ortho})}\| \text{ is minimized.} \quad (2.11b)$$

(These are preliminary definitions; I will redefine  $h_{ab}^{(\text{ortho})}$  in (2.14) below.)

That is,  $h_{ab}^{(\text{ortho})}$  is obtained by Gram-Schmidt orthogonalizing  $h_{ab}^{(\text{sourced})}$  with respect to  $h_{ab}^{(\text{hom})}$ . It's easy to show that the value of  $\lambda$  satisfying (2.11) is

$$\lambda^{(\text{instantaneous})} = - \frac{\langle h_{ab}^{(\text{hom})}, h_{ab}^{(\text{sourced})} \rangle}{\|h_{ab}^{(\text{hom})}\|^2} \left( \sum'_{ab} \right). \quad (2.12)$$

At late times,  $h_{ab}^{(\text{hom})}$  is approximately a scalar multiple of  $h_{ab}^{(\text{unstable})}$ , so orthogonalizing  $h_{ab}^{(\text{sourced})}$  with respect to  $h_{ab}^{(\text{hom})}$  is approximately the same as orthogonalizing  $h_{ab}^{(\text{sourced})}$  with respect to  $h_{ab}^{(\text{unstable})}$ . Therefore, at late times, the orthogonalization (2.11) (which by definition makes  $\langle h_{ab}^{(\text{ortho})}, h_{ab}^{(\text{hom})} \rangle = 0$  and hence  $\langle \widehat{h_{ab}^{(\text{ortho})}}, \widehat{h_{ab}^{(\text{hom})}} \rangle = 0$ ) should make  $\langle \widehat{h_{ab}^{(\text{ortho})}}, \widehat{h_{ab}^{(\text{unstable})}} \rangle$  “small” at late times. In other words,  $h_{ab}^{(\text{ortho})}$  should be approximately free of the unstable mode at late times.

If  $\lambda$  were *not* defined by (2.11) and (2.12), but were instead a fixed constant (independent of time), then because

- (i) the Lorenz gauge condition (2.2) and the  $O(\mu)$  Lorenz-gauge perturbed Einstein equations (2.3) are both *linear* in the metric perturbation,
- (ii)  $h_{ab}^{(\text{sourced})}$  is an inhomogeneous solution of the  $O(\mu)$  Lorenz-gauge perturbed Einstein equations (2.3), and
- (iii)  $h_{ab}^{(\text{hom})}$  is a *homogeneous* solution of the  $O(\mu)$  Lorenz-gauge perturbed Einstein equations (2.3),

it would necessarily follow that for any fixed  $\lambda$ ,  $h_{ab}^{(\text{ortho})}$  as defined by the linear combination (2.10)

- (1) would be an inhomogeneous solution of the Lorenz-gauge  $O(\mu)$  perturbed Einstein equations (2.3) with the same source terms as  $h_{ab}^{(\text{sourced})}$ , and

(2) would satisfy the Lorenz gauge conditions (2.2).

However, in general,  $\lambda$  as defined by (2.11) and (2.12) is time-dependent, so substituting  $h_{ab}^{(\text{ortho})}$  into the Lorenz gauge condition (2.2) and the  $O(\mu)$  perturbed Einstein equations (2.3) gives extra  $\partial_t \lambda$  and  $\partial_{tt} \lambda$  terms, causing  $h_{ab}^{(\text{ortho})}$  to not satisfy either of the conditions (1) or (2) above.<sup>10</sup>

Therefore, my orthogonalization scheme actually uses a *piecewise-constant-in-time*  $\lambda$  which is “occasionally” updated from  $\lambda^{(\text{instantaneous})}$  at some discrete times  $0 < t_1 < t_2 < t_3 < \dots$  during the evolution. That is, I define

$$\lambda^{(\text{occasionally updated})}(t) = \lambda^{(\text{instantaneous})}([t]_{\{t_k\}}) \quad (2.13)$$

where  $[t]_{\{t_k\}}$  is the largest  $t_k \leq t$ . I then redefine  $h_{ab}^{(\text{ortho})}$  as

$$h_{ab}^{(\text{ortho})}(t) = h_{ab}^{(\text{sourced})}(t) + \lambda^{(\text{occasionally updated})}(t) h_{ab}^{(\text{hom})}(t). \quad (2.14)$$

With this scheme, in general,  $\lambda^{(\text{occasionally updated})}$  and  $h_{ab}^{(\text{ortho})}$  have jump discontinuities at each time  $t = t_k$ , but the conditions (1) and (2) above are satisfied within each time interval  $t_k < t < t_{k+1}$ .

The orthogonality conditions (2.11) are satisfied exactly at each time  $t = t_k$ , so the arguments given above that  $\langle \widehat{h_{ab}^{(\text{ortho})}}, \widehat{h_{ab}^{(\text{unstable})}} \rangle$  should be “small” still apply at late times in the sequence  $t \in \{t_k\}$ . Hence, if  $t_{k+1} - t_k$  (the time between orthogonalizations) is bounded as  $t \rightarrow \infty$ , and  $\langle \widehat{h_{ab}^{(\text{ortho})}}, \widehat{h_{ab}^{(\text{unstable})}} \rangle$  doesn't grow too rapidly within each time interval  $t_k < t < t_{k+1}$ , then  $\langle \widehat{h_{ab}^{(\text{ortho})}}, \widehat{h_{ab}^{(\text{unstable})}} \rangle$  should be “small” (i.e.,  $h_{ab}^{(\text{ortho})}$  should be “mostly” free of the unstable mode) at *all* late times.

One concern with the orthogonalization scheme is that it requires a numerical cancellation of the unstable mode between the (independent) sourced and homogeneous evolutions, and this cancellation becomes more difficult to achieve numerically – i.e., the cancellation becomes more sensitive to small (numerical) relative errors in the evolutions – as the unstable mode grows larger at late times. Fortunately, the unstable mode grows only linearly with time; if it grew exponentially with time the required numerical cancellation would soon become impractical. In practice, I find that the unstable mode

<sup>10</sup> I have confirmed numerically that if  $\lambda$  is updated “continuously” (i.e., at each time step) then  $h_{ab}^{(\text{ortho})}$  doesn't satisfy the  $O(\mu)$  Lorenz-gauge perturbed Einstein equations (2.3). In particular, for the `ppart-ortho-cont` and `esrc-ortho-cont` evolutions in table I,  $\|\tilde{G}_{ab}\|$  is typically 4–6 orders of magnitude larger than in the other orthogonalized evolutions in table I, and these large values do *not* decrease at higher numerical resolutions.

grows sufficiently slowly that the numerical cancellation is achievable to a reasonable accuracy.<sup>11</sup>

## 2. Design choices

There are two major design choices in the orthogonalization scheme:

- The choice of the inner product, which in turn defines the meaning of “ $\perp$ ” and “ $\|\cdot\|$ ” in (2.11). I discuss the choice of inner product in section III C 1.
- The choice of the orthogonalization times  $\{t_k\}$ . The simplest choice, and the one I have used for all the numerical tests reported here, is to make the orthogonalization times uniformly spaced in time,  $t_k = k \Delta t^{(\text{ortho})}$ .<sup>12</sup>

If the particle orbit is periodic (e.g., any geodesic on a Schwarzschild background, or any equatorial geodesic on a Kerr background), it may be useful to choose the orthogonalization time spacing  $\Delta t^{(\text{ortho})}$  to integrally divide the orbital period  $P$ , so that  $\lambda$  is updated at the same set of orbital phases in each orbit. This makes orbit-to-orbit comparisons of  $\lambda^{(\text{occasionally updated})}$  and  $h_{ab}^{(\text{ortho})}$  easier, and is particularly useful if used in combination with the orbit-averaging scheme discussed in appendix C 2).

## 3. Physical Meaning of Re-Orthogonalization

What is the physical meaning of re-orthogonalization, i.e., of the jump discontinuity in  $h_{ab}^{(\text{ortho})}$  at each time  $t = t_k$ ? In particular, is re-orthogonalization purely a change of gauge (allowing  $h_{ab}^{(\text{ortho})}$  to be interpreted as the continuous time-evolution of the slices  $\Sigma_t$  of a single

physical spacetime), or does  $h_{ab}^{(\text{ortho})}$  immediately (infinitesimally) after  $t = t_k$  represent a physically distinct  $t = \text{constant}$  hypersurface from  $h_{ab}^{(\text{ortho})}$  immediately (infinitesimally) before  $t = t_k$ ?

To answer this question, observe first that the DB13 unstable mode is a pure Lorenz gauge mode. By virtue of the definition (2.14), the jump in  $h_{ab}^{(\text{ortho})}$  induced by re-orthogonalizing (i.e., by updating  $\lambda^{(\text{occasionally updated})}$ ) is a scalar multiple of  $h_{ab}^{(\text{hom})}$ . Thus, to the extent that the late-time  $h_{ab}^{(\text{hom})}$  is dominated by the unstable mode, the jump in  $h_{ab}^{(\text{ortho})}$  induced by re-orthogonalization is approximately a scalar multiple of the unstable mode, and thus this jump corresponds approximately to a change of (Lorenz) gauge.

It would be interesting to try to explicitly verify this numerically, either by comparing curvature invariants across re-orthogonalization, and/or by attempting to explicitly construct the re-orthogonalization gauge transformation. I have not done either of these.

However, the numerical results presented here<sup>13</sup> do establish (for the tests cases considered here) that at late times, re-orthogonalization preserves the Lorenz gauge condition, i.e., re-orthogonalization does *not* significantly increase the numerical violations of the  $h_{ab}^{(\text{ortho})}$  Lorenz gauge constraints. This is consistent with the above argument that at late times, re-orthogonalization is approximately a change of gauge within the Lorenz gauge family.

## III. SCHWARZSCHILD SPACETIME

For an initial test of the orthogonalization scheme, I take the background spacetime to be Schwarzschild spacetime of mass  $M$  with the usual Schwarzschild coordinates  $(t, r, \theta, \phi)$ , so that the line element is

$$ds^2 = -f dt^2 + f^{-1} dr^2 + r^2(d\theta^2 + \sin^2\theta d\phi^2), \quad (3.1)$$

where  $f = 1 - 2M/r$ . I introduce the usual Schwarzschild tortoise coordinate

$$r_* = r + 2M \ln \left| \frac{r}{2M} - 1 \right|, \quad (3.2)$$

as well as the null coordinates

$$u = t - r_* \quad (3.3a)$$

$$v = t + r_* \quad (3.3b)$$

My numerical scheme requires inverting (3.2) to find  $r$  as a function of  $r_*$ ; I describe this computation in appendix B 1.

<sup>11</sup> In numerical analysis, the Gram-Schmidt process is considered to be numerically somewhat unstable (see, e.g., Golub and Van Loan [21, section 5.2.7–5.2.9]), but this instability doesn’t seem to significantly affect my application. That is, in practice, I find that immediately after updating  $\lambda^{(\text{occasionally updated})}$ , the numerically-computed unit-vector inner product magnitude  $\left| \langle \widehat{h}_{(\text{ortho})}^{(I)}, \widehat{h}_{(\text{hom})}^{(I)} \rangle \right|$  (which would be 0 in an exact computation and is nonzero only due to floating-point roundoff in the Gram-Schmidt process) is as small as could be expected, i.e.  $\mathcal{O}(\varepsilon \|\widehat{h}_{(\text{ortho})}^{(I)}\|)$ . This means that the numerical inaccuracy of Gram-Schmidt orthogonalization makes only a minute contribution to the value of  $\left| \langle \widehat{h}_{(\text{ortho})}^{(I)}, \widehat{h}_{(\text{hom})}^{(I)} \rangle \right|$  at typical times between  $\lambda^{(\text{occasionally updated})}$  updates (shown, e.g., in figures 7, 11, and 17).

<sup>12</sup> Another possibility would be to choose the  $\{t_k\}$  adaptively, monitoring  $\langle \widehat{h}_{(\text{ortho})}^{(I)}, \widehat{h}_{(\text{hom})}^{(I)} \rangle$  during the evolution and re-orthogonalizing each time this inner product exceeds some chosen threshold. I haven’t tried this.

<sup>13</sup> See, for example, the left column of figures 6 and 10.

### A. $\ell m$ decomposition

Following BL05 and BS07, I decompose the trace-reversed metric perturbation  $\bar{h}_{ab}$  using the Barack-Lousto-Sago basis of tensor spherical-harmonic

modes  $Y_{ab}^{(I\ell m)}$ ,

$$\bar{h}_{ab}(t, r, \theta, \phi) = \frac{\mu}{r} \sum_{\ell, m} \sum_I a^{(I)} \bar{h}^{(I\ell m)}(t, r) Y_{ab}^{(I\ell m)}(r, \theta, \phi), \quad (3.4)$$

where the fixed coefficients  $a^{(I)}$  (given explicitly by BL05's equation (9)) are chosen for convenience, and the Barack-Lousto-Sago tensor-spherical-harmonic basis functions  $Y_{ab}^{(I\ell m)}$  are given explicitly by BL05's equations (A1), (A2), and (A3), with the definitions of  $\bar{h}^{(3\ell m)}$  and  $Y_{ab}^{(3\ell m)}$  modified as per BS07's note 37,

$$\left( \bar{h}^{(3\ell m)} \text{ in BS07 and this work} \right) = f^{-1} \left( \bar{h}^{(3\ell m)} \text{ in BL05} \right) \quad (3.5a)$$

$$\left( Y_{ab}^{(3\ell m)} \text{ in BS07 and this work} \right) = f \left( Y_{ab}^{(3\ell m)} \text{ in BL05} \right). \quad (3.5b)$$

The metric perturbation  $h_{ab}$  and the trace-reversed metric perturbation  $\bar{h}_{ab}$  are (by definition) real, but the fields  $\bar{h}^{(I\ell m)}$  are complex fields.

I numerically evolve the fields  $\bar{h}^{(I\ell m)}$  using a Cauchy evolution scheme in  $(t, r_*)$  coordinates. BL05 write the evolution and Lorenz gauge constraint equations in terms of the partial derivatives  $\partial_r \bar{h}^{(I\ell m)}$  (at constant  $t$ ) and  $\partial_v \bar{h}^{(I\ell m)}$  (at constant  $u$ ); for my numerical scheme I transform these into  $\partial_{r_*} \bar{h}^{(I\ell m)}$  and  $\partial_{r_* r_*} \bar{h}^{(I\ell m)}$  (both at constant  $t$ ) and  $\partial_t \bar{h}^{(I\ell m)}$  (at constant  $\{r, r_*\}$ ) via

$$\partial_r \bar{h} \text{ at constant } t = f^{-1} \partial_{r_*} \bar{h} \quad (3.6a)$$

$$\partial_v \bar{h} \text{ at constant } u = \frac{1}{2} \partial_t \bar{h} + \frac{1}{2} \partial_{r_*} \bar{h}. \quad (3.6b)$$

For each  $(\ell, m)$ , the  $(t, r_*)$ -coordinate evolution equations for the fields  $\bar{h}^{(I\ell m)}$  are

$$\partial_{tt} \bar{h}^{(I)} = \text{RHS}_{(\text{vacuum})}^{(I)}(\bar{h}^{(J)}) + 4\mathcal{S}^{(I)} \quad (3.7a)$$

$$=: \text{RHS}^{(\text{total})^{(I)}}(\bar{h}^{(J)}), \quad (3.7b)$$

where both  $\text{RHS}_{(\text{vacuum})}^{(I)}$  and  $\text{RHS}^{(\text{total})^{(I)}}$  are spatial differential operators, and where the factor of 4 multiplying the source term in (3.7a) accounts for my use of a different normalization convention for the  $\square$  operator than BL05.

In more detail, the vacuum right-hand-side operator is given by

$$\begin{aligned} \text{RHS}_{(\text{vacuum})}^{(I)}(\bar{h}^{(J)}) &= \partial_{r_* r_*} \bar{h}^I - V \bar{h}^{(I)} \\ &\quad - 4\mathcal{M}^I(\bar{h}^J, \partial_{r_*} \bar{h}^{(J)}, \partial_t \bar{h}^{(J)}), \end{aligned} \quad (3.7c)$$

where the potential  $V = V(r)$  is given by

$$V(r) = f \left[ \frac{\partial_r f}{r} + \frac{\ell(\ell+1)}{r^2} \right], \quad (3.7d)$$

and where  $\mathcal{M}$  is a linear coupling operator which mixes the different Barack-Lousto-Sago modes indexed by  $(I)$  but doesn't mix the tensor-spherical-harmonic indices  $(\ell m)$ .  $\mathcal{M}$  is given explicitly by BL05's equation (18) if BL05's main gauge constraint damping terms are included,<sup>14</sup> or by BL05's equation (C1) if gauge constraint damping is omitted. The source term  $\mathcal{S}$  models the particle and is described in section III B.

Since the evolution equations (3.7) don't mix the  $(\ell, m)$ , each  $(\ell, m)$  may be evolved independently. For  $\ell = m = 1$ ,  $Y_{ab}^{(I\ell m)}$  is nontrivial only for  $I \in \{1, 2, 3, 4, 5, 6\}$ .

In terms of the fields  $\bar{h}^{(I\ell m)}(t, r)$ , the Lorenz gauge conditions (constraints) (2.2) are given by BL05's equation (16), again modified to use the BS07 definition (3.5) of  $\bar{h}^{(3\ell m)}$ . I refer to the mode-decomposed Lorenz gauge conditions (BL05's  $H_a^{(\ell m)}$ , defined as the left-hand-side fields in BL05's equation (16)) as  $Y^{(a)} = Y^{(a)}(t, r_*)$ , with the dependence on  $\ell m$  being implicit. For  $\ell = m = 1$ ,  $Y^{(a)}$  is nontrivial only for  $a \in \{1, 2, 3\}$ .

In the usual terminology of numerical relativity (see, e.g., Bona and Palenzuela-Luque [11, chapter 3] or Alcubierre [2, section 2.6]), the BL05/BS07 evolution system is a free evolution with (Lorenz-gauge) constraint damping.

Appendix B describes my numerical scheme for (approximately) time-integrating the evolution equations (3.7).

<sup>14</sup> BL05's equation (18) incorporates a slightly different gauge-constraint damping scheme than that described by BL05 in the two paragraphs immediately prior to their equation (17). All the results presented here use BL05's equation (18).

## B. Modelling the Particle

I take the particle to be in a circular geodesic orbit at coordinate radius  $r = r_p$ , with angular velocity  $\omega = \sqrt{M/r_p^3}$  and (coordinate) orbital period  $P = 2\pi/\omega$ .

All the numerical results presented here use  $r_p = 7.2M$ , so that  $P \approx 121.389M$ .

### 1. Point-Particle Scheme

The simplest way to model the particle is as a point particle with the  $\delta$ -function stress-energy tensor given by BL05's equation (5). The corresponding source terms in the BL05 evolution equation (17) are given by BL05's equations (29) and (30).

Because of the  $\delta$ -function source term, the fields  $\bar{h}^{(I\ell m)}$  and their time derivatives are only  $C^0$  across the particle,<sup>15</sup> while spatial derivatives of  $\bar{h}^{(I\ell m)}$  have (time-dependent) jumps across the particle. I calculate these jumps using the scheme described in appendix A. Once these jumps are known, I use them in the finite differencing scheme as described in appendix B 5 a.

### 2. Effective Source

Alternatively, the particle may be modelled using an effective-source scheme. Compared to a point-particle scheme, an effective-source scheme is more complicated, but generalizes readily to 2+1- or 3+1-dimensional numerical evolutions.

Using an effective-source scheme, for each  $(\ell, m)$  the  $\bar{h}^{(I\ell m)}$  evolution equations (3.7) become

$$\partial_{tt}\bar{h}_{\text{num}}^{(I)} = \text{RHS}_{(\text{vacuum})}^{(I)} + \begin{cases} 4S_{\text{eff}}^{(I)} & \text{inside the worldtube} \\ 0 & \text{outside the worldtube} \end{cases}, \quad (3.8)$$

with the corresponding jump conditions across the worldtube boundary

$$\bar{h}_{\text{num}}^{(I)} = \begin{cases} \bar{h}_{(\text{residual})}^{(I)} & \text{inside the worldtube} \\ \bar{h}^{(I)} & \text{outside the worldtube} \end{cases} \quad (3.9a)$$

$$= \begin{cases} \bar{h}^{(I)} - \bar{h}_{(\text{puncture})}^{(I)} & \text{inside the worldtube} \\ \bar{h}^{(I)} & \text{outside the worldtube} \end{cases}. \quad (3.9b)$$

I describe the implementation of these jump conditions at the finite-differencing level in appendix B 5 b.

<sup>15</sup> This uses the fact that the particle is in a *circular* orbit; for a noncircular orbit the time derivatives would, in general, also have jumps across the particle.

If the initial data doesn't already satisfy the jump conditions (3.9) across the worldtube boundary, the dynamical evolution quickly drives the  $\bar{h}^{(I)}$  (and  $\partial_t\bar{h}^{(I)}$ ) into a configuration satisfying the jump conditions. However, this process tends to generate high-spatial-frequency noise in the  $\bar{h}^{(I)}$ , which can reduce the accuracy of the numerical computation. In appendix C 3 I discuss a possible scheme (which turns out not to work well) for reducing the amount of this high-spatial-frequency noise by gradually turning on the puncture at the start of the evolution.

## C. Orthogonalization

DB13 found that only the  $\ell = m = 1$  evolutions suffer from the unstable gauge mode, so hereinafter I restrict my attention to the  $\ell = m = 1$  case, and I drop the indices  $\ell m$ .

Rather than orthogonalizing the metric perturbation  $h_{ab}$  itself, my code instead actually orthogonalizes the Barack-Lousto-Sago  $\bar{h}^{(I)}$  fields. Since the  $\bar{h}^{(I)}$  are complex fields, I choose (define) a complex inner product  $\langle \bar{h}_{(A)}^{(I)}, \bar{h}_{(B)}^{(I)} \rangle$  on  $\bar{h}^{(I)}$  fields.<sup>16, 17</sup> This implicitly also defines a norm on  $\bar{h}^{(I)}$  fields,  $\|\bar{h}^{(I)}\|^2 := \langle \bar{h}^{(I)}, \bar{h}^{(I)} \rangle$ .

The remaining description of section IID still applies, i.e., I initially define

$$\bar{h}_{(\text{ortho})}^{(I)} := \bar{h}_{(\text{sourced})}^{(I)} + \lambda \bar{h}_{(\text{hom})}^{(I)}, \quad (3.10)$$

where  $\lambda$  is now a *complex* scalar, chosen so that

$$\bar{h}_{(\text{ortho})}^{(I)} \perp \bar{h}_{(\text{hom})}^{(I)}, \quad (3.11a)$$

or, equivalently,

$$\|\bar{h}_{(\text{ortho})}^{(I)}\| \text{ is minimized.} \quad (3.11b)$$

The value of  $\lambda$  satisfying (3.11) is

$$\lambda^{(\text{instantaneous})} = - \frac{\langle \bar{h}_{(\text{hom})}^{(I)}, \bar{h}_{(\text{sourced})}^{(I)} \rangle}{\|\bar{h}_{(\text{hom})}^{(I)}\|^2} \quad \left( \not\propto^{(I)} \right). \quad (3.12)$$

$\lambda^{(\text{occasionally updated})}$  is still defined by (2.13), and my final redefinition of  $\bar{h}_{(\text{ortho})}^{(I)}$  is

$$\bar{h}_{(\text{ortho})}^{(I)}(t) := \bar{h}_{(\text{sourced})}^{(I)}(t) + \lambda^{(\text{occasionally updated})}(t) \bar{h}_{(\text{hom})}^{(I)}(t). \quad (3.13)$$

<sup>16</sup> Recall that indices repeated between the two arguments of the inner product are *not* subject to the Einstein summation convention, e.g., there is no summation over  $I$  implied in this definition, or in the definition of  $\|\bar{h}^{(I)}\|^2$ .

<sup>17</sup> To be clear, this is the inner product between one set of the 6 nontrivial  $\bar{h}^{(I)}$  fields, and another set of the 6 nontrivial  $\bar{h}^{(I)}$  fields,  $\langle \bar{h}_{(A)}^{(1,2,3,4,5,6)}, \bar{h}_{(B)}^{(1,2,3,4,5,6)} \rangle$ .

### 1. Choice of Inner Product

I have experimented with several different choices of inner product.

The fundamental requirement for the inner product is that it should “see” the unstable mode. Figure 1 shows that the unstable mode has a large amplitude throughout the plotted range  $r_* \in [-50M, +50M]$ , so the inner product should include (at least most of) this region. The  $\bar{h}^{(I)}$  near the inner/outer grid boundaries are strongly influenced by my non-physical inner/outer boundary conditions (described in appendix B6), so I exclude these regions from the inner product.

An important consideration in choosing the inner product is how the region near the particle should be handled. The physical metric perturbation may be singular at the particle, which both makes it difficult to define a sensible inner product there and runs the risk of the near-particle contributions dominating the remainder of the computational domain. Therefore, I always exclude the near-particle region from the inner product.

In practice, I choose the inner product to depend on the  $\bar{h}^{(I)}$  (only) within the region  $r_* \in X - Y$ , where  $X = [-100M, 100M]$  and  $Y$  is a region near the particle, as described below.<sup>18,19</sup>

To this end, a simple definition for the inner product is the (complex) Euclidean inner product on Barack-Lousto-Sago  $\bar{h}^{(I)}$  fields,

$$\langle \bar{h}_{(A)}^{(I)}, \bar{h}_{(B)}^{(I)} \rangle := \frac{1}{N} \sum_{\mathbf{i} \in X-Y} \sum_I \text{conj} \left[ \left( \bar{h}_{(A)}^{(I)} \right)_{\mathbf{i}} \right] \left( \bar{h}_{(B)}^{(I)} \right)_{\mathbf{i}}, \quad (3.14)$$

where  $\mathbf{i}$  indexes grid points,  $N$  is the actual number of grid points in the set  $X-Y$ , and  $Y$  (the near-particle region excluded from the inner product) is the set of all grid points which either (i) are within the worldtube (if an effective source is being used), or (ii) are within a finite-difference molecule radius of the particle (if a point-particle model is being used).

Unfortunately, when doing convergence tests which compare orthogonalized evolutions at different finite-differencing resolutions  $\Delta r_*$  (discussed in detail in appendix D), using the inner product (3.14) results in  $\lambda$  and  $\bar{h}_{(\text{ortho})}^{(I)}$  showing only slow ( $\mathcal{O}(\Delta r_*)$ ) convergence to a continuum limit. There are two reasons for this slow convergence:

<sup>18</sup> It would be interesting to try values other than  $r_* = \pm 100M$  for the endpoints of the  $X$  interval, and/or to try making  $X$  non-symmetric about  $r_* = 0$ . I haven’t tried either of these.

<sup>19</sup> It might also be interesting to try making the cutoff of the inner product outside  $X$  gradual rather than abrupt, i.e., weighting the inner product with a weight function which smoothly decreases from 1 for  $r_* \in X$  to very small values at large  $|r_*|$ . Such an inner product should respond more smoothly than my present inner product when outgoing radiation crosses the boundary of the  $X$  region. I haven’t tried this.

- The set of near-particle grid points  $Y$  varies with  $\Delta r_*$ .
- Viewing the sum over grid points in (3.14) as an approximation to the integral 3.15 below, (3.14) is the rectangle-rule approximation (the Riemann sum), which generically has an  $\mathcal{O}(\Delta r_*)$  error in approximating the integral.

To allow faster (higher order) convergence, I now instead define the inner product as the integral

$$\langle \bar{h}_{(A)}^{(I)}, \bar{h}_{(B)}^{(I)} \rangle := \int_{X-Y} \left( \sum_I \text{conj} \left[ \left( \bar{h}_{(A)}^{(I)} \right) \right] \left( \bar{h}_{(B)}^{(I)} \right) \right) dr_*, \quad (3.15)$$

where the set  $Y$  is now chosen to be independent of  $\Delta r_*$ . In particular, I choose  $Y$  as follows:

- Start with an  $r_*$  interval which is the worldtube (if an effective-source scheme is being used), or which is a single point at the particle (if a point-particle scheme is being used).
- Then, widen this interval by moving each of its endpoints outwards by a macroscopic distance  $(\delta r_*)_{\text{widen}}$  (chosen to be larger than any finite-difference molecule radius).
- Finally, quantize the widened interval by rounding each of its endpoints outwards to an integer multiple of some macroscopic distance  $(\delta r_*)_{\text{quantize}}$ , chosen to be an integer multiple of the least common multiple of all the grid spacings  $\Delta r_*$  used in convergence tests (cf. appendix D).

With this definition, the inner product only “sees” the physical metric perturbation outside a neighborhood of the particle (and outside a neighborhood of the worldtube if an effective-source scheme is being used),  $X$  and  $Y$ ’s endpoints are (i.e., coincide with) grid points, and  $X$  and  $Y$ ’s endpoints are both independent of the grid spacing  $\Delta r_*$ . Table II gives the values of  $(\delta r_*)_{\text{widen}}$  and  $(\delta r_*)_{\text{quantize}}$  used in my numerical tests of the orthogonalization scheme.

For numerical calculation, I approximate the integral (3.15) using Simpson’s rule, which generically has an  $\mathcal{O}((\Delta r_*)^4)$  error term, allowing for up to 4th order convergence of  $\lambda$  and  $\bar{h}_{(\text{ortho})}^{(I)}$ . I discuss convergence tests in detail in appendix D.

### 2. Choice of Orthogonalization times

I have experimented with a number of choices for the orthogonalization time spacing  $\Delta t^{(\text{ortho})}$ . Here I present results for  $\Delta t^{(\text{ortho})} = 50M$ ,  $\Delta t^{(\text{ortho})} = P/4 \approx 30.347M$ , and  $\Delta t^{(\text{ortho})} = P/12 \approx 10.116M$ .

### D. Diagnostics

Because the Lorenz gauge condition (2.2) doesn't fully specify the gauge,  $\bar{h}_{(\text{ortho})}^{(I)}$  is generally not in the same gauge as an  $\bar{h}^{(I)}$  computed by some other method (e.g., a frequency-domain method). This makes a direct cross-method comparison of  $\bar{h}^{(I)}$  difficult.

Instead, I assess the orthogonalization scheme by numerically testing that at late times (when  $\bar{h}_{(\text{hom})}^{(I)}$  is dominated by the unstable mode), the following criteria are satisfied:

- In between orthogonalization times,  $\bar{h}_{(\text{ortho})}^{(I)}$  should satisfy the  $O(\mu)$  Lorenz-gauge perturbed Einstein equations (2.3). I assess this by testing that the independently-computed  $\mathcal{O}(\mu)$  perturbed Einstein tensor  $\tilde{G}_{ab}$  (described in detail in section III D 1) is small and converges towards zero as the numerical resolution is increased. (I discuss convergence tests in appendix D.)
- In between orthogonalization times,  $\bar{h}_{(\text{ortho})}^{(I)}$  should satisfy the  $O(\mu)$  Lorenz gauge condition (2.2), i.e., the Lorenz gauge constraints  $Y^{(1)}$ ,  $Y^{(2)}$ , and  $Y^{(3)}$  should all be small, and should converge towards zero as the numerical resolution is increased.
- $\bar{h}_{(\text{ortho})}^{(I)}$  should contain only a relatively small component of the unstable mode. Since  $\bar{h}_{(\text{hom})}^{(I)}$  is dominated by the unstable mode at late times, I operationalize this criterion as the requirement that  $\langle \bar{h}_{(\text{ortho})}^{(I)}, \bar{h}_{(\text{hom})}^{(I)} \rangle$  should be “small”, say  $\lesssim 0.4$ .

#### 1. Independent computation of the Einstein tensor

To assist in verifying the correctness of the evolution equations, and to verify that the orthogonalization scheme yields correct evolutions, I find it very useful to have an independently-programmed computation of the  $\mathcal{O}(\mu)$  perturbed Einstein tensor  $G_{ab}$  defined (everywhere away from the particle) by (2.1).

$G_{ab}$  depends on all 4 spatial coordinates  $(t, r, \theta, \phi)$ , but for  $\ell = m = 1$  the angular dependence of  $G_{ab}$  can be separated by multiplying each  $(t, r, \theta, \phi)$ -coordinate tensor component of  $G_{ab}$  by the corresponding component of

$$S_{ab}^{(\theta\phi)} = \begin{bmatrix} S^{-1} & S^{-1} & C^{-1} & S^{-1} \\ * & S^{-1} & C^{-1} & S^{-1} \\ * & * & S^{-1} & 1 \\ * & * & * & S^{-3} \end{bmatrix}, \quad (3.16)$$

where

$$S = e^{i\phi} \sin \theta \quad (3.17a)$$

$$C = e^{i\phi} \cos \theta, \quad (3.17b)$$

and where  $*$  denotes components determined by symmetry. That is, the component-by-component product  $S_{ab}^{(\theta\phi)} \times G_{ab}$  has no angular dependence.

To obtain components which neither blow up nor vanish at the horizon, I then further rescale  $S_{ab}^{(\theta\phi)} \times G_{ab}$  by multiplying each of its components by the corresponding component of

$$S_{ab}^{(r)} = \begin{bmatrix} R & R^2 & R & R \\ * & R^3 & R^2 & R^2 \\ * & * & R^2 & 1 \\ * & * & * & R^2 \end{bmatrix}, \quad (3.18)$$

where  $R = r - 2M$ . I define the resulting “rescaled” Einstein tensor as

$$\tilde{G}_{ab} = S_{ab}^{(r)} \times S_{ab}^{(\theta\phi)} \times G_{ab}, \quad (3.19)$$

and use this, and norms over coordinate components of  $\tilde{G}_{ab}$  at an event ( $\|\tilde{G}_{ab}\|$ ) and over components and grid points ( $\|\tilde{G}_{ab}\|$ ), as diagnostics.

For the work described here, I generated formulas for each  $\tilde{G}_{ab}$  component as a function of the  $\bar{h}^{(I)}$  and their 1st and 2nd spacetime partial derivatives, directly from (2.1) by using the SageManifolds package (Gourgoulhon et al. [22] and Gourgoulhon and Mancini [23]) in the open-source Sage symbolic computation system (Eröcal and Stein [18], Stein and Joyner [30], and The Sage Developers [32]). In my implementation, this computation suffers from numerical cancellations for  $r_* \ll 0$  or  $r_* \gg 0$ , so I limit the Einstein-tensor computation to the range  $r_* \in [-30M, +30M]$ .

#### 2. Diagnostic Norms

I use pointwise norms  $\|\cdot\|$  (i.e., norms over coordinate components, computed independently at each grid point) to assess the spatial variation of diagnostics (e.g., in figures 1, 6, and 10). In particular,

- I define  $\|Y^{(1,2,3)}\|$  to be the RMS of  $Y^{(1)}$ ,  $Y^{(2)}$ , and  $Y^{(3)}$ .
- I define  $\|\tilde{G}_{ab}\|$  to be  $\sqrt{|\tilde{G}_{ab}| |\tilde{G}^{ab}|}$ .

I also use gridwise norms  $\|\cdot\|$  (i.e., norms across an entire set of grid points and coordinate components), particularly when assessing the temporal variation of diagnostics and for convergence tests (appendix D). In particular,

- I define  $\|Y^{(1,2,3)}\|$  and  $\|\bar{h}_{(\text{ortho})}^{(I)}\|$  as the inner-product norm (described in detail in section III C 1).
- For historical reasons, my code only computes  $\tilde{G}_{ab}$  on a fixed and relatively coarsely-spaced set of grid points (spacing  $1M$  in  $r_*$  for all the results reported

here), independent of the numerical resolution. This set doesn't provide enough information to accurately compute the inner-product integral 3.15. Instead, I define  $\|\tilde{G}_{ab}\|$  to be the RMS over grid points of  $\|\tilde{G}_{ab}\|$ .

### 3. Computation of Time Derivatives for Diagnostics

In order for the calculation of diagnostics (in particular, the Lorenz gauge constraints  $Y^a$  and the rescaled Einstein tensor  $\tilde{G}_{ab}$ ) to be fully independent of my implementation of the Barack-Lousto-Sago evolution system for the  $\bar{h}^{(I)}$ , my code calculates  $Y^a$  and  $\tilde{G}_{ab}$  using  $\partial_t \bar{h}^{(I)}$  and  $\partial_{tt} \bar{h}^{(I)}$  obtained by explicitly time-finite-differencing the sequence of  $\bar{h}^{(I)}$  generated by the numerical evolution, rather than using the time derivatives computed by the Barack-Lousto-Sago evolution equations (3.7).

For computing diagnostics, the time finite-differencing uses off-centered (1-sided) 4th order molecules, using the current time slice and the 4 (5) immediately preceding time slices for  $\partial_t \bar{h}^{(I)}$  ( $\partial_{tt} \bar{h}^{(I)}$ ) respectively. My code suppresses computation of these time derivatives and the diagnostics  $Y^a$  and  $\tilde{G}_{ab}$  at any time where the time-finite-differencing would not have sufficient time levels of continuously-changing data. In practice, this means that diagnostics aren't computed for the initial data or the first 4 or 5 time steps of an evolution, nor are they computed for 4 or 5 time steps after  $\lambda^{(\text{occasionally updated})}$  is updated (since this causes  $\bar{h}^{(I)}$  to change discontinuously).<sup>20</sup>

### 4. No-Puncture-Subtraction Diagnostics

My formulas for  $\tilde{G}_{ab}$  don't take into account the presence of any source terms in the Einstein equations, and hence give wrong results within the worldtube if an effective-source scheme is used. To avoid this problem, my numerical code offers the option of computing "no-puncture-subtracted" ("nops") diagnostics, where the code effectively undoes the puncture subtraction of (3.9) inside the worldtube by defining

$$\bar{h}_{(\text{nops})}^{(I)} = \begin{cases} \bar{h}_{\text{num}}^{(I)} + \bar{h}_{(\text{puncture})}^{(I)} & \text{inside the worldtube} \\ \bar{h}_{\text{num}}^{(I)} & \text{outside the worldtube} \end{cases}, \quad (3.20)$$

<sup>20</sup> It would be possible to avoid this gap in the diagnostics after each  $\lambda^{(\text{occasionally updated})}$  update, by keeping a duplicate copy of the  $\bar{h}_{(\text{ortho})}^{(I)}$  computed using the pre-update  $\lambda^{(\text{occasionally updated})}$ . This would somewhat complicate the software, and possibly significantly increase memory usage, but would likely have only a minor CPU-time cost since only a small fraction of time steps would require the extra computation. I haven't implemented this technique.

and computing all diagnostics using the  $\bar{h}_{(\text{nops})}^{(I)}$ . (Since the spatial finite differencing still doesn't "know" about the particle, these diagnostics are still inaccurate within a finite difference molecule radius of the particle. These diagnostics also have some numerical cancellations near the particle due to the particle's Coulomb-type  $1/(r-r_p)$  singularity.)

## IV. NUMERICAL TESTS OF THE ORTHOGONALIZATION SCHEME

In this section I present numerical tests of the basic orthogonalization scheme for point-particle and effective-source particle models. (I present numerical tests of some variants of the orthogonalization scheme in appendix C.) Tables I and II give parameters for my test evolutions.

To study the convergence of the finite-difference numerical results to a continuum limit (discussed in detail in appendix D), I have run many evolutions at a number of different finite-difference resolutions between  $\Delta r_* = M/2$  and  $\Delta r_* = M/32$ . Unless noted otherwise, all results presented here are for  $\Delta r_* = M/8$ .

### A. Initial Data

All the evolutions presented here use the same (arbitrary) initial data, optionally modified as described in the next paragraph. For each  $I$ , this initial data sets each of  $\text{Re}[\bar{h}^{(I)}]$ ,  $\text{Im}[\bar{h}^{(I)}]$ ,  $\text{Re}[\partial_t \bar{h}^{(I)}]$ , and  $\text{Im}[\partial_t \bar{h}^{(I)}]$  to an independently-chosen Gaussian in  $r_*$ . Each Gaussian amplitude is randomly chosen from a uniform distribution on  $[-10, +10]$ , each Gaussian mean  $r_*$  is randomly chosen from a uniform distribution on  $[-10M, +10M]$ , and each Gaussian standard deviation in  $r_*$  is randomly chosen from a uniform distribution on  $[10M, 20M]$ .

For evolutions using an effective-source scheme (and not using the gradual turnon scheme discussed in appendix C3), it may be useful to explicitly subtract the puncture from the initial data within the worldtube, so that the (updated) initial data then satisfies the jump conditions (2.8). Table I explicitly states whether or not this subtraction is done for each test evolution.

### B. Orthogonalized Evolution (Point Particle)

I begin my presentation of numerical tests of the orthogonalization scheme with the simplest case: a point-particle model.

Figure 4 shows the time evolution of  $\lambda^{(\text{instantaneous})}$  and  $\lambda^{(\text{occasionally updated})}$  for the `ppart-ortho-50` evolution. After an initial transient,  $\lambda^{(\text{instantaneous})}$  shows gradually-decaying spiral oscillations in the complex plane, superimposed on a gradually-slowng drift. The oscillations have the same period as the particle orbit,  $P \approx 121.389M$ .  $\lambda^{(\text{occasionally updated})}$

Evolution name	particle?	puncture subtracted from initial data?	evolution duration $t_{\max}$	Courant factor $\Delta t/\Delta r_*$	nops?	orthogonalized?	$\lambda$ <sup>(occasionally updated)</sup>	notes
homogeneous	no	no	$1000M$	1.0	no	—	—	shown in figures 1–3
sourced-ppart	point particle	no	$1000M$	1.0	no	no	—	shown in figures 1–3
sourced-esrc	effective source	no	$1000M$	1.0	yes	no	—	shown in figures 1–3
ppart-ortho-50	point particle	no	$2000M$	1.0	no	yes	updated every $50M$ from $\lambda^{(\text{instantaneous})}$	shown in figures 4–7 and 22–24
esrc-ortho-P4	effective source	yes	$1011.573M$ $P/120 \approx 1.012$	yes	yes	yes	updated every $P/4 \approx 30.347M$ from $\lambda^{(\text{instantaneous})}$	shown in figures 8–11 and 22–24
esrc-ortho-P12	effective source	yes	$1011.573M$ $P/120 \approx 1.012$	yes	yes	yes	updated every $P/12 \approx 10.116M$ from $\lambda^{(\text{instantaneous})}$	shown in figures 13 and 14
ppart-ortho-oa-50	point particle	no	$2000M$	1.0	no	yes	updated every $50M$ from $\lambda^{(\text{orbit averaged})}$	shown in figures 15–17
esrc-gto-ortho-P4	effective source (gradual turnon)	no	$1011.573M$ $P/120 \approx 1.012$	yes	yes	yes	updated every $P/4 \approx 30.347M$ from $\lambda^{(\text{instantaneous})}$	shown in figures 18, and 19
ppart-ortho-fixed-from- oa-50-t=500	point particle	no	$2000M$	1.0	no	yes	fixed (never updated) $= \lambda^{(\text{orbit averaged})}$ at $t_{\max}^{(\text{base})} = 500M$ in <b>ppart-ortho-oa-50</b> evolution	shown in figure 20
ppart-ortho-fixed-from- oa-50-t=1000	point particle	no	$2000M$	1.0	no	yes	fixed (never updated) $= \lambda^{(\text{orbit averaged})}$ at $t_{\max}^{(\text{base})} = 1000M$ in <b>ppart-ortho-oa-50</b> evolution	shown in figure 20
ppart-ortho-fixed-from- oa-50-t=2000	point particle	no	$5000M$	1.0	no	yes	fixed (never updated) $= \lambda^{(\text{orbit averaged})}$ at $t_{\max}^{(\text{base})} = 2000M$ in <b>ppart-ortho-oa-50</b> evolution	shown in figures 20 and 21
ppart-ortho-cont	point particle	no	$1000M$	1.0	no	yes	updated every time step from $\lambda^{(\text{instantaneous})}$	discussed in footnote 10
esrc-ortho-cont	effective source	yes	$1011.573M$ $P/120 \approx 1.012$	yes	yes	yes	updated every time step from $\lambda^{(\text{instantaneous})}$	discussed in footnote 10

TABLE I. This table describes parameters specific to each test evolution. The column headed "nops?" specifies whether or not the diagnostics are computed using a no-puncture-subtracted copy of the  $\bar{h}^{(I)}$ , as described in section III D 4. See table II for parameters common to all the test evolutions.

Parameter name	value
spatial domain	$r_* \in [-100M - 1.5t_{\max}, +100M + 1.5t_{\max}]^\dagger$
$(\delta r_*)_{\text{widen}}$	$1M$
$(\delta r_*)_{\text{quantize}}$	$1M$
particle (if present)	located at $r = 7.2M$ ( $r_* \approx 9.111M$ ); orbital period $P \approx 121.389M$
worldtube (if present)	radius $\pm 2M$ in $r_*$ , centered on grid point closest to particle

TABLE II. This table describes parameters common to all the test evolutions. See table I for parameters specific to each test evolution.

<sup>†</sup> The factor of 1.5 is chosen to give a safety margin against possible numerical modes which may travel inwards from the spatial boundaries at superluminal speeds.

samples-and-holds  $\lambda^{(\text{instantaneous})}$  every  $\Delta t^{(\text{ortho})} = 50M$  (figure 4(b) and (c)). Since this sampling period doesn't integrally divide the orbital period  $P$ , the  $\lambda^{(\text{occasionally updated})}$  updates sample the oscillations at a different phase at each oscillation, so  $\lambda^{(\text{occasionally updated})}$  moves somewhat irregularly in the complex plane.

Figure 5 shows the time evolution of norms over grid points and tensor components of the resulting  $\bar{h}_{(\text{ortho})}^{(I)}$ ,  $Y^{(1,2,3)}$ , and  $\tilde{G}_{ab}$ . Notice that unlike the non-orthogonalized evolutions shown in figures 1 and 2, here  $\bar{h}^{(I)}$  (more precisely,  $\bar{h}_{(\text{ortho})}^{(I)}$ ) remains bounded at late times, showing no secular growth with time, while  $Y^{(1,2,3)}$  and  $\tilde{G}_{ab}$  still remain small.

Figure 6 shows snapshots and a movie of the resulting orthogonalized evolution at various times. Unlike figure 1, here the particle-orbit-period oscillations are clearly visible in the movie; the evolution is *not* dominated by the unstable mode. There are some low-level oscillations in the rescaled Einstein tensor  $\|\tilde{G}_{ab}\|$  for  $r_* \lesssim -25M$  and  $r_* \gtrsim 20M$ ; these are likely due to numerical cancellations in my computation of  $\tilde{G}_{ab}$  and don't grow with time. At late times  $\|Y^{(1,2,3)}\|$  and  $\|\tilde{G}_{ab}\|$  are small everywhere.

In section IID 1, I conjectured that at late times the unit-vector inner product  $\langle \widehat{h_{ab}^{(\text{ortho})}}, \widehat{h_{ab}^{(\text{unstable})}} \rangle$  should remain small. While I do not have direct access to  $h_{ab}^{(\text{unstable})}$ , I can use  $\bar{h}_{(\text{hom})}^{(I)}$  as a proxy for  $h_{ab}^{(\text{unstable})}$  at late times. Figure 7 shows the time evolution of the unit-vector inner product  $\langle \widehat{\bar{h}_{(\text{ortho})}^{(I)}}, \widehat{\bar{h}_{(\text{hom})}^{(I)}} \rangle$  for the ppart-ortho-50 evolution. Notice that, as conjectured in section IID 1 (and in contrast to the non-orthogonalized evolutions shown in figures 1 and 2, where the inner product is  $> 0.999$  at late times), at late times this inner product stays relatively small ( $\leq 0.4$ ) at late times, with no secular growth with time.

The success of the orthogonalization scheme in this evolution despite sampling the  $\lambda^{(\text{instantaneous})}$  oscillations at irregular phases suggests that the orthogonalization scheme should also work well for non-periodic particle orbits.

### C. Orthogonalized Evolution (Effective Source)

I now present a numerical test of the orthogonalization scheme using an effective-source model for the particle. Here I also make use of the particle orbit being periodic, and choose the orthogonalization time spacing  $\Delta t^{(\text{ortho})}$  to integrally divide the particle orbit period ( $\Delta t^{(\text{ortho})} = P/4$ ), so that  $\lambda^{(\text{occasionally updated})}$  is updated at the same set of orbital phases in each orbit.

Figure 8 shows the time evolution of  $\lambda^{(\text{instantaneous})}$  and  $\lambda^{(\text{occasionally updated})}$  for the esrc-ortho-P4 evolution.

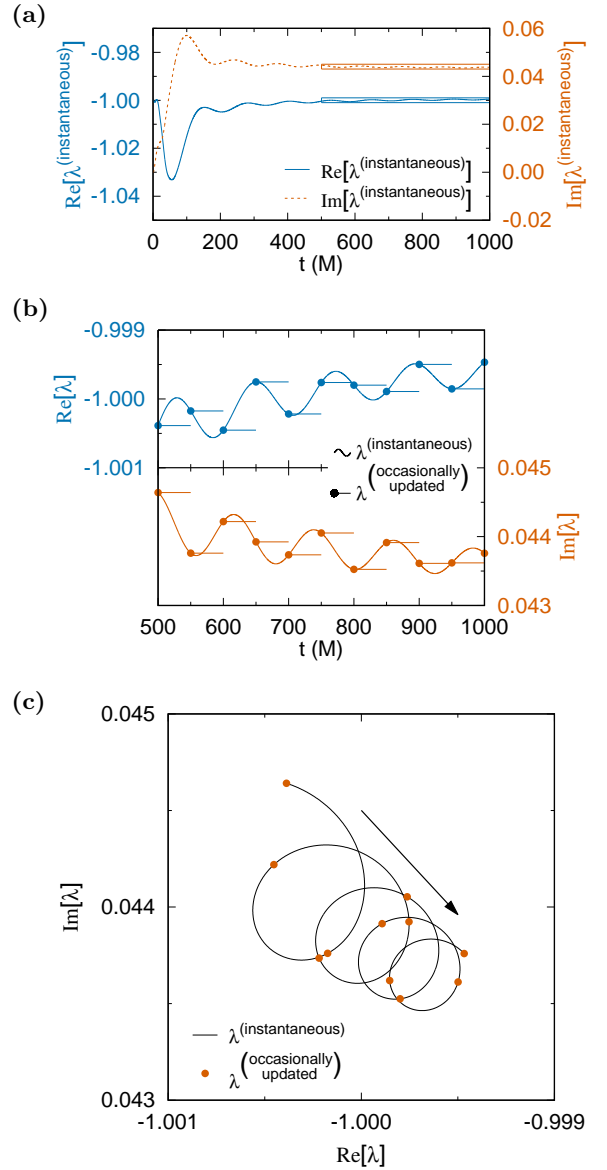


FIG. 4. This figure shows the time evolution of  $\lambda^{(\text{instantaneous})}$  and  $\lambda^{(\text{occasionally updated})}$  for the ppart-ortho-50 evolution. Part (a) shows the real and imaginary parts of  $\lambda^{(\text{instantaneous})}$  as functions of time. The rectangular regions are shown at an enlarged scale in parts (b) and (c). Part (b) shows, at an enlarged scale, the real and imaginary parts of both  $\lambda^{(\text{instantaneous})}$  and  $\lambda^{(\text{occasionally updated})}$  as functions of time for late times ( $t \geq 500M$ ). The solid dots and horizontal lines show the sample-and-hold behavior of  $\lambda^{(\text{occasionally updated})}$ . The legend applies to both real and imaginary parts. Part (c) shows, at an enlarged scale, the trajectories in the complex plane of both  $\lambda^{(\text{instantaneous})}$  (the spiral curve) and  $\lambda^{(\text{occasionally updated})}$  (the solid dots) for late times (again  $t \geq 500M$ ). The arrow shows the direction of the time evolution.

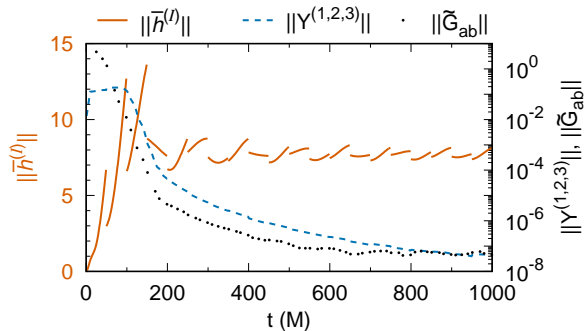


FIG. 5. This figure shows the time evolution of norms over grid points and components in the `ppart-ortho-50` evolution. The inner-product norm of  $\bar{h}_{(\text{ortho})}^{(I)}$  is plotted on the left scale, and the inner-product norm of the Lorenz gauge constraints  $Y^{(1,2,3)}$  and the RMS-norm of the rescaled Einstein tensor  $\tilde{G}_{ab}$  are plotted on the right (logarithmic) scale. Notice that unlike the non-orthogonalized evolutions shown in figure 2, here  $\|\bar{h}_{(\text{ortho})}^{(I)}\|$  remains bounded at late times, showing no secular growth with time.

$\lambda^{(\text{instantaneous})}$  shows similar oscillations to those observed in the point-particle case (figure 4). Because of the orbit-congruent sampling,  $\lambda^{(\text{occasionally updated})}$  displays more regular ( $\approx$  periodic) behavior than in the `ppart-ortho-50` evolution (figure 4).

Figure 9 shows the time evolution of the norms  $\|\bar{h}_{(\text{ortho})}^{(I)}\|$ ,  $\|Y^{(1,2,3)}\|$ , and  $\|\tilde{G}_{ab}\|$ . Notice that at late times, all the norms remain bounded, showing no secular growth with time.

Figure 10 shows snapshots and a movie of the resulting `escr-ortho-P4` orthogonalized evolution at various times. These are qualitatively very similar to the snapshots and movie of the point-particle `ppart-ortho-50` orthogonalized snapshots and movie shown in figure 6. In particular, the orthogonalized  $\bar{h}^{(I)}$  remain bounded throughout the evolution, and their Lorenz gauge constraints  $Y^{(1,2,3)}$  and rescaled Einstein tensor  $\tilde{G}_{ab}$  are small at late times. The particle-orbit-period oscillations are clearly visible in the movie; the evolution is *not* dominated by the unstable mode.

Figure 11 shows the time evolution of the unit-vector inner product  $\langle \bar{h}_{(\text{ortho})}^{(I)}, \bar{h}_{(\text{hom})}^{(I)} \rangle$  for the `escr-ortho-P4` evolution. This shows very similar behavior to that shown in figure 7 for the `ppart-ortho-50` evolution, with the inner product being relatively small at *all* late times.

## V. DISCUSSION AND CONCLUSIONS

In this paper I present and test a scheme for mostly eliminating the  $\ell = m = 1$  gauge instability in time-domain Lorenz-gauge evolutions of small metric perturbations of a background (typically Schwarzschild or Kerr)

spacetime.<sup>21</sup>

My scheme is based on *orthogonalizing* the metric perturbation with respect to an auxiliary homogeneous metric-perturbation evolved in parallel with the main (sourced) evolution. That is, given an (unstable) sourced metric perturbation  $h_{ab}$ , I define the orthogonalized metric perturbation  $h_{ab}^{(\text{ortho})} := h_{ab} + \lambda h_{ab}^{(\text{hom})}$ , where  $h_{ab}^{(\text{hom})}$  is the (unstable) auxiliary homogeneous metric perturbation and the scalar  $\lambda$  is chosen so that  $h_{ab}^{(\text{ortho})} \perp h_{ab}^{(\text{hom})}$  with respect to a specified inner product on metric perturbations.

If  $\lambda$  were updated continuously (i.e., at each time step of a numerical evolution), then  $\partial_t h_{ab}^{(\text{ortho})}$  and  $\partial_{tt} h_{ab}^{(\text{ortho})}$  would contain  $\partial_t \lambda$  and  $\partial_{tt} \lambda$  terms, causing  $h_{ab}^{(\text{ortho})}$  to violate the perturbed Einstein equations and the Lorenz gauge conditions. Therefore, my scheme instead uses a *piecewise-constant-in-time*  $\lambda$  which is only updated “occasionally” (typically every  $10M$  to  $50M$ <sup>22</sup>) during the evolution. At late times in the evolution (i.e., at times when  $h_{ab}^{(\text{hom})}$  is dominated by the unstable mode), the resulting  $h_{ab}^{(\text{ortho})}$  satisfies the perturbed Einstein equations and the Lorenz gauge conditions during each time interval where  $\lambda$  is constant.  $h_{ab}^{(\text{ortho})}$  has a jump discontinuity each time  $\lambda$  is updated; at late times in the evolution this jump should be purely a gauge transformation (within the family of Lorenz gauges).

I have tested the orthogonalization scheme for a Schwarzschild background spacetime, using both point-particle and “puncture” (effective-source) sources for the metric perturbation. My choice for the orthogonalization inner product is a spatial integral of the usual Euclidean inner product of the Barak-Lousto-Sago metric-perturbation variables.

I find that the orthogonalization scheme works well, in that the orthogonalized metric perturbation satisfies the perturbed Einstein equations and the Lorenz gauge conditions (up to finite-differencing accuracy), and contains only a small component of the unstable gauge mode; this “small component” can be made smaller by updating the orthogonalization more frequently.

To make this research more accessible, the full source code (about 60K lines of C++ and 2K lines of Sage) and parameter files used to generate all the data in this manuscript are included as online supplemental material. I am also submitting the code and parameter files to the Black Hole Perturbation Toolkit (BHP [1]).

<sup>21</sup> Here I consider only 1st-order metric perturbations, i.e., I am considering (only) evolution and gauge effects which are linear in the metric perturbations.

<sup>22</sup>  $M$  is the mass of the background Schwarzschild or Kerr spacetime.

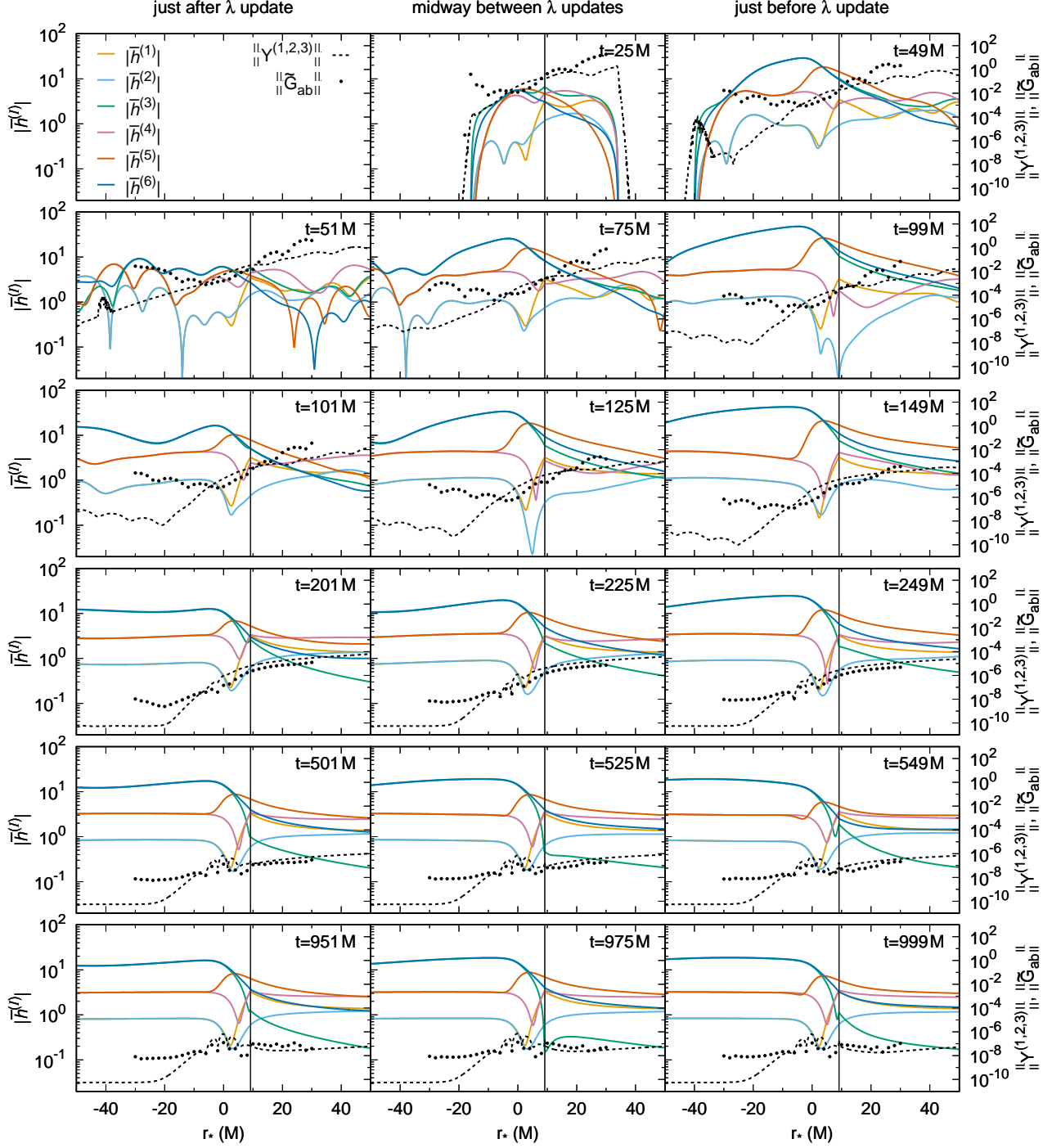


FIG. 6. This figure shows snapshots and a movie of the `ppart-ortho-50` orthogonalized evolution. The same legend (shown in the top left subplot) applies to all the subplots. Time runs across each row, then down. Within each row, the left subplot is at a time just after a  $\lambda^{(\text{occasionally updated})}$  update; the center subplot is midway between  $\lambda^{(\text{occasionally updated})}$  updates (which happen every  $50M$ ), and the right subplot is at a time just before the next  $\lambda^{(\text{occasionally updated})}$  update. In each subplot, the absolute values of the nontrivial Barack-Lousto-Sago metric-perturbation fields  $\bar{h}^{(1,2,3,4,5,6)}$  are plotted in color on the left scale (which is expanded relative to figure 1), and pointwise norms of the nontrivial Barack-Lousto-Sago Lorenz gauge constraints,  $\|Y^{(1,2,3)}\|$ , and of the independently-computed rescaled Einstein tensor,  $\|\tilde{G}_{ab}\|$  are plotted in black on the right scale (which is the same as figure 1);  $\|\tilde{G}_{ab}\|$  is only plotted at  $r_*$  intervals of  $2M$ . In the movie, notice that unlike the movie of figure 1, here the particle-orbit-period oscillations are clearly visible; the evolution is *not* dominated by the unstable mode.

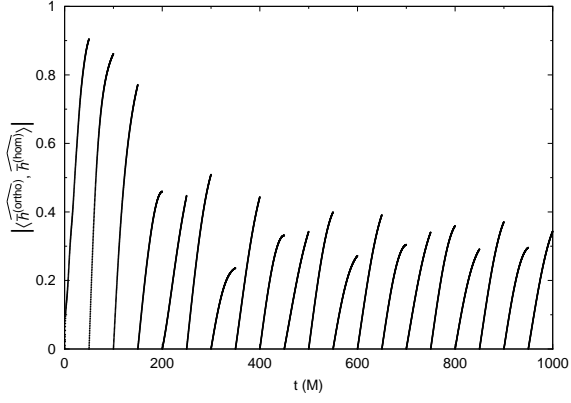


FIG. 7. This figure shows the time evolution of the unit-vector inner product  $\langle \bar{h}_{(\text{ortho})}^{(I)}, \bar{h}_{(\text{hom})}^{(I)} \rangle$  for the **ppart-ortho-50** evolution. This inner product grows due to the unstable mode, but resets to zero each time  $\lambda^{(\text{occasionally updated})}$  is updated. As conjectured in section IID 1, this inner product is relatively small at *all* late times.

### A. Possible Extensions to this Work

There are a number of directions in which this work could be extended.

As discussed in appendix D, my present numerical scheme shows fairly good convergence to a continuum limit for the orthogonalized metric perturbation (more precisely the orthogonalized Barack-Lousto-Sago metric-perturbation fields  $\bar{h}_{(\text{ortho})}^{(I)}$ ), but the convergence is poorer for the independently-computed Lorenz gauge constraints and rescaled Einstein tensor. Changes to the numerical scheme to improve this convergence would be very valuable.

My choices for inner product and orthogonalization update times seem reasonable, but many other choices are possible. For example, footnotes 18 and 19 suggest possible variants of the inner product. Alternatively, the ideas of Green et al. [24] might offer a route to constructing a geometrically-based inner product for metric perturbations of Kerr spacetime.

It would be useful to test the orthogonalization scheme with more general metric perturbations, notably those sourced by a small body moving on an eccentric orbit in Schwarzschild spacetime (my numerical tests here consider only circular orbits), and/or source-free evolutions.

If the extra  $\partial_t \lambda$  and  $\partial_{tt} \lambda$  terms in  $\partial_t h_{ab}^{(\text{ortho})}$  and  $\partial_{tt} h_{ab}^{(\text{ortho})}$  could somehow be cancelled or subtracted out, then the orthogonalization could be updated continuously, allowing an orthogonalized evolution completely free of the unstable mode (up to numerical accuracy).

My present numerical evolution scheme is relatively simple. I expect that the orthogonalization scheme would work equally well with more sophisticated numerical evolution schemes (e.g., adaptive mesh refinement, spectral,

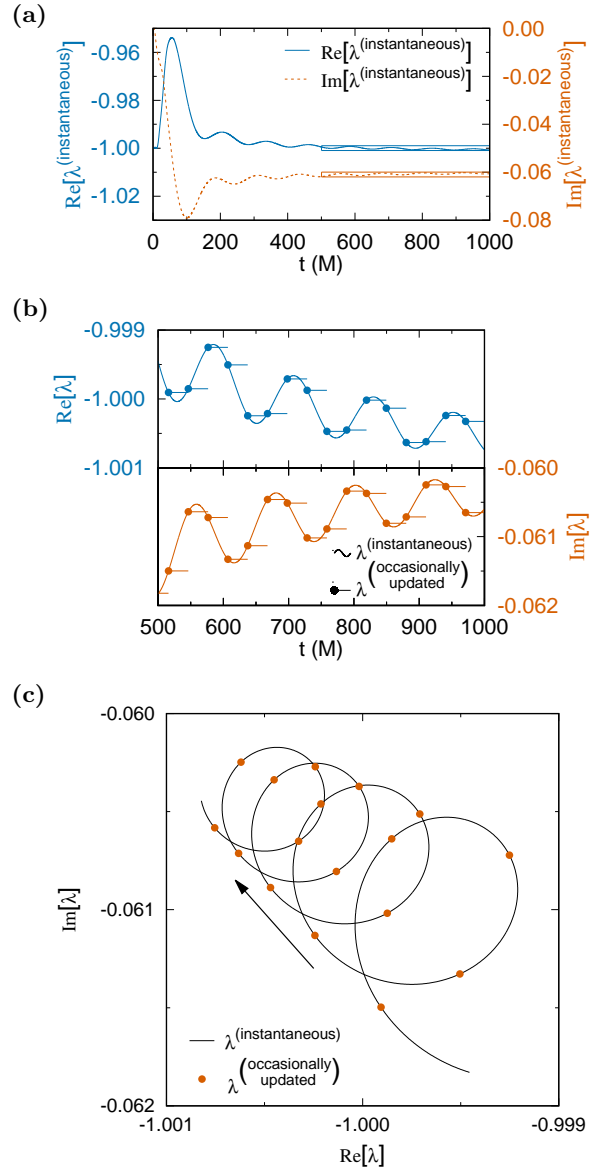


FIG. 8. This figure shows the time evolution of  $\lambda^{(\text{instantaneous})}$  and  $\lambda^{(\text{occasionally updated})}$  for the **escr-ortho-P4** evolution. Part (a) shows the real and imaginary parts of  $\lambda^{(\text{instantaneous})}$  as functions of time. The rectangular regions are shown at an enlarged scale in parts (b) and (c). Part (b) shows, at an enlarged scale, the real and imaginary parts of both  $\lambda^{(\text{instantaneous})}$  and  $\lambda^{(\text{occasionally updated})}$  as functions of time for late times ( $t \geq 500M$ ). The solid dots and horizontal lines show the sample-and-hold behavior of  $\lambda^{(\text{occasionally updated})}$ . The legend applies to both real and imaginary parts. Part (c) shows, at an enlarged scale, the trajectories in the complex plane of both  $\lambda^{(\text{instantaneous})}$  (the spiral curve) and  $\lambda^{(\text{occasionally updated})}$  (the solid dots) for late times ( $t \geq 500M$ ). The arrow shows the direction of the time evolution.

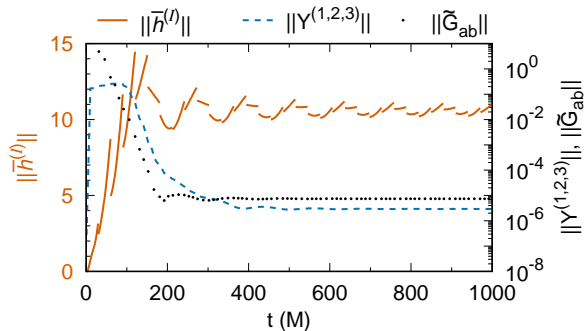


FIG. 9. This figure shows the time evolution of norms over grid points and components in the `esrc-ortho-P4` evolution. The inner-product norm of  $\bar{h}_{(\text{ortho})}^{(I)}$  is plotted on the left scale, and the inner-product norm of the Lorenz gauge constraints  $Y^{(1,2,3)}$  and the RMS-norm of the rescaled Einstein tensor  $\tilde{G}_{ab}$  are plotted on the right (logarithmic) scale. Notice that unlike the non-orthogonalized evolutions shown in figure 2, here all the norms remain bounded at late times, showing no secular growth with time.

and/or discontinuous Galerkin methods), and/or using hyperboloidal compactification at the horizon and  $\mathcal{J}^+$ , but it would be useful to explicitly verify this.

The numerical results presented here establish that  $h_{ab}^{(\text{ortho})}$  is in the Lorenz gauge at all late times, including both immediately before and immediately after re-orthogonalizations. In section IID 3 I argue that at late times, the change in  $h_{ab}^{(\text{ortho})}$  when re-orthogonalizing should be *only* a (Lorenz) gauge transformation, i.e., that  $h_{ab}^{(\text{ortho})}$  immediately after a late-time re-orthogonalization represents the *same* physical  $t = \text{constant}$  hypersurface as  $h_{ab}^{(\text{ortho})}$  immediately before (the same) re-orthogonalization. However, I have not explicitly verified this numerically. It would be valuable to do this, i.e., to explicitly construct the late-time re-orthogonalization gauge transformation and demonstrate that the change in  $h_{ab}^{(\text{ortho})}$  induced by a late-time re-orthogonalization is indeed purely a (Lorenz) gauge transformation.

The present work only calculates metric perturbations (or more precisely the Barack-Lousto-Sago variables  $\bar{h}^{(I)}$ ); it would be interesting to extend this to calculating the emitted gravitational waves, and then investigate whether or not late-time re-orthogonalizations significantly perturbs the gravitational waves and/or other gauge invariants.

And, of course, it would be very interesting to apply the orthogonalization scheme to metric perturbations on a Kerr background; this could provide a route to calculating (1st-order) radiation-reaction effects for highly-eccentric EMRIs.

## VI. ACKNOWLEDGEMENTS

It is a pleasure to thank some of the many people who have contributed to this research project.

I thank S. Dolan for many informative discussions, for hosting my research visits in 2014 and 2016, for deriving the “TXV” equations described in appendix A 1 for calculating jumps in the Barack-Lousto-Sago fields across a point particle, and for sharing unpublished research results on the Barack-Lousto-Sago evolution system.

I thank L. Barack for many informative discussions, and for his generosity in answering various questions about details of the BL05 evolution scheme. I thank M. Colleoni for valuable assistance with code comparisons to validate my implementation of the BL05 evolution system.

I thank B. Wardell for his LorenzGauge1DEffective-Source open-source effective source code (Wardell [38]), and for many informative discussions about effective-source schemes.

I thank W. Stein for initiating and leading the development of the open-source Sage symbolic computation system, and E.ourgoulhon for developing and making available the open-source SageManifolds software for tensor calculus and other computations.

I thank A. Buonanno and the Max-Planck-Institut für Gravitationsphysik for financial support and for hosting a research visit in 2018, and the Alexander von Humboldt Foundation and the Indiana University Center for Space-time Symmetries, Department of Astronomy, and Office of the Vice-Provost for Research for financial support.

### Appendix A: Point-Particle Jump Conditions

In this appendix I describe my scheme for calculating the jumps in  $\bar{h}^{(I)}$  across the particle.

#### 1. General Formalism

Slightly generalizing the BL05 evolution equations, consider a 1+1-dimensional linear wave equation with a  $\delta$ -function source,

$$-\partial_{tt}\mathbf{u} + \partial_{xx}\mathbf{u} + \mathbf{T}(x)\partial_t\mathbf{u} + \mathbf{X}(x)\partial_x\mathbf{u} + \mathbf{V}(x)\mathbf{u} = \mathbf{s}(t), \quad (\text{A1})$$

where for the remainder of this appendix only,  $x := r_*$ ,  $N > 0$  is an integer,  $\mathbf{s}(t)$  is an  $N$ -element column vector,  $\mathbf{T}(x)$ ,  $\mathbf{X}(x)$ , and  $\mathbf{V}(x)$  are  $N \times N$  coefficient matrices, and for any variable or expression  $q$ ,  $q' := \partial_x q$  and  $[q]_p$  is the jump in  $q$  across the particle.

Integrating (A1) from  $x_p - \epsilon$  to  $x_p + \epsilon$  and taking the limit  $\epsilon \rightarrow 0$  gives the jump in  $\partial_x \mathbf{u}$  as

$$[\mathbf{u}' ]_p = \lim_{\epsilon \rightarrow 0} \{ \mathbf{u}'(x_p + \epsilon) - \mathbf{u}'(x_p - \epsilon) \} = \mathbf{s}(t). \quad (\text{A2})$$

To find the jump in  $\partial_{xx} \mathbf{u}$ , take the difference of (A1) evaluated at  $x_p + \epsilon$  and  $x_p - \epsilon$ , then consider the limit of

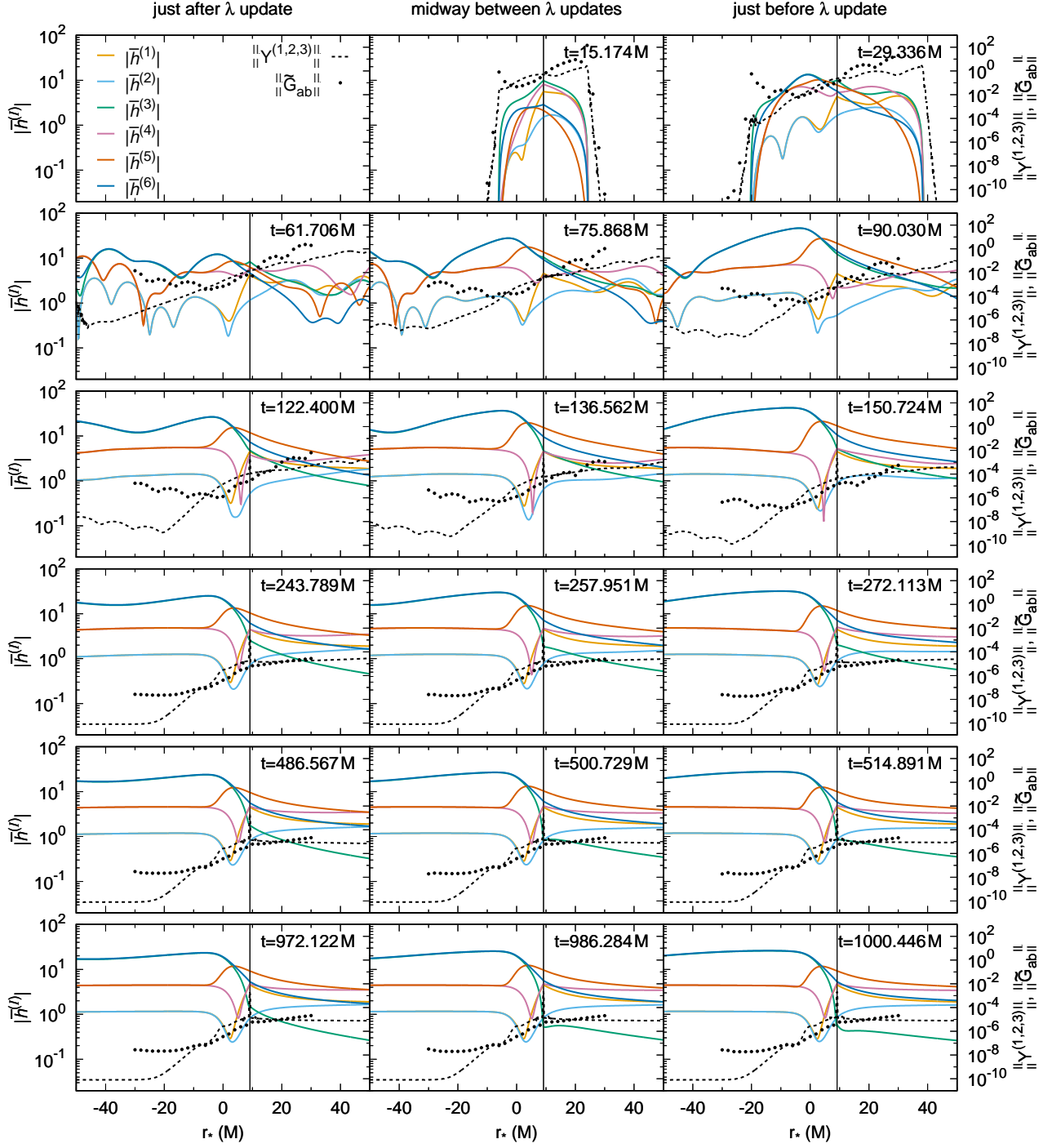


FIG. 10. This figure shows snapshots and a movie of the escr-ortho-P4 orthogonalized evolution. The same legend applies to all the subplots; note that the vertical scale is expanded relative to figure 1. Time runs across each row, then down. Within each row, the left subplot is at a time just after a  $\lambda$  <sup>(occasionally updated)</sup> update; the center subplot is midway between  $\lambda$  <sup>(occasionally updated)</sup> updates (which happen every  $\Delta t^{(\text{ortho})} \approx 30.347M$ ), and the right subplot is at a time just before the next  $\lambda$  <sup>(occasionally updated)</sup> update. Notice that, like figure 6 and unlike figure 1, here the  $\bar{h}^{(l)}$  all remain bounded throughout the evolution. In the movie, notice that like the movie of figure 6 and unlike the movie of figure 1, here the evolution is *not* dominated by the unstable mode.

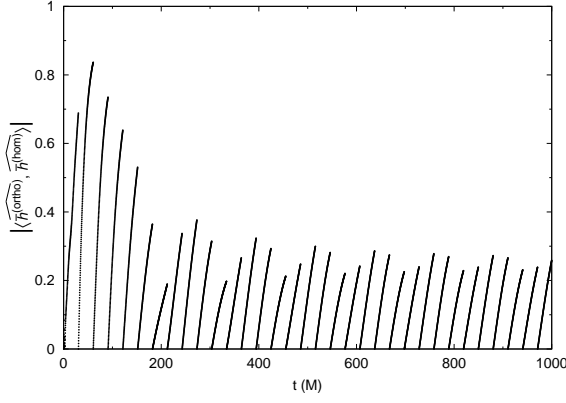


FIG. 11. This figure shows the time evolution of the unit-vector inner product  $\langle \bar{h}_{(\text{ortho})}^{(I)}, \bar{h}_{(\text{hom})}^{(I)} \rangle$  for the `esrc-ortho-P4` evolution. This inner product grows due to the unstable mode, but resets to zero each time  $\lambda$  (occasionally updated) is updated. As conjectured in section IID 1, this inner product is relatively small at *all* late times.

this difference as  $\epsilon \rightarrow 0$ . This gives

$$[\mathbf{u}'']_p = -\mathbf{X}(x_p)[\mathbf{u}']_p = -\mathbf{X}_p \mathbf{s}(t). \quad (\text{A3})$$

To find the jump in  $\partial_{xxx}\mathbf{u}$ , take an  $x$  derivative of (A1) and then repeat the above procedure. This yields

$$\begin{aligned} -\partial_{tt}[\mathbf{u}']_p + [\mathbf{u}''']_p \\ + \mathbf{X}'_p[\mathbf{u}']_p + \mathbf{X}_p[\mathbf{u}''']_p + \mathbf{T}_p \partial_t[\mathbf{u}']_p + \mathbf{V}_p[\mathbf{u}']_p \\ = 0, \end{aligned} \quad (\text{A4})$$

so that

$$[\mathbf{u}''']_p = \partial_{tt}\mathbf{s} - \mathbf{T}_p \partial_t \mathbf{s} - (\mathbf{X}'_p - \mathbf{X}_p^2 + \mathbf{V}_p)\mathbf{s}. \quad (\text{A5})$$

(If desired, jumps in higher-order derivatives can be found by iterating this procedure.)

## 2. Application to the $\bar{h}^{(I\ell m)}$ evolution equations

To apply the above formalism to the BL05 evolution equations (3.7), take  $N$  to be the number of nontrivial  $\bar{h}^{(I\ell m)}$  ( $N=6$  for the  $\ell=m=1$  case which is my focus here),  $\mathbf{u}$  to be an  $N$ -element column vector of those nontrivial  $\bar{h}^{(I\ell m)}$ , and take  $\mathbf{s}(t)$  to be an  $N$ -element column vector of the nontrivial components of the coefficient of  $\delta(r-r_0)$  in BL05's equation (29), multiplied by 4 (because the source term in (3.7) is  $4\mathcal{S}^{(I)}$ ).

The  $\mathbf{T}$ ,  $\mathbf{X}$ , and  $\mathbf{V}$  matrices together encode the right hand side of the  $\bar{h}^{(I\ell m)}$  evolution equation (3.7),

$$\mathbf{T}_{(IJ)} = \frac{\partial \text{RHS}_{(I)}^{(\text{vacuum})}(\mathbf{u}, \partial_{r_*}\mathbf{u}, \partial_{r_*r_*}\mathbf{u}, \partial_t\mathbf{u})}{\partial((\partial_t\mathbf{u})_{(J)})} \quad (\text{A6a})$$

$$\mathbf{X}_{(IJ)} = \frac{\partial \text{RHS}_{(I)}^{(\text{vacuum})}(\mathbf{u}, \partial_{r_*}\mathbf{u}, \partial_{r_*r_*}\mathbf{u}, \partial_t\mathbf{u})}{\partial((\partial_{r_*}\mathbf{u})_{(J)})} \quad (\text{A6b})$$

$$\mathbf{V}_{(IJ)} = \frac{\partial \text{RHS}_{(I)}^{(\text{vacuum})}(\mathbf{u}, \partial_{r_*}\mathbf{u}, \partial_{r_*r_*}\mathbf{u}, \partial_t\mathbf{u})}{\partial \mathbf{u}_{(J)}}, \quad (\text{A6c})$$

where  $\text{RHS}^{(\text{vacuum})}$  is regarded as a function of the independent variables  $\mathbf{u}$ ,  $\partial_{r_*}\mathbf{u}$ ,  $\partial_{r_*r_*}\mathbf{u}$ , and  $\partial_t\mathbf{u}$ .

From a software-engineering perspective, it's desirable to have  $\text{RHS}^{(\text{vacuum})}$ , and in particular the somewhat-complicated  $\mathcal{M}$  operator, defined in only a single place in the software (this is often called the “don't repeat yourself” rule, widely popularized by Hunt and Thomas [25]). To this end, my numerical code computes the  $\mathbf{T}$ ,  $\mathbf{X}$ , and  $\mathbf{V}$  matrices by directly finite differencing the  $\text{RHS}^{(\text{vacuum})}$  function. Because  $\text{RHS}^{(\text{vacuum})}$  is *linear* in  $\bar{h}^{(I\ell m)}$ ,  $\partial_{r_*}\bar{h}^{(I\ell m)}$ ,  $\partial_{r_*r_*}\bar{h}^{(I\ell m)}$ , and  $\partial_t\bar{h}^{(I\ell m)}$ , this finite differencing does *not* need to use a small step size for accuracy. Instead, the  $\mathbf{T}$ ,  $\mathbf{X}$ , and  $\mathbf{V}$  matrices can be computed exactly<sup>23</sup> (albeit slightly inefficiently) via

$$\mathbf{T}_{(IJ)} = \text{RHS}_{(I)}^{(\text{vacuum})}(\mathbf{0}, \mathbf{0}, \mathbf{0}, \boldsymbol{\delta}_{(J)}) - \text{RHS}_{(I)}^{(\text{vacuum})}(\mathbf{0}, \mathbf{0}, \mathbf{0}, \mathbf{0}) \quad (\text{A7a})$$

$$\mathbf{X}_{(IJ)} = \text{RHS}_{(I)}^{(\text{vacuum})}(\mathbf{0}, \boldsymbol{\delta}_{(J)}, \mathbf{0}, \mathbf{0}) - \text{RHS}_{(I)}^{(\text{vacuum})}(\mathbf{0}, \mathbf{0}, \mathbf{0}, \mathbf{0}) \quad (\text{A7b})$$

$$\mathbf{V}_{(IJ)} = \text{RHS}_{(I)}^{(\text{vacuum})}(\boldsymbol{\delta}_{(J)}, \mathbf{0}, \mathbf{0}, \mathbf{0}) - \text{RHS}_{(I)}^{(\text{vacuum})}(\mathbf{0}, \mathbf{0}, \mathbf{0}, \mathbf{0}), \quad (\text{A7c})$$

where  $\mathbf{0}$  is the  $N$ -element zero vector, and  $\boldsymbol{\delta}_{(J)}$  is the

$N$ -element Kronecker-delta vector

$$(\boldsymbol{\delta}_{(J)})_{(K)} = \begin{cases} 1 & \text{if } J = K \\ 0 & \text{if } J \neq K \end{cases}. \quad (\text{A8})$$

Since  $\mathbf{T}$ ,  $\mathbf{X}$ , and  $\mathbf{V}$  are only needed at one spatial position (the particle position), the actual computational cost of

<sup>23</sup> “Exactly” here means modulo floating-point rounding errors.

the  $3N+1$   $\text{RHS}^{(\text{vacuum})}$  evaluations needed to compute all components of  $\mathsf{T}_p$ ,  $\mathsf{X}_p$ , and  $\mathsf{V}_p$  via (A7) is minor compared to the overall cost of the evolution.

In my implementation the numerical grid is chosen such that the particle position does *not* coincide with any grid point. This implies that the source term vanishes at every grid point; the source appears only through the jumps across the particle.

This scheme does have one other slightly awkward requirement, namely that  $\text{RHS}^{(\text{vacuum})}$  must be evaluated at a non-grid point (the particle position). This means that  $\text{RHS}^{(\text{vacuum})}$  must be evaluated *without* using any coefficients precomputed or cached at the grid points. I found that this requires a certain amount of special programming, but isn't too difficult in practice.

Given  $\mathsf{T}_p$ ,  $\mathsf{X}_p$ ,  $\mathsf{V}_p$ , and  $\mathbf{s}(t)$ , the jumps in  $\partial_{r_*} \bar{h}^{(I\ell m)}$ ,  $\partial_{r_* r_*} \bar{h}^{(I\ell m)}$ , and  $\partial_{r_* r_* r_*} \bar{h}^{(I\ell m)}$  across the particle position are then given by (A2), (A3), and (A5) respectively.

## Appendix B: Numerical Methods

The focus of this work is on testing and exploring the behavior of the orthogonalization scheme, not on developing a highly efficient code. Therefore, I use a relatively simple finite-differencing numerical scheme.

### 1. Computing $r(r_*)$

Since I use a numerical grid uniform in  $r_*$ , computing various coefficients at the grid points requires knowing the  $r$  coordinates of the grid points. I compute these by numerically inverting the tortoise-coordinate definition (3.2). To do this, I define

$$y = \ln \left( \frac{r}{2M} - 1 \right) \quad (\text{B1})$$

$$x_* = \frac{r_*}{2M}, \quad (\text{B2})$$

so that  $r_* = r + 2My$  and  $r = 2M(1 + e^y)$ . (3.2) then becomes

$$x_* = 1 + y + e^y. \quad (\text{B3})$$

I numerically solve (B3) by Newton's method, finding a zero of the function

$$q(y) = 1 + y + e^y - x_*. \quad (\text{B4})$$

The initial guess is based on neglecting either  $y$  or  $e^y$  in (B4), giving

$$y^{(\text{initial})} = \begin{cases} \log(x_* - 1) & \text{if } x_* > 1 \ (y \gtrsim -0.577) \\ x_* - 1 & \text{if } x_* \leq 1 \ (y \lesssim -0.577) \end{cases} \quad (\text{B5})$$

The Newton's-method solution is moderately expensive (it typically requires 3–10 iterations at each grid point, with each iteration needing a couple of transcendental functions), so my code keeps a cache of the radii of all the grid points.

## 2. Notation for the remainder of this Appendix

Throughout the remainder of this appendix, I suppress the indices  $^{(I\ell m)}$ , and I use a lower-case Latin typewriter-font  $\mathbf{i}$  to index grid functions.

When describing finite-difference molecules (stencils), I use a lower-case Latin typewriter-font  $\mathbf{m}$  to index the molecule coefficients, so that a generic finite-difference operator  $\text{op}$  is defined by

$$(\text{op}(q))_{\mathbf{i}} = \sum_{\mathbf{m}=\mathbf{m}_{\min}}^{\mathbf{m}_{\max}} \text{op}_{\mathbf{m}} q_{\mathbf{i}+\mathbf{m}}, \quad (\text{B6})$$

where  $\Delta r_*$  is the grid spacing,  $q$  is the grid function being finite-differenced, and the molecule has nonzero coefficients (only) in the interval  $\mathbf{m} \in [\mathbf{m}_{\min}, \mathbf{m}_{\max}]$ . I refer to the molecule as having the evaluation point  $\mathbf{i}$  and (the set of) input points  $\{\mathbf{i}+\mathbf{m} \mid \mathbf{m} \in [\mathbf{m}_{\min}, \mathbf{m}_{\max}]\}$ .

I write molecule coefficients as a small matrix, with the coefficient at the evaluation point  $\mathbf{m} = 0$  underlined. For example, I write the usual centered 4th-order  $\partial_{r_*}$  finite difference molecule as

$$\mathbf{d} = \frac{1}{12\Delta r_*} \left[ +1 \quad -8 \quad \underline{0} \quad +8 \quad -1 \right], \quad (\text{B7})$$

where here  $m_{\min} = -2$  and  $m_{\max} = +2$ .

I refer to a finite-difference molecule as occupying the  $r_*$  interval defined by its input points, i.e.,

$$[(r_*)_{\mathbf{i}} + m_{\min} \Delta r_*, (r_*)_{\mathbf{i}} + m_{\max} \Delta r_*]. \quad (\text{B8})$$

I say that a finite-difference molecule (operator) ‘‘crosses the particle’’ if and only if the particle is contained in that interval, i.e., if and only if the sum (B6) includes both terms with  $(r_*)_{\mathbf{i}+\mathbf{m}} < (r_*)_p$  and terms with  $(r_*)_{\mathbf{i}+\mathbf{m}} > (r_*)_p$ . When using an effective-source scheme with a worldtube, I say that a finite-difference molecule (operator) ‘‘crosses the worldtube boundary’’ if and only if the sum (B6) includes both terms with  $\mathbf{i}+\mathbf{m}$  inside the worldtube and terms with  $\mathbf{i}+\mathbf{m}$  outside the worldtube.

## 3. Main finite differencing

For each  $(\ell, m)$ , I use a 4th-order Runge-Kutta method of lines scheme to time-integrate of the  $\bar{h}^{(I)}$  evolution equations (3.7), written in the 1st-order-in-time form

$$\partial_t(\bar{h}^{(I)}, \partial_t \bar{h}^{(I)}) = (\partial_t \bar{h}^{(I)}, \text{RHS}^{(\text{total})}(\bar{h}^{(I)}, \partial_t \bar{h}^{(I)})). \quad (\text{B9})$$

I use 4th order centered finite differencing on a uniform-in- $r_*$  grid to approximate the spatial derivatives in the  $\text{RHS}^{(\text{vacuum})}$  definition (3.7c) and the  $\mathcal{M}$  operator.

## 4. Dissipation

To reduce numerical noise, I add an additional dissipation term  $\epsilon \mathcal{D}(\bar{h})$  to the right hand side of (3.7c) at

selected grid points, where the dissipation operator  $D$  is the 6th-order Kreiss-Oliger dissipation operator (Rinne [28, appendix C]) with finite-difference molecule

$$D = \frac{1}{64 \Delta r_*} \begin{bmatrix} +1 & -6 & +15 & \underline{-20} & +15 & -6 & +1 \end{bmatrix}. \tag{B10}$$

All the results presented here use the dissipation coefficient  $\epsilon = 0.1$ .

I add the dissipation term only at those grid points with  $r_* \in [0, 15M]$  which also satisfy the following condition:

- For a point-particle scheme, the dissipation molecule must not cross the particle.
- For an effective-source scheme, the dissipation molecule must not intersect the worldtube.

### 5. Source Terms

Despite the major conceptual differences between the point-particle and effective-source particle models, their implementations at the level of finite differencing are actually mostly similar.

In both cases, for each finite-differencing operation at a grid point  $i$ , the code first tests

- for a point-particle model, whether or not the finite difference molecule would cross the particle; or,
- for an effective-source model, whether or not the finite difference molecule would cross the worldtube boundary.

In each case, this is (or can be) a very quick test, requiring only testing whether or not the grid-point index  $i$  is contained in a previously-computed interval or pair of intervals of grid-point indices.

If this test finds that the molecule would *not* cross the particle or worldtube boundary, then the code does the usual finite differencing operation on  $\bar{h}$  with no further attention needed to the source terms.<sup>24,25</sup>

If this test finds that the molecule *would* cross the particle or worldtube boundary, then the code instead finite-differences an “adjusted” temporary copy of a molecule-sized region of the  $\bar{h}$  grid function, where the “adjustment” corrects for the source model:

- for a point-particle model, the adjustment (described in detail in appendix B 5 a) corrects for the jumps in spatial derivatives of  $\bar{h}$  across the particle;
- for an effective-source model, the adjustment (described in detail in appendix B 5 b) corrects for the jump (2.8) in  $\bar{h}_{ab}^{\text{num}}$  across the worldtube boundary.

Because the “adjustment” is only done at a few grid points in each slice, the overall computational cost of this scheme is quite low.

#### a. Adjusted Finite Differencing: Point Particle

For a finite difference molecule which would cross the particle, the “adjustment” corrects for the jumps in spatial derivatives of  $\bar{h}$  across the particle by making each point of the temporary copy match the inside/outside-the-particle semantics of the evaluation point,

$$\bar{h}_{i+m}^{\text{adjusted}} = \begin{cases} \bar{h}_{i+m} & \text{if } (r_*)_i < (r_*)_p \text{ and } (r_*)_{i+m} < (r_*)_p \\ & \text{or if } (r_*)_i > (r_*)_p \text{ and } (r_*)_{i+m} > (r_*)_p \\ \bar{h}_{i+m} - J & \text{if } (r_*)_i < (r_*)_p \text{ and } (r_*)_{i+m} > (r_*)_p \\ \bar{h}_{i+m} + J & \text{if } (r_*)_i > (r_*)_p \text{ and } (r_*)_{i+m} < (r_*)_p \end{cases}, \tag{B11a}$$

where  $J$  is obtained by Taylor-expanding the jump in  $\bar{h}$  in the distance  $d$  from the particle,

$$J = J_{r_*} d + \frac{1}{2!} J_{r_* r_*} d^2 + \frac{1}{3!} J_{r_* r_* r_*} d^3 + \mathcal{O}(d^4), \tag{B11b}$$

where  $d = (r_*)_{i+m} - (r_*)_p$  and where  $J_{r_*}$ ,  $J_{r_* r_*}$ , and  $J_{r_* r_* r_*}$  are the jumps in  $\partial_{r_*} \bar{h}$ ,  $\partial_{r_* r_*} \bar{h}$ , and  $\partial_{r_* r_* r_*} \bar{h}$  respectively.

Because the evolution equation (3.7) contains  $\partial_{r_* r_*}$ , this scheme is only  $\mathcal{O}(\Delta r_*)^2$  accurate, but that’s sufficient for present purposes. If a higher order of accuracy were desired, I describe in section III B 1 how jumps in higher derivatives could be calculated, allowing the jump series (B11b) to be extended to higher orders of the distance  $d$ .

<sup>24</sup> For a point particle, I choose the grid so that the particle is not at a grid point. This implies that at every grid point, the  $\delta$ -function source term in BL05’s equation (29) vanishes.

<sup>25</sup> For the effective source used here,  $\bar{h}^{\text{num}}$  is only  $C^2$  at the particle position, so it would be more accurate – and would quite likely improve convergence (appendix D) – to special-case finite differencing operations which cross the particle, perhaps in the manner described in Thornburg and Wardell [34, appendix B.10]. I haven’t (yet) made this improvement.

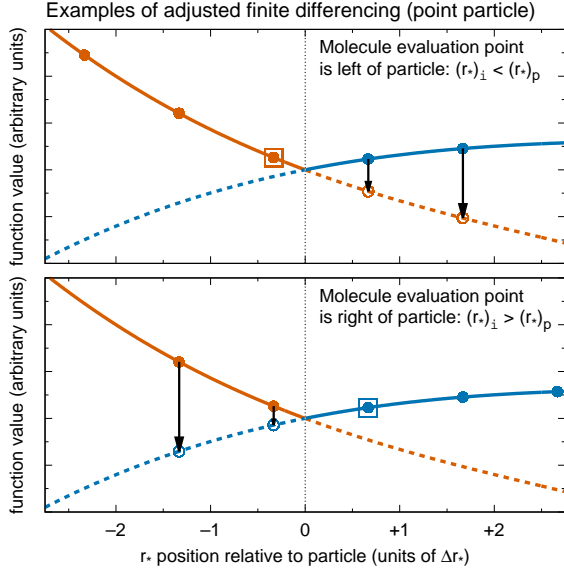


FIG. 12. This figure shows two examples of adjusted finite differencing using the scheme (B11) for the case of a point particle. In each panel, a sample  $\bar{h}^{(I\ell m)}$  is plotted as a solid line (red for  $r_* < (r_*)_p$  and blue for  $r_* > (r_*)_p$ ), with the grid-point values shown as filled circles. This sample  $\bar{h}^{(I\ell m)}$  has jump discontinuities in each of its spatial derivatives across the particle position (marked by a dashed vertical line). In each panel, the molecule-evaluation point is marked by a box around the filled circle.

The upper panel shows an example where the molecule evaluation point is to the left of the particle ( $(r_*)_i < (r_*)_p$ ). In this case, the adjustment (vertical arrows) is applied to the molecule input points to the right of the particle ( $(r_*)_{i+m} > (r_*)_p$ ), so that when combined with the molecule input points to the left of the particle (solid red circles) the adjusted  $\bar{h}^{(I\ell m)}$  values (open red circles) fall on a smooth curve (red curve, both solid and dashed) for finite differencing.

The lower panel shows an example where the molecule evaluation point is to the right of the particle ( $(r_*)_i > (r_*)_p$ ). In this case, the adjustment (vertical arrows) is applied to the molecule input points to the left of the particle ( $(r_*)_{i+m} < (r_*)_p$ ), so that when combined with the molecule input points to the right of the particle (solid blue circles), the adjusted  $\bar{h}^{(I\ell m)}$  values (open blue circles) again fall on a smooth curve (blue curve, both solid and dashed) for finite differencing.

## b. Adjusted Finite Differencing: Effective Source

For a finite difference molecule which would cross the particle, the “adjustment” corrects for the jump (2.8) in  $\bar{h}^{\text{num}}$  across the worldtube boundary,

$$\bar{h}_{i+m}^{\text{adjusted}} = \begin{cases} \bar{h}_{i+m}^{\text{num}} & \text{if } i \in W \text{ and } i+m \in W \\ & \text{or if } i \notin W \text{ and } i+m \notin W \\ \bar{h}_{i+m}^{\text{num}} + \bar{h}_{i+m}^{(\text{puncture})} & \text{if } i \in W \text{ and } i+m \notin W \\ \bar{h}_{i+m}^{\text{num}} - \bar{h}_{i+m}^{(\text{puncture})} & \text{if } i \notin W \text{ and } i+m \in W \end{cases}, \quad (\text{B12})$$

where  $W$  is the set of grid-point indices in the worldtube.

## 6. Boundary Conditions

Since the goal of the present work is solely to test the orthogonalization scheme, rather than to construct an

efficient production code, I choose the spatial domain to be sufficiently large that the spatial grid boundaries are causally disconnected with the inner-product region. (Table II gives the spatial grid boundary positions for each evolution.) This scheme is very inefficient (it evolves many grid points – in fact the vast majority of them – which are outside the inner-product region), but it avoids any concern about the boundary conditions possibly affecting my tests of the orthogonalization scheme.

Since the actual physical boundary condition doesn't affect the evolution within the inner-product region, I use an arbitrary boundary condition at the actual physical boundaries: before each evaluation of the right-hand-side function, each state-vector spatial ghost zone is zeroed.

### Appendix C: Tests of Variants of the Orthogonalization Scheme

In this appendix I present numerical tests of four variants of the basic orthogonalization scheme: using a shorter orthogonalization time spacing, orbit-averaging  $\lambda$ , gradual turnon of the puncture and effective source, and using a fixed (time-independent)  $\lambda$ .

#### 1. Shorter Orthogonalization Time Spacing

To show the effect of changing the orthogonalization time spacing  $\Delta t^{(\text{ortho})}$ , here I briefly present the *escr-ortho-P12* evolution, which is identical to the *escr-ortho-P4* evolution presented in section IV C except that the orthogonalization time spacing is a factor of 3 shorter:  $P/12 \approx 10.116M$  instead of  $P/4 \approx 30.347M$ .

Figure 13 shows the time evolution of the unit-vector inner product  $\langle \widehat{\bar{h}}_{(\text{ortho})}^{(I)}, \widehat{\bar{h}}_{(\text{hom})}^{(I)} \rangle$  for the *escr-ortho-P12* evolution. Because of the frequent orthogonalization updates, at late times the unit-vector inner product is very small ( $\lesssim 0.1$ ). That is, at late times the *escr-ortho-P12* evolution contains only a small component of the unstable mode.

Figure 14 shows the time evolution of the norms  $\|\widehat{\bar{h}}_{(\text{ortho})}^{(I)}\|$ ,  $\|Y^{(1,2,3)}\|$ , and  $\|\widetilde{G}_{ab}\|$ . Notice that at late times, all the norms remain bounded, showing no secular growth with time.

#### 2. Orbit Averaging

Figures 4 and 8 show that after an initial transient,  $\lambda^{(\text{instantaneous})}$  – and thus  $\lambda^{(\text{occasionally updated})}$  – tends to oscillate in a slowly-decaying spiral pattern in the complex plane, with oscillation period equal to the particle's orbital period  $P$ . Changing the definition of  $\lambda^{(\text{occasionally updated})}$  to be less oscillatory would be useful:

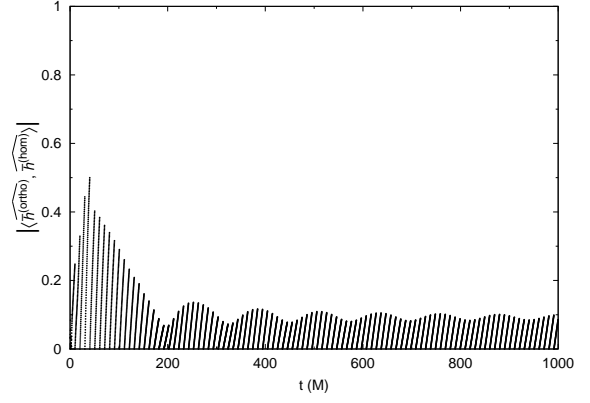


FIG. 13. This figure shows the time evolution of the unit-vector inner product  $\langle \widehat{\bar{h}}_{(\text{ortho})}^{(I)}, \widehat{\bar{h}}_{(\text{hom})}^{(I)} \rangle$  for the *escr-ortho-P12* evolution, where  $\lambda^{(\text{occasionally updated})}$  is updated every  $P/12 \approx 10.116M$ . The scale is the same as that of figure 9 (which shows the *escr-ortho-P4* evolution). In comparison to that evolution, here the unit-vector inner product is much smaller ( $\lesssim 0.1$ ) at late times.

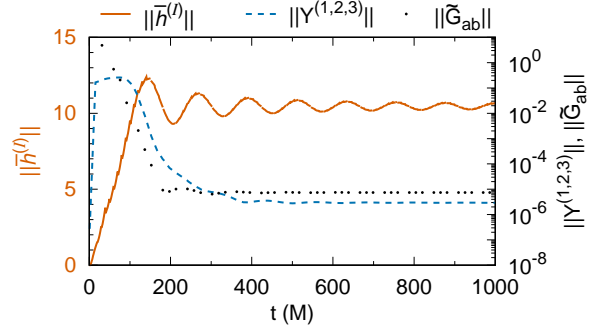


FIG. 14. This figure shows the time evolution of norms over grid points and components in the *escr-ortho-P12* evolution. The inner-product norm of  $\widehat{\bar{h}}_{(\text{ortho})}^{(I)}$  is plotted on the left scale, and the inner-product norm of the Lorenz gauge constraints  $Y^{(1,2,3)}$  and the RMS-norm of the rescaled Einstein tensor  $\widetilde{G}_{ab}$  are plotted on the right (logarithmic) scale. Both scales are the same as those of figure 9 (which shows the *escr-ortho-P4* evolution). All the norms remain bounded at late times, showing no secular growth with time.

- A less-oscillatory  $\lambda^{(\text{occasionally updated})}$  would reduce the magnitude of the jumps in  $h_{ab}^{(\text{ortho})}$  each time  $\lambda^{(\text{occasionally updated})}$  is updated.
- A less-oscillatory  $\lambda^{(\text{occasionally updated})}$  would make a finite-time  $\lambda^{(\text{occasionally updated})}$  a better estimate of the  $t \rightarrow \infty$  limit, which would improve the performance of the fixed- $\lambda$  orthogonalization variant discussed in section C 4.

This suggests averaging  $\lambda$  over an orbital period, i.e., defining

$$\lambda^{(\text{orbit averaged})}(t) = \text{average}(\lambda^{(\text{instantaneous})}, [t-P, t]), \quad (\text{C1a})$$

and then redefining  $\lambda^{(\text{occasionally updated})}$  as

$$\lambda^{(\text{occasionally updated})}(t) = \lambda^{(\text{orbit averaged})}([t]_{\{t_k\}}). \quad (\text{C1b})$$

(This scheme retains the definitions (2.14) and (3.13) of  $h_{ab}^{(\text{ortho})}$  and  $\bar{h}_{(\text{ortho})}^{(I)}$  in terms of  $\lambda^{(\text{occasionally updated})}$ .)

[In view of the orthogonality condition (2.11), an alternative possible definition for the orbit averaging would be to define  $\lambda^{(\text{orbit averaged})}(t)$  as that value of  $\lambda$  for which

$$\text{average}(\langle h_{ab}^{(\text{ortho})}, h_{ab}^{(\text{hom})} \rangle, [t-P, t]) = 0, \quad (\text{C2a})$$

or, if no such  $\lambda$  exists, that value of  $\lambda$  which minimizes

$$\left| \text{average}(\langle h_{ab}^{(\text{ortho})}, h_{ab}^{(\text{hom})} \rangle, [t-P, t]) \right|. \quad (\text{C2b})$$

I have not implemented this variant; indeed, it's not immediately obvious how to efficiently compute the (a)  $\lambda$  satisfying (C2).]

To test the orbit-averaging scheme (C1), I consider the **ppart-ortho-oa-50** evolution, which apart from the orbit averaging is identical to the non-orbit-averaged **ppart-ortho-50** evolution described in section IV B.

Figure 15 shows the time evolution of  $\lambda^{(\text{instantaneous})}$ ,  $\lambda^{(\text{orbit averaged})}$ , and  $\lambda^{(\text{occasionally updated})}$  for the **ppart-ortho-oa-50** evolution. Part (a), showing the time evolution of  $\lambda^{(\text{instantaneous})}$ , is identical to that of figure 4 (which shows the **ppart-ortho-50** evolution). Parts (b) and (c) show the effect of the orbit averaging.

Comparing figures 4 and 15, the changes in  $\lambda^{(\text{occasionally updated})}$  (and thus, the changes in the  $\bar{h}^{(I)}$ ) at each update are much smaller in the orbit-averaged **ppart-ortho-oa-50** evolution (figure 15) than in the non-orbit-averaged **ppart-ortho-50** evolution (figure 4), showing the success of the orbit-averaging scheme.

Figure 16 shows the time evolution of the norms  $\|\bar{h}_{(\text{ortho})}^{(I)}\|$ ,  $\|Y^{(1,2,3)}\|$ , and  $\|\tilde{G}_{ab}\|$ . Notice that at late times  $\|\bar{h}_{(\text{ortho})}^{(I)}\|$  remains bounded, showing no secular growth with time, while  $\|Y^{(1,2,3)}\|$  and  $\|\tilde{G}_{ab}\|$  remain small. Comparing with figure 5 (which shows the non-orbit-averaged **ppart-ortho-50** evolution), here the changes in  $\lambda^{(\text{occasionally updated})}$  with each update are much smaller.

The snapshots and movie of this evolution are visually quite similar to those shown in figure 6 for the (non-orbit-averaged) **ppart-ortho-50** evolution, and are omitted here in the interests of brevity.

Figure 17 shows the time evolution of the unit-vector inner product  $\langle \bar{h}_{(\text{ortho})}^{(I)}, \bar{h}_{(\text{hom})}^{(I)} \rangle$  for the orbit-averaged

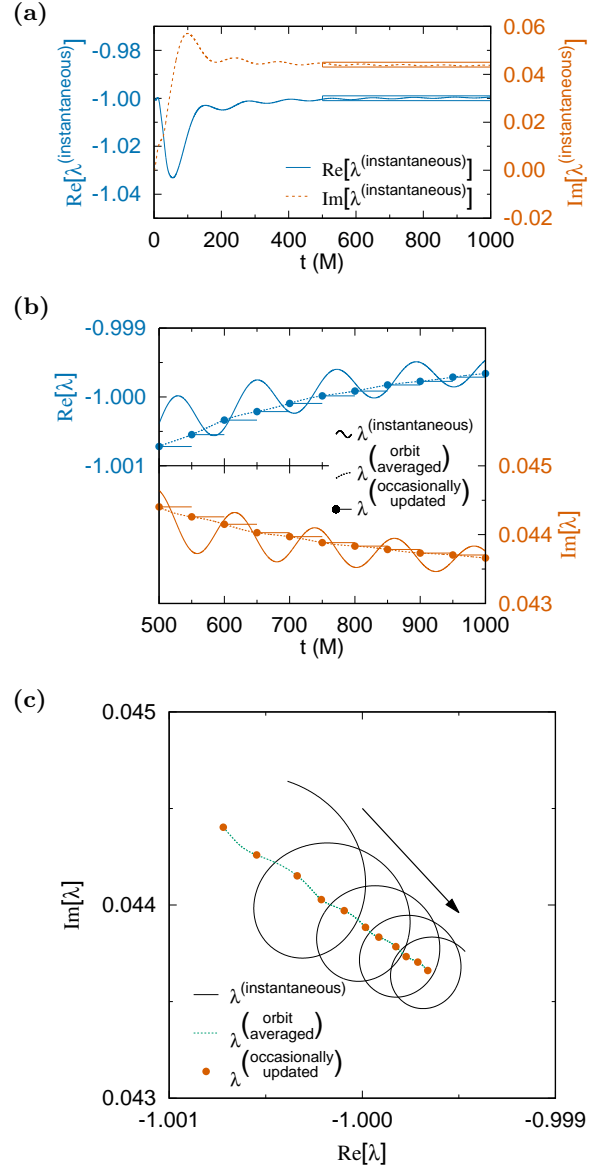


FIG. 15. This figure shows the time evolution of  $\lambda^{(\text{instantaneous})}$  and  $\lambda^{(\text{occasionally updated})}$  for the **ppart-ortho-oa-50** evolution. Part (a) (which is identical to that of figure 4) shows the real and imaginary parts of  $\lambda^{(\text{instantaneous})}$  as functions of time. The rectangular regions are shown at an enlarged scale in parts (b) and (c). Part (b) shows, at an enlarged scale, the real and imaginary parts of  $\lambda^{(\text{instantaneous})}$ ,  $\lambda^{(\text{orbit averaged})}$ , and  $\lambda^{(\text{occasionally updated})}$  as functions of time for late times ( $t \geq 500M$ ). The solid dots and horizontal lines show the sample-and-hold behavior of  $\lambda^{(\text{occasionally updated})}$ . The legend applies to both real and imaginary parts. Part (c) shows, at an enlarged scale, the trajectories in the complex plane of  $\lambda^{(\text{instantaneous})}$  (the spiral curve),  $\lambda^{(\text{orbit averaged})}$  (the wiggly dotted line), and  $\lambda^{(\text{occasionally updated})}$  (the solid dots) for late times ( $t \geq 500M$ ). The arrow shows the direction of the time evolution.

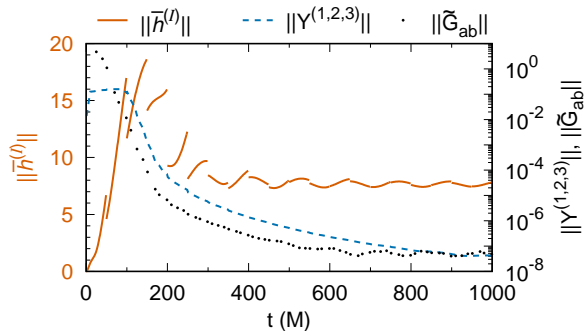


FIG. 16. This figure shows the time evolution of norms over grid points and components in the **ppart-ortho-50** evolution. The inner-product norm of  $\bar{h}_{(\text{ortho})}^{(I)}$  is plotted on the left scale, and the inner-product norm of the Lorenz gauge constraints  $Y^{(1,2,3)}$  and RMS-norm of the rescaled Einstein tensor  $\tilde{G}_{ab}$  are plotted on the right (logarithmic) scale. This figure should be compared with figure 5 (which shows the same norms for the non-orbit-averaged **ppart-ortho-50** evolution).

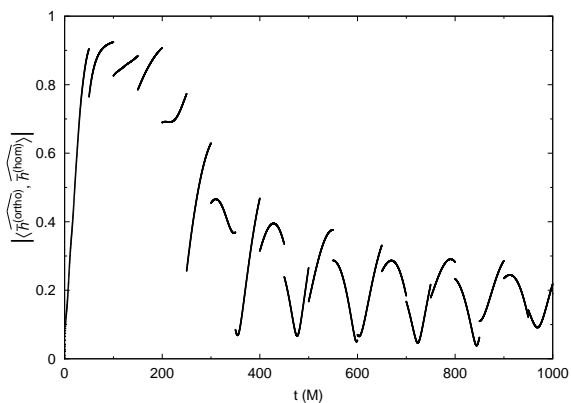


FIG. 17. This figure shows the time evolution of the unit-vector inner product  $\langle \widehat{h}_{(\text{ortho})}^{(I)}, \widehat{h}_{(\text{hom})}^{(I)} \rangle$  for the **ppart-ortho-50** evolution. Because of the orbit averaging, the unit-vector inner product doesn't reset to zero each time  $\lambda^{(\text{occasionally updated})}$  is updated. However, at late times this inner product still stays relatively small. This figure should be compared with figure 7 (which shows the same unit-vector inner product for the non-orbit-averaged **ppart-ortho-50** evolution).

**ppart-ortho-50** evolution. Comparing with figure 7 (which shows this same unit-vector inner product for the non-orbit-averaged **ppart-ortho-50** evolution), the qualitative behavior is somewhat different. Notably, the unit-vector inner product does *not* reset to zero each time  $\lambda^{(\text{occasionally updated})}$  is updated, and the jumps in the unit-vector inner product at each update are quite small. However, at late times the unit-vector inner product still stays relatively small, which is a key diagnostic of the

orthogonalization scheme's success.

### 3. Gradual Turnon of the Puncture and Effective Source

As noted in section III B 2, if the initial data doesn't already satisfy the jump conditions (3.9) across the worldtube boundary, the dynamical evolution generates high-spatial-frequency noise in the process of driving the fields into a configuration satisfying the jump conditions. This high-spatial-frequency noise tends to reduce the accuracy of the numerical computation.

One way to reduce this noise is to use a *gradual turnon* of the puncture and effective source: replace  $\bar{h}_{ab}^{(\text{puncture})}$  in (2.5) and  $\bar{h}_{(\text{puncture})}^{(I)}$  in (3.9b) by  $\text{gto}(t) \bar{h}_{ab}^{(\text{puncture})}$  and  $\text{gto}(t) \bar{h}_{(\text{puncture})}^{(I)}$  respectively, where the smooth “gradual-turnon function”  $\text{gto}$  is chosen to satisfy  $\text{gto}(0) \approx 0$  at  $t = 0$  and  $\text{gto}(t) \approx 1$  at late times.

When using gradual turnon, I use the same gradual-turnon function  $\text{gto}$  as Thornburg and Wardell [34, appendix B3], namely

$$\text{gto}(t) = \frac{1}{2} (1 + \text{erf}(z)) \quad (\text{C3a})$$

$$= \begin{cases} 1 - \frac{1}{2} \text{erfc}(z) & \text{if } z \geq 0 \\ \frac{1}{2} \text{erfc}(-z) & \text{if } z < 0 \end{cases} \quad (\text{C3b})$$

where the scaled time  $z := A + (t - t_{(\text{initial})})/B$ , and the alternative definition (C3b) avoids the numerical cancellation in (C3a) at early times.

When using gradual turnon, I use the parameters  $A = -5$  and  $B = 20M$ , so that  $\text{gto}(0) \approx 8 \times 10^{-13}$  (small enough that the initial high-frequency noise is negligible),  $\text{gto}(100M) = \frac{1}{2}$ , and  $|\text{gto}(t) - 1| < 10^{-6}$  for  $t \geq 168M$  (so that the effect of the gradual-turnon factor in the evolution equations is less than a part per million for all later times).

To test the gradual-turnon scheme, I consider the **escr-gto-ortho-P4** evolution, which apart from the gradual turnon is identical to the **escr-ortho-P4** evolution described in section IV C.

Figure 18 shows the time evolution of  $\lambda^{(\text{instantaneous})}$  and  $\lambda^{(\text{occasionally updated})}$  for the **escr-gto-ortho-P4** evolution. Compared to figure 8 (which shows the non-gradual-turnon **escr-ortho-P4** evolution), here  $\lambda^{(\text{instantaneous})}$  (and hence  $\lambda^{(\text{occasionally updated})}$ ) varies much more rapidly.

This more-rapid variation doesn't seem to harm the overall performance of the orthogonalization scheme. Figure 19 shows the time evolution of the norms  $\|\bar{h}_{(\text{ortho})}^{(I)}\|$ ,  $\|Y^{(1,2,3)}\|$ , and  $\|\tilde{G}_{ab}\|$ . Notice that at late times, all the norms remain bounded, showing no secular growth with time.

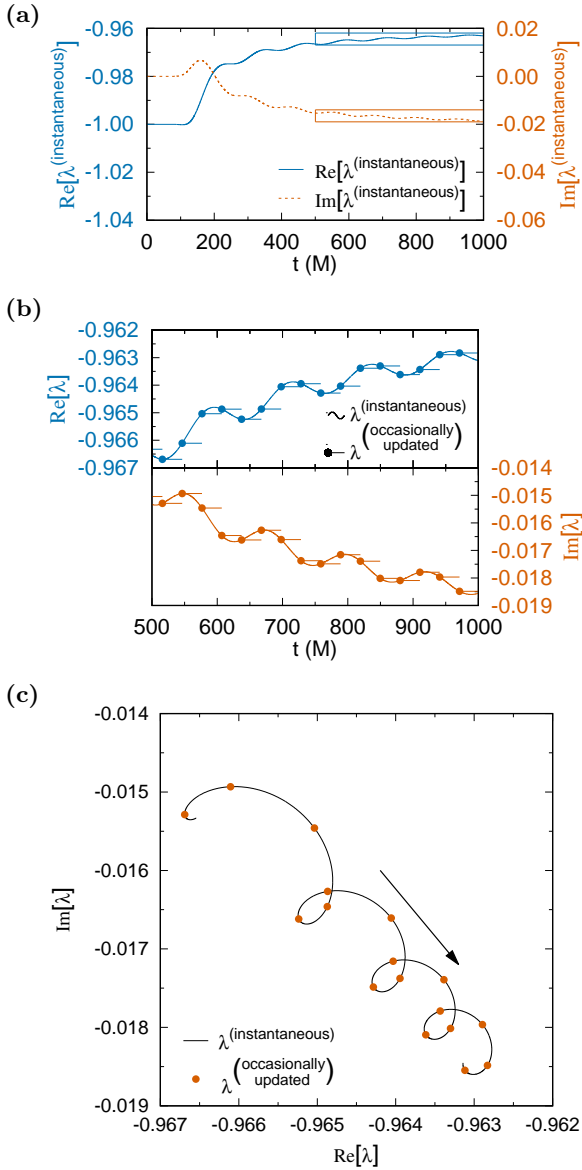


FIG. 18. This figure shows the time evolution of  $\lambda^{(\text{instantaneous})}$  and  $\lambda^{(\text{occasionally updated})}$  for the *esrc-gto-ortho-P4* evolution. Part (a) shows the real and imaginary parts of  $\lambda^{(\text{instantaneous})}$  as functions of time. The rectangular regions are shown at an enlarged scale in parts (b) and (c). Part (b) shows, at an enlarged scale, the real and imaginary parts of both  $\lambda^{(\text{instantaneous})}$  and  $\lambda^{(\text{occasionally updated})}$  as functions of time for late times ( $t \geq 500M$ ). The solid dots and dashed horizontal lines show the sample-and-hold behavior of  $\lambda^{(\text{occasionally updated})}$ . The legend applies to both real and imaginary parts. Part (c) shows, at an enlarged scale, the trajectories in the complex plane of both  $\lambda^{(\text{instantaneous})}$  (the spiral curve) and  $\lambda^{(\text{occasionally updated})}$  (the solid dots) for late times ( $t \geq 500M$ ). The arrow shows the direction of the time evolution.

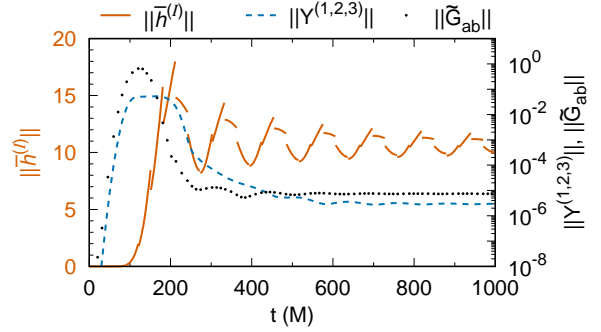


FIG. 19. This figure shows the time evolution of norms over grid points and components in the *esrc-gto-ortho-P4* evolution. The inner-product norm of  $\bar{h}_{(\text{ortho})}^{(I)}$  is plotted on the left scale, and the inner-product norm of the Lorenz gauge constraints  $Y^{(1,2,3)}$  and the RMS-norm of the rescaled Einstein tensor  $\tilde{G}_{ab}$  are plotted on the right (logarithmic) scale.

#### 4. Using a Fixed $\lambda$

Another way to reduce the jumps in  $\lambda^{(\text{occasionally updated})}$  is to never update  $\lambda^{(\text{occasionally updated})}$ , i.e., to choose  $\lambda^{(\text{occasionally updated})}$  to actually be some fixed (time-independent) constant  $\lambda^{(\text{fixed})}$ . In order for the unstable gauge mode to still be mostly cancelled,  $\lambda^{(\text{fixed})}$  should be fairly close to  $\lambda^{(\text{instantaneous})}$ .

This motivates the following scheme:

1. Compute a “base” orthogonalized evolution (possibly using orbit-averaging) for some time period  $t \in [0, t_{\text{max}}^{(\text{base})}]$ .
2. Choose  $\lambda^{(\text{fixed})}$  to be  $\lambda^{(\text{instantaneous})}(t_{\text{max}}^{(\text{base})})$ ,  $\lambda^{(\text{orbit averaged})}(t_{\text{max}}^{(\text{base})})$ , or some series acceleration (e.g., the Aitken, Richardson, or Shanks transformation) of the time sequence of  $\lambda^{(\text{instantaneous})}$  or  $\lambda^{(\text{orbit averaged})}$  in the base orthogonalized evolution.
3. Now compute a new “fixed- $\lambda$ ” approximately-orthogonalized evolution (starting from  $t = 0$ ) using  $\lambda^{(\text{occasionally updated})}(t) = \lambda^{(\text{fixed})}$ . The goal is that the fixed- $\lambda$  metric perturbation should contain only a relatively small component of the unstable mode throughout some “useful” range of times about  $t_{\text{max}}^{(\text{base})}$ . For a Schwarzschild background, we can assess this by determining the time interval over which the fixed- $\lambda$  unit-vector inner product  $\langle \bar{h}_{(\text{ortho})}^{(I)}, \bar{h}_{(\text{hom})}^{(I)} \rangle$  is relatively small.

Because  $\lambda^{(\text{instantaneous})}(t)$  and  $\lambda^{(\text{orbit averaged})}(t)$  vary only relatively weakly with  $t$  at late times (see, e.g., figures 4, 8, and especially 15),  $\lambda^{(\text{fixed})}$  will remain close to  $\lambda^{(\text{instantaneous})}(t)$  – and thus the fixed- $\lambda$  unit-vector inner

product  $\langle \widehat{\bar{h}}_{(\text{ortho})}^{(I)}, \widehat{\bar{h}}_{(\text{hom})}^{(I)} \rangle$  should remain relatively small – throughout a significant range of times about  $t = t_{\text{max}}^{(\text{base})}$ .

Moreover, since the variation of  $\lambda^{(\text{instantaneous})}(t)$  and  $\lambda^{(\text{orbit averaged})}(t)$  with  $t$  is slower at later times, increasing  $t_{\text{max}}^{(\text{base})}$  should widen (increase the duration of) the time interval about  $t = t_{\text{max}}^{(\text{base})}$  for which the fixed- $\lambda$   $\langle \widehat{\bar{h}}_{(\text{ortho})}^{(I)}, \widehat{\bar{h}}_{(\text{hom})}^{(I)} \rangle$  is relatively small.

For an initial test of the  $\lambda^{(\text{fixed})}$  scheme, I use the `ppart-ortho-oa-50` evolution as the base evolution, and set  $\lambda^{(\text{fixed})} := \lambda^{(\text{orbit averaged})}(t_{\text{max}}^{(\text{base})})$  with  $t_{\text{max}}^{(\text{base})} = 500M$ ,  $1000M$ , or  $2000M$  (the `ppart-ortho-fixed-from-oa-50-t=500`, `ppart-ortho-fixed-from-oa-50-t=1000`, and `ppart-ortho-fixed-from-oa-50-t=2000` evolutions, respectively).

Figure 20 shows the time evolution of  $\langle \widehat{\bar{h}}_{(\text{ortho})}^{(I)}, \widehat{\bar{h}}_{(\text{hom})}^{(I)} \rangle$  for these three  $\lambda^{(\text{fixed})}$  evolutions. As expected, in each case  $\langle \widehat{\bar{h}}_{(\text{ortho})}^{(I)}, \widehat{\bar{h}}_{(\text{hom})}^{(I)} \rangle$  is relatively small (operationalized here as  $\leq 0.4$ ) for a finite time interval about the time  $t_{\text{max}}^{(\text{base})}$ , and the duration of this time interval increases as  $t_{\text{max}}^{(\text{base})}$  increases. (The precise time intervals for each case are given in table III.) That is, by increasing  $t_{\text{max}}^{(\text{base})}$ , i.e., by setting  $\lambda^{(\text{fixed})}$  from the base-evolution  $\lambda^{(\text{occasionally updated})}$  at a later time, the duration of the time interval for which the fixed- $\lambda$  evolution is mostly free of the unstable mode can be increased.

Figure 21 shows the resulting fixed- $\lambda$   $\|\widehat{\bar{h}}_{(\text{ortho})}^{(I)}\|$ ,  $\|Y^{(1,2,3)}\|$ , and  $\|\widetilde{G}_{ab}\|$  for the case where  $\lambda^{(\text{fixed})}$  is set at  $t = 2000M$  (the `ppart-ortho-fixed-from-oa-at-t=2000` evolution).  $\|\widehat{\bar{h}}_{(\text{ortho})}^{(I)}\|$  shows little systematic increase with time during the time interval (shown shaded) where  $\langle \widehat{\bar{h}}_{(\text{ortho})}^{(I)}, \widehat{\bar{h}}_{(\text{hom})}^{(I)} \rangle \leq 0.4$ , suggesting that  $\widehat{\bar{h}}_{(\text{ortho})}^{(I)}$  is *not* dominated by the unstable mode.  $\|Y^{(1,2,3)}\|$  and  $\|\widetilde{G}_{ab}\|$  remain small at all late times.

In conclusion, using a fixed  $\lambda$  seems to provide an approximately-orthogonalized evolution which is mostly free of the unstable mode for a period of time which, while finite, can be considerably longer than  $1000M$ .

#### Appendix D: Convergence Tests

In any numerical solution of differential equations it's essential to ensure that as the numerical resolution is increased (i.e., as  $\Delta r_*$  is decreased), the numerical solution does indeed converge to to a continuum solution of the differential equations. A quantitative test of the rate of this convergence (and whether this rate matches the theoretical expectation) is an excellent test of the overall numerical computation (Choptuik [12]).

This convergence can be assessed by comparing numerical evolutions at varying numerical resolutions. Here I

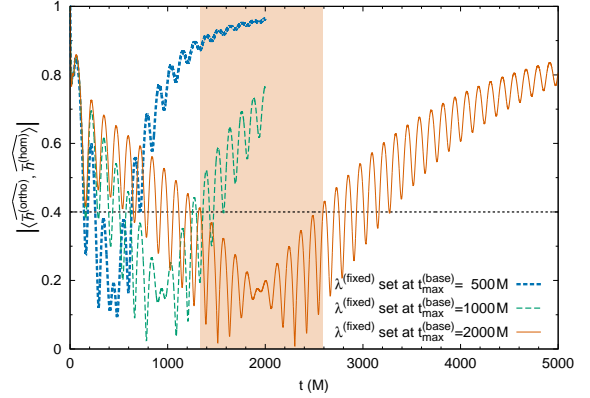


FIG. 20. This figure shows the time evolution of the unit-vector inner product  $\langle \widehat{\bar{h}}_{(\text{ortho})}^{(I)}, \widehat{\bar{h}}_{(\text{hom})}^{(I)} \rangle$  for fixed- $\lambda$  evolutions where  $\lambda^{(\text{fixed})}$  is set from the `ppart-ortho-oa-50` evolution's  $\lambda^{(\text{occasionally updated})}$  at  $t_{\text{max}}^{(\text{base})} = 500M$ ,  $1000M$ , and  $2000M$ . Notice that as the time ( $t_{\text{max}}^{(\text{base})}$ ) at which  $\lambda^{(\text{fixed})}$  is set increases, the time intervals for which  $\langle \widehat{\bar{h}}_{(\text{ortho})}^{(I)}, \widehat{\bar{h}}_{(\text{hom})}^{(I)} \rangle$  is “relatively small” ( $\leq 0.4$ , shown as the dashed horizontal line) becomes longer. This time interval is shown as the shaded region for the  $t_{\text{max}}^{(\text{base})} = 2000M$  case. The precise time intervals for each case are given in table III.

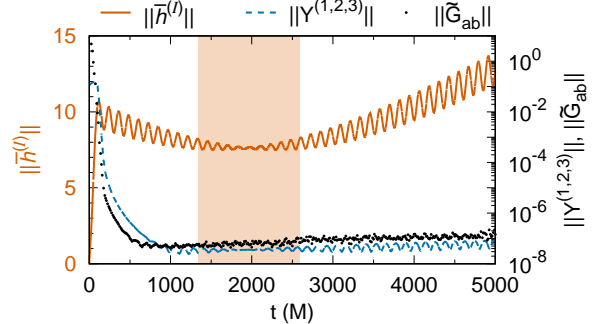


FIG. 21. This figure shows the time evolution of norms over grid points and components in the `ppart-ortho-fixed-from-oa-at-t=2000` evolution. The inner-product norm of  $\widehat{\bar{h}}_{(\text{ortho})}^{(I)}$  is plotted on the left scale, and the inner-product norm of the Lorenz gauge constraints  $Y^{(1,2,3)}$  and the RMS-norm of the rescaled Einstein tensor  $\widetilde{G}_{ab}$  are plotted on the right (logarithmic) scale. The time interval (of duration  $1253M$ ) for which  $\langle \widehat{\bar{h}}_{(\text{ortho})}^{(I)}, \widehat{\bar{h}}_{(\text{hom})}^{(I)} \rangle \leq 0.4$  is shaded.

use the resolutions

$$\Delta r_* \in \left\{ \frac{M}{2}, \frac{M}{3}, \frac{M}{4}, \frac{M}{6}, \frac{M}{8}, \frac{M}{12}, \frac{M}{16}, \frac{M}{24}, \frac{M}{32} \right\}. \quad (\text{D1})$$

I use the following convergence diagnostics:

- For each pair of resolutions differing by a factor

Fixed- $\lambda$ evolution	$t_{\max}^{(\text{base})}$	time interval	duration of time interval
ppart-ortho-fixed-from-oa-50-t=500	500M	$t \in [258, 630]M$	372M
ppart-ortho-fixed-from-oa-50-t=1000	1000M	$t \in [617, 1254]M$	637M
ppart-ortho-fixed-from-oa-50-t=2000	2000M	$t \in [1338, 2591]M$	1253M

TABLE III. For each fixed- $\lambda$  evolution, This table gives the  $t_{\max}^{(\text{base})}$  and the time intervals and durations for which  $\langle \widehat{\bar{h}}_{(\text{ortho})}^{(I)}, \widehat{\bar{h}}_{(\text{hom})}^{(I)} \rangle \leq 0.4$ . All the fixed- $\lambda$  evolutions use the ppart-ortho-50 evolution as the base evolution.

of 2, I compute the inner-product norm

$$\|(\bar{h}_{(\text{ortho})}^{(I)})_{(\text{lo})} - (\bar{h}_{(\text{ortho})}^{(I)})_{(\text{hi})}\|, \quad (\text{D2a})$$

where the subscripts  $_{(\text{lo})}$  and  $_{(\text{hi})}$  refer to the lower resolution and to the higher resolution (subsamped to the lower-resolution grid), respectively.

- For each resolution, I compute the inner-product norm

$$\|Y^{(1,2,3)}\| \quad (\text{D2b})$$

and the RMS-norm

$$\|\tilde{G}_{ab}\|, \quad (\text{D2c})$$

in both cases computed using the  $\bar{h}_{(\text{ortho})}^{(I)}$  and their independently-computed time derivatives as described in section III D 3.

Given my code’s 4th-order finite-differencing scheme (described in detail in appendix B), all these norms should ideally be proportional to  $(\Delta r_*)^4$ , at least for sufficiently high resolutions. As is standard in numerical relativity, I estimate the actual convergence order  $p$  by fitting the model

$$\log\|\cdot\| = p \log \Delta r_* + \text{constant} \quad (\text{D3})$$

to each of the norms (D2) across a range of  $\Delta r_*$ .

However, there is a complication: the numerical fields ( $\bar{h}^{(I)}$  for a point-particle scheme, or  $\bar{h}_{\text{num}}^{(I)}$  for an effective-source scheme) are non-smooth at the particle position:

- For a point-particle scheme,  $\bar{h}^{(I)}$  is generically  $C^0$  at the particle. Adjusted finite differencing across the particle (described in detail in appendix B 5 a) compensates for the non-smoothness, but because the jump series (B11b) is truncated at a finite order, the compensation isn’t perfect, i.e.,  $\bar{h}^{\text{adjusted}}$  as defined by (B11) isn’t  $C^\infty$  within a finite-difference molecule radius of the particle.
- For an effective-source scheme, because  $\bar{h}_{ab}^{(\text{puncture})}$  only matches a finite number of terms (in my case the first 4 terms) of the Laurent series expansion of  $\bar{h}_{ab}^{(\text{singular})}$  near the particle in powers of the distance from the particle,  $\bar{h}^{(\text{residual})}$  as defined by (2.4) is only finitely-differentiable at the particle ( $C^2$  for the puncture used here).

Applying finite difference operators to these non-smooth fields results in finite differencing errors which are “bump functions” (Thornburg [33, appendix F])<sup>26</sup> of the particle position modulo the grid spacing. Because each resolution in the convergence-test set (D1) samples such a bump function at a quasi-random phase,<sup>27</sup> each resolution’s theoretical  $\mathcal{O}((\Delta r_*)^4)$  finite-differencing error term is effectively multiplied by a quasi-random coefficient, somewhat spoiling smooth convergence.

I assess the convergence by considering the norms (D2) both as functions of time, and as functions of resolution at three sample late times, chosen to be immediately after the 2nd-to-last re-orthogonalization, midway between the 2nd-to-last and last re-orthogonalizations, and immediately before the last re-orthogonalization. These sample times are given in table IV. By comparing convergence orders across the sample times, I can determine whether the re-orthogonalizations impair convergence.

### 1. Convergence of $\bar{h}_{(\text{ortho})}^{(I)}$

Figure 22 shows the convergence of  $\|\bar{h}_{(\text{lo})}^{(I)} - \bar{h}_{(\text{hi})}^{(I)}\|$  for the ppart-ortho-50 and esrc-ortho-P4 evolutions. Parts (a) and (c) show  $\|\bar{h}_{(\text{lo})}^{(I)} - \bar{h}_{(\text{hi})}^{(I)}\|$  as a function of time for each evolution and each resolution pair. Parts (b) and (d) show  $\|\bar{h}_{(\text{lo})}^{(I)} - \bar{h}_{(\text{hi})}^{(I)}\|$  as a function of resolution at three sample times late in each evolution. The sample times are marked with vertical dashed lines in parts (a) and (c), and are listed in table IV.

For the esrc-ortho-P4 evolution, figure 22(c) shows that at late times  $\|\bar{h}_{(\text{lo})}^{(I)} - \bar{h}_{(\text{hi})}^{(I)}\|$  is relatively time-independent at the three highest resolutions ( $(\Delta r_*)_{(\text{lo})} \leq M/8$ ), but shows substantial secular growth with time at lower resolutions. Using a combination of  $\|\bar{h}_{(\text{lo})}^{(I)} - \bar{h}_{(\text{hi})}^{(I)}\|$  which are relatively time-independent and which are secularly growing with time would introduce a time-dependent bias

<sup>26</sup> Although the discussion of Thornburg [33, appendix F] is framed in terms of interpolation, it applies equally well to other finite differencing operations.

<sup>27</sup> This phase is effectively  $((r_*)_p \bmod \Delta r_*)/\Delta r_*$ . While not actually random, this phase is not controlled by my current numerical scheme.

Sample time	ppart-ortho-50 evolution	esrc-ortho-P4 evolution
Immediately after the 2nd-to-last late-time re-orthogonalization	$t = 1951M$	$t \approx 972.122M$
Midway between the 2nd-to-last and last late-time re-orthogonalizations	$t = 1975M$	$t \approx 986.284M$
Immediately before the last late-time re-orthogonalization	$t = 1999M$	$t \approx 1000.446M$

TABLE IV. This table gives the sample times for the convergence tests shown in figures 22, 23, and 24.

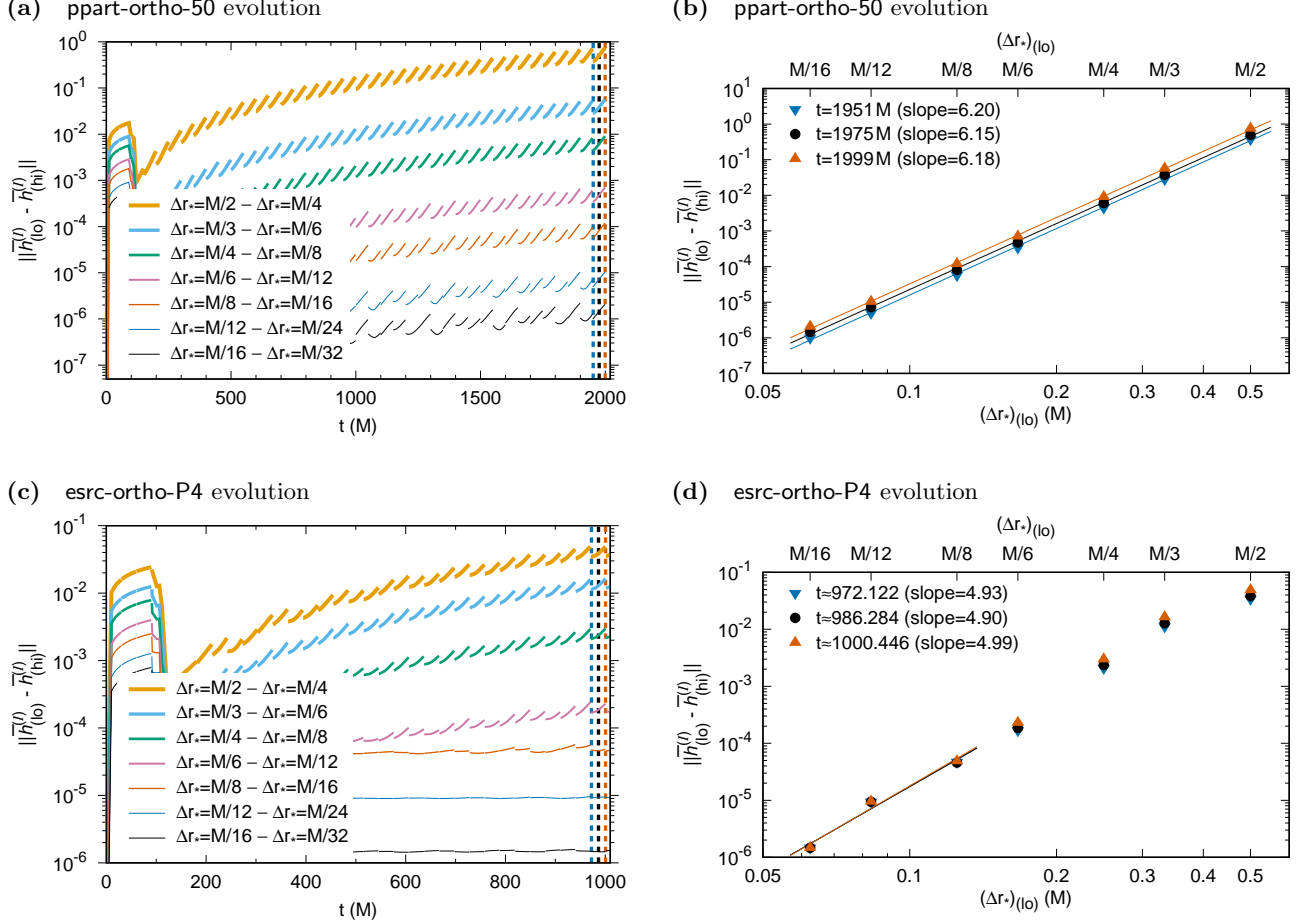


FIG. 22. This figure shows the convergence of  $\|\bar{h}_{(lo)}^{(I)} - \bar{h}_{(hi)}^{(I)}\|$  for the **ppart-ortho-50** and **esrc-ortho-P4** evolutions. The left column (parts (a) and (c)) shows the norms as a function of time. The right column (parts (b) and (d)) shows the norms as a function of the numerical resolution  $\Delta r_*$ , along with regression lines for fitting the convergence order, for the three sample times shown as vertical dashed lines in the left column (parts (a) and (c)). These sample times are given in table IV, and are chosen to be immediately after a late-time re-orthogonalization, midway between late-time re-orthogonalizations, and immediately before the next late-time re-orthogonalization, respectively. See the main text for further discussion.

into the convergence-order fit (figure 22(d)). To avoid this time-dependent bias, I use only the three highest resolutions ( $(\Delta r_*)_{(lo)} \leq M/8$ ) in the convergence-order fit (figure 22(d)).

For the **ppart-ortho-50** evolution  $\|\bar{h}_{(lo)}^{(I)} - \bar{h}_{(hi)}^{(I)}\|$  shows comparable secular growth at all resolutions (i.e., the different-resolution curves in figure 22(a) are roughly parallel to each other), so there's no reason to restrict the convergence-order fits to a subset of resolutions.

Actually, for both evolutions all the  $\|\bar{h}_{(lo)}^{(I)} - \bar{h}_{(hi)}^{(I)}\|$  points are quite close to the fitted convergence-order

lines in figures 22(b) and 22(d), so the choice of which resolutions are included in the fit makes relatively little difference in the fitted slopes (convergence orders).

For both evolutions, at each sample time the fitted convergence orders are significantly *greater* than the predicted 4. That is, at late times  $\|\bar{h}_{(lo)}^{(I)} - \bar{h}_{(hi)}^{(I)}\|$  is *not* dominated by  $\mathcal{O}((\Delta r_*)^4)$  finite-differencing errors. Also, since the norm in  $\|\bar{h}_{(lo)}^{(I)} - \bar{h}_{(hi)}^{(I)}\|$  is taken over a set of grid points which is bounded away from the particle (this is described in detail in section III C 1), the anomalously

high convergence orders can't be caused by the behavior of  $\bar{h}_{(\text{ortho})}^{(I)}$  near the particle.

The origin of these anomalously high convergence orders remains unclear; further research is needed to understand this.

## 2. Convergence of the Lorenz gauge constraints

Figure 23 shows the convergence of  $\|Y^{(1,2,3)}\|$  for the **ppart-ortho-50** and **escr-ortho-P4** evolutions. In each figure, parts (a) and (c) show  $\|\cdot\|$  as a function of time for each evolution and each resolution. Parts (b) and (d) show  $\|\cdot\|$  as a function of resolution at three sample times late in each evolution. The sample times are marked with vertical dashed lines in parts (a) and (c), and are listed in table IV.

For the **ppart-ortho-50** evolution, figure 23(a) shows that  $\|Y^{(1,2,3)}\|$  is still decreasing as a function of time at the end of the evolution ( $t_{\text{max}} = 2000M$ ) for the highest two resolutions ( $\Delta r_* \leq M/24$ ), and perhaps at the next lower resolution ( $\Delta r_* = M/16$ ) as well. This suggests that it might be useful to increase the duration  $t_{\text{max}}$  of this evolution.

Given the present data, I have chosen the range of resolutions  $M/12 \leq \Delta r_* \leq M/6$  as having  $\|Y^{(1,2,3)}\|$  being relatively time-independent for convergence-order fitting (figure 23(b)). At each sample time the fitted convergence orders are significantly *greater* than the predicted 4. However, at the three highest resolutions the convergence order is clearly much lower, and is in fact consistent with an error floor of  $\|Y^{(1,2,3)}\| \approx 10^{-9}$ .

For the **escr-ortho-P4** evolution, figure 23(c) shows that at late times,  $\|Y^{(1,2,3)}\|$  shows slow secular growth with time at the two lowest resolutions ( $\Delta r_* \geq M/3$ ). At late times, at intermediate resolutions ( $M/12 \leq \Delta r_* \leq M/4$ ),  $\|Y^{(1,2,3)}\|$  undergoes several particle-orbit-period oscillations before becoming approximately time-independent, while at the three highest resolutions ( $\Delta r_* \leq M/16$ ) these oscillations still have substantial amplitude at the end of the evolution ( $t_{\text{max}} \approx 1011.573M$ ), suggesting that it might also be useful to increase the duration  $t_{\text{max}}$  of this evolution.

Given the present data, I have chosen the range of resolutions  $\Delta r_* \leq M/4$  for convergence-order fitting (figure 23(d)). The fitted convergence orders are all much

less than the predicted 4, suggesting that  $\bar{h}_{(\text{ortho})}^{(I)}$  may not be fully smooth in this evolution (so that the spatial and time derivatives in  $Y^{(1,2,3)}$  result in a decrease of convergence order). Moreover, the  $\Delta r_* = M/16$  evolution shows a much smaller  $\|Y^{(1,2,3)}\|$  than would be the case for any fixed convergence order. This may be due to a fortuitous sampling of a bump-function finite-differencing error term very close to a zero.

## 3. Convergence of the rescaled Einstein tensor

Figure 24 shows the convergence of  $\|\tilde{G}_{ab}\|$  for the **ppart-ortho-50** and **escr-ortho-P4** evolutions. In each figure, parts (a) and (c) show  $\|\cdot\|$  as a function of time for each evolution and each resolution. Parts (b) and (d) show  $\|\cdot\|$  as a function of resolution at three sample times late in each evolution. The sample times are marked with vertical dashed lines in parts (a) and (c), and are listed in table IV.

For the **ppart-ortho-50** evolution, figure 24(a) shows that  $\|\tilde{G}_{ab}\|$  has a slow secular increase with time for almost all resolutions. Figure 24(b) shows that  $\|\tilde{G}_{ab}\|$  has two distinct ranges of variation with  $\Delta r_*$ : at lower resolutions ( $\Delta r_* \geq M/8$ )  $\|\tilde{G}_{ab}\|$  decreases with increasing resolution (decreasing  $\Delta r_*$ ) but at higher resolutions ( $\Delta r_* \leq M/12$ )  $\|\tilde{G}_{ab}\|$  increases with increasing resolution (decreasing  $\Delta r_*$ ).

For the **escr-ortho-P4** evolution, figures 24(c) and (d) show very similar behavior to the corresponding figures for  $\|Y^{(1,2,3)}\|$  (figures 23(c) and (d)). Notably, the  $\Delta r_* = M/16$  evolution shows a much smaller  $\|\tilde{G}_{ab}\|$  than would be the case for any fixed convergence order; this may again be due to a fortuitous sampling of a bump-function finite-differencing error term very close to a zero.

## 4. Convergence Summary

Figure 22 shows that in both the **ppart-ortho-50** and **escr-ortho-P4** evolutions,  $\|\bar{h}_{(\text{lo})}^{(I)} - \bar{h}_{(\text{hi})}^{(I)}\|$  converges smoothly (to zero) with increasing resolution (decreasing  $(\Delta r_*)_{(\text{lo})}$ ).

However, figures 23 and 24 show significant limitations and non-uniformities in the convergence of  $\|Y^{(1,2,3)}\|$  and  $\|\tilde{G}_{ab}\|$  (which are computed via numerical derivatives of the  $\bar{h}^{(I)}$ ), likely due to low-level non-smoothness in the numerical fields.

- 
- [1] Black Hole Perturbation Toolkit. (bhptoolkit.org), 2026.
  - [2] Miguel Alcubierre. *Introduction to 3 + 1 Numerical Relativity*. Oxford U.P., Oxford, U.K., 1986.
  - [3] Leor Barack, Marta Colleoni, Thibault Damour, Soichiro Isoyama, and Norichika Sago. Self-force effects on the marginally bound zoom-whirl orbit in Schwarzschild

- spacetime. *Phys. Rev. D*, 100:124015, Dec 2019.
- [4] Leor Barack and Darren A. Golbourn. Scalar-field perturbations from a particle orbiting a black hole using numerical evolution in 2+1 dimensions. *Phys. Rev. D*, 76(4):044020, Aug 2007.
- [5] Leor Barack and Carlos O. Lousto. Perturbations of

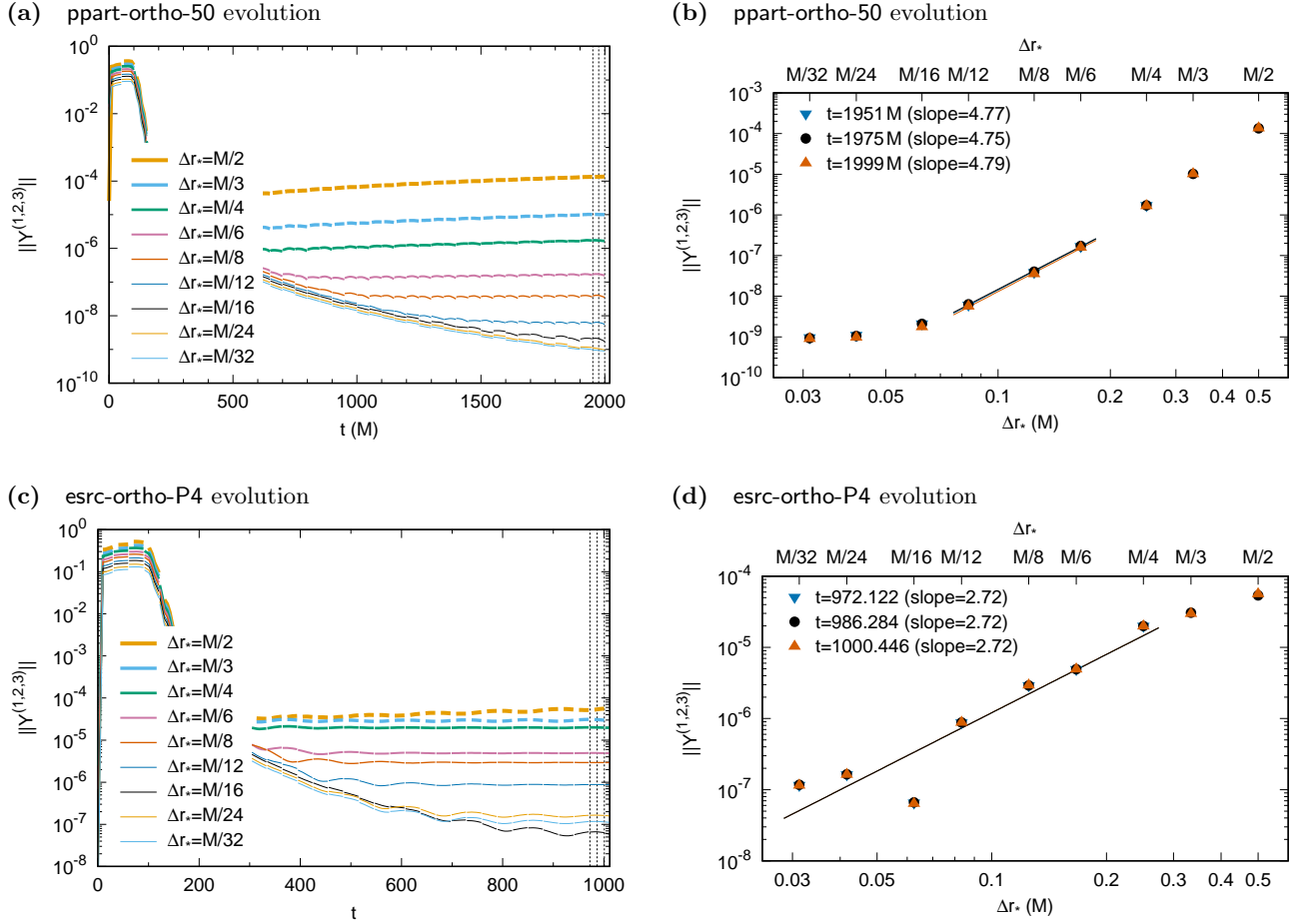


FIG. 23. This figure shows the convergence of  $Y^{(1,2,3)}$ , more precisely the inner-product norm  $\|Y^{(1,2,3)}\|$ , in the **ppart-ortho-50** and **esrc-ortho-P4** evolutions. The left column (parts (a) and (c)) shows the norms as a function of time. The right column (parts (b) and (d)) shows the norms as a function of the numerical resolution  $\Delta r_*$ , along with regression lines, for the three sample times shown as vertical dashed lines in the left column (parts (a) and (c)). These sample times are given in table IV, and are chosen to be immediately after a late-time re-orthogonalization, midway between late-time re-orthogonalizations, and immediately before the next late-time re-orthogonalization, respectively. See the main text for further discussion.

Schwarzschild black holes in the Lorenz gauge: Formulation and numerical implementation. *Phys. Rev. D*, 72(10):104026, 2005.

- [6] Leor Barack and Norichika Sago. Gravitational self-force on a particle in circular orbit around a Schwarzschild black hole. *Phys. Rev. D*, 75(6):064021, 2007.
- [7] Leor Barack and Norichika Sago. Gravitational self-force correction to the innermost stable circular orbit of a Schwarzschild black hole. *Phys. Rev. Lett.*, 102(19):191101, 2009.
- [8] Leor Barack and Norichika Sago. Gravitational self-force on a particle in eccentric orbit around a Schwarzschild black hole. *Phys. Rev. D*, 81(8):084021, Apr 2010.
- [9] Leor Barack and Norichika Sago. Beyond the geodesic approximation: conservative effects of the gravitational self-force in eccentric orbits around a Schwarzschild black hole. *Phys. Rev. D*, 83(8):084023, Apr 2011.
- [10] Luc Blanchet. Post-Newtonian theory for gravitational waves. *Living Reviews in Relativity*, 27(4), 2024.
- [11] Carles Bona and Carlos Palenzuela-Luque. *Elements of Numerical Relativity: From Einstein's Equations to Black Hole Simulations*. Number 673 in Lecture Notes in Physics. Springer-Verlag, 1st edition, 2005.
- [12] Matthew W. Choptuik. Consistency of finite-difference solutions to Einstein's equations. *Phys. Rev. D*, 44(10):3124–3135, 1991.
- [13] Steven Detweiler and Eric Poisson. Low multipole contributions to the gravitational self-force. *Phys. Rev. D*, 69:084019, Apr 2004.
- [14] Steven Detweiler and Bernard F. Whiting. Self-force via a Green's function decomposition. *Phys. Rev. D*, 67(2):024025, Jan 2003.
- [15] Sam R. Dolan and Leor Barack. Self force via  $m$ -mode regularization and 2+1 D evolution: III. Gravitational field on Schwarzschild spacetime. *Phys. Rev. D*, 87:084066, Apr 2013.
- [16] Sam R. Dolan, Leanne Durkan, Chris Kavanagh, and Barry Wardell. Metric perturbations of Kerr spacetime in Lorenz gauge: circular equatorial orbits. *Class. Quant. Grav.*, 41(15):155011, 2024.

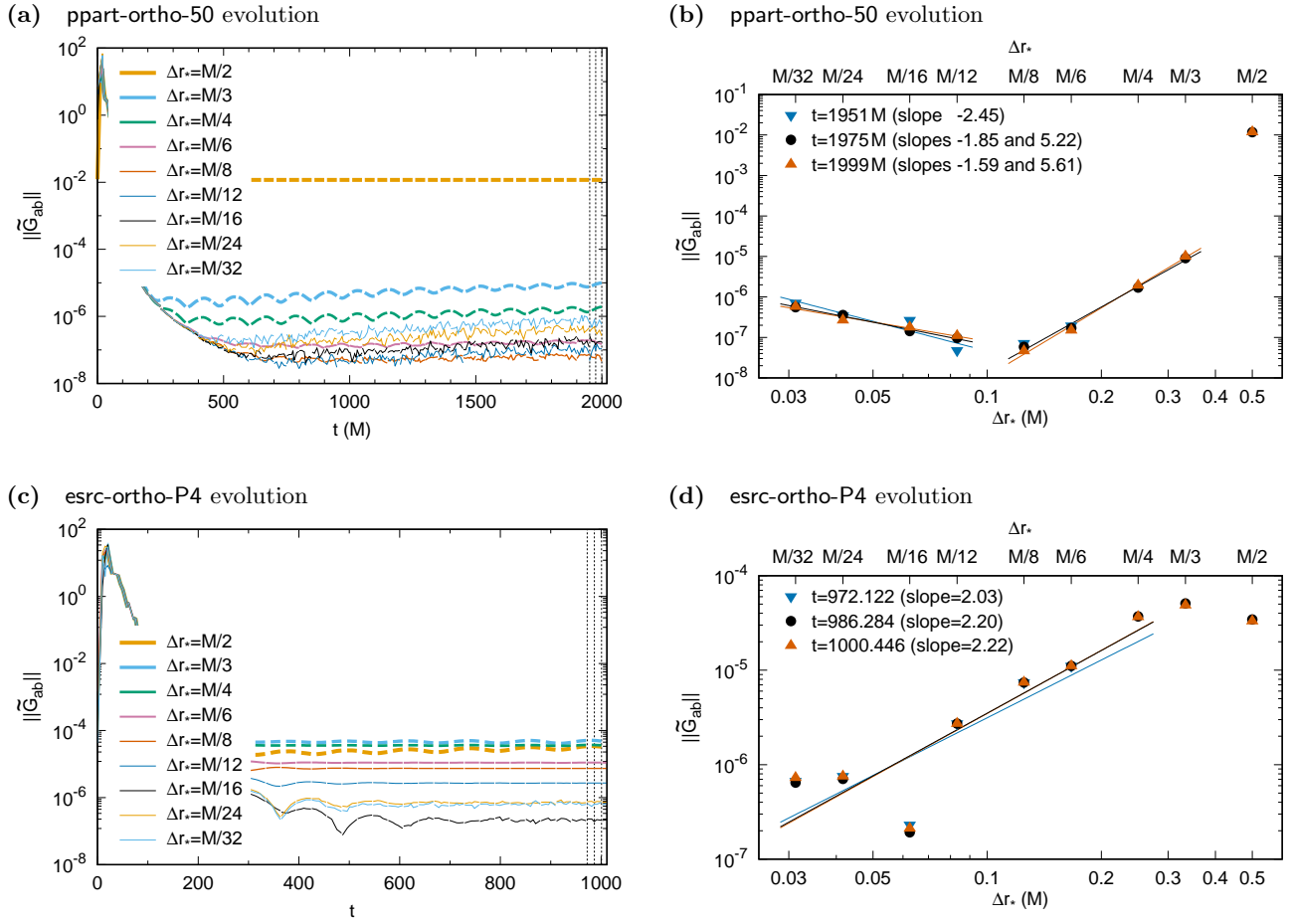


FIG. 24. This figure shows the convergence of  $\tilde{G}_{ab}$ , more precisely the RMS-norm  $\|\tilde{G}_{ab}\|$ , in the ppart-ortho-50 and esrc-ortho-P4 evolutions. The left column (parts (a) and (c)) shows the norms as a function of time. The right column (parts (b) and (d)) shows the norms as a function of the numerical resolution  $\Delta r_*$ , along with high-resolution and low-resolution regression lines for the indicated ranges of points, for the three sample times shown as vertical dashed lines in the left column (parts (a) and (c)). (The  $t = 1951$  low-resolution fit is omitted because the lowest 4 resolutions didn't have output at that time.) The sample times are given in table IV, and are chosen to be immediately after a late-time re-orthogonalization, midway between late-time re-orthogonalizations, and immediately before the next late-time re-orthogonalization, respectively. See the main text for further discussion.

- [17] Sam R. Dolan, Chris Kavanagh, and Barry Wardell. Gravitational Perturbations of Rotating Black Holes in Lorenz Gauge. *Phys. Rev. Lett.*, 128(15):151101, 2022.
- [18] Burçin Eröcal and William Stein. The Sage project: Unifying free mathematical software to create a viable alternative to Magma, Maple, Mathematica and Matlab. In Komei Fukuda, Joris van der Hoeven, Michael Joswig, and Nobuki Takayama, editors, *ICMS 2010: Proceedings of the Third International Congress on Mathematical Software*, volume 6327 of *Lecture Notes in Computer Science*, pages 12–27, Berlin, 2010. Springer-Verlag.
- [19] Toshifumi Futamase and Yousuke Itoh. The post-Newtonian approximation for relativistic compact binaries. *Living Reviews in Relativity*, 10(1):2, 2007.
- [20] David Goldberg. What every computer scientist should know about floating-point arithmetic. *ACM Computing Surveys*, 23(1):5–48, 1991.
- [21] Gene H. Golub and Charles F. Van Loan. *Matrix Computations*. Johns Hopkins University Press, Baltimore, MD, USA, 4th edition, 2013.
- [22] Éricourgoulhon, Michal Bejger, and Marco Mancini. Tensor calculus with open-source software: the SageManifolds project. *Journal of Physics: Conference Series*, 600:012002, Apr 2015.
- [23] Éricourgoulhon and Marco Mancini. *Symbolic tensor calculus on manifolds: a SageMath implementation*, pages 1–54. Number 1 in *Les cours du CIRM*. CIRM, 2018.
- [24] Stephen R. Green, Stefan Hollands, Laura Sberna, Vahid Toomani, and Peter Zimmerman. Conserved currents for a Kerr black hole and orthogonality of quasinormal modes. *Physical Review D*, 107(6):064030, Mar 2023.
- [25] Andrew Hunt and David Thomas. *The Pragmatic Programmer: From Journeyman to Master*. Addison-Wesley, Reading, MA, USA, 2nd edition, 2019.
- [26] Michael L. Katz, Alvin J. K. Chua, Lorenzo Speri,

- Niels Warburton, and Scott A. Hughes. Fast extreme-mass-ratio-inspiral waveforms: New tools for millihertz gravitational-wave data analysis. *Physical Review D*, 104(6), Sep 2021.
- [27] LISA Consortium Waveform Working Group. Waveform modelling for the Laser Interferometer Space Antenna. 2023. arXiv:2311.01300.
- [28] Oliver Rinne. An axisymmetric evolution code for the Einstein equations on hyperboloidal slices. *Class. Quant. Grav.*, 27(3), 15 January 2010.
- [29] Gerhard Schäfer and Piotr Jaranowski. Hamiltonian formulation of general relativity and post-Newtonian dynamics of compact binaries. *Living Reviews in Relativity*, 27(2), 2024.
- [30] William Stein and David Joyner. SAGE: System for Algebra and Geometry Experimentation. *ACM SIGSAM Bulletin*, 39(2):61–64, 2005.
- [31] Saul A. Teukolsky. The Kerr metric. *Class. Quant. Grav.*, 32(124006), 2014.
- [32] The Sage Developers. *SageMath, the Sage Mathematics Software System (Version 10.5.beta0)*, 2024. <https://www.sagemath.org>.
- [33] Jonathan Thornburg. A 3+1 computational scheme for dynamic spherically symmetric black hole spacetimes – I: Initial data. *Phys. Rev. D*, 59(10):104007, 1999.
- [34] Jonathan Thornburg and Barry Wardell. Scalar self-force for highly eccentric equatorial orbits in Kerr spacetime. *Phys. Rev. D*, 95:084043, Apr 2017.
- [35] Ian Vega and Steven Detweiler. Regularization of fields for self-force problems in curved spacetime: Foundations and a time-domain application. *Phys. Rev. D*, 77(8):084008, Apr 2008.
- [36] Robert M. Wald. *General relativity*. The University of Chicago Press, Chicago, 1984.
- [37] Barry Wardell. Self-force: Computational strategies. In Dirk Puetzfeld, Claus Lämmerzahl, and Bernard Schutz, editors, *Equations of Motion in Relativistic Gravity*, volume 179 of *Fundamental Theories of Physics*, pages 487–522. Springer International Publishing, 2015.
- [38] Barry Wardell. `LorenzGauge1DEffectiveSource`: Numerical code to compute a Lorenz-gauge 1-dimensional effective source, 2015.
- [39] Barry Wardell, Chris Kavanagh, and Sam R. Dolan. Sourced metric perturbations of Kerr spacetime in Lorenz gauge. *Class. Quant. Grav.*, 42(20):205007, 2025.
- [40] Bernard F Whiting and Larry R Price. Metric reconstruction from Weyl scalars. *Class. Quant. Grav.*, 22(15):S589–S604, 2005.